

Metallicity and Kinematics of M31's Outer Stellar Halo from a Keck¹ Spectroscopic Survey

David B. Reitzel²

Department of Physics & Astronomy, 8371 Mathematical Sciences Building, University of California at Los Angeles, Los Angeles, California 90095, USA

Email: reitzel@astro.ucla.edu

and

Puragra Guhathakurta

UCO/Lick Observatory, Department of Astronomy & Astrophysics, University of California, 1156 High Street, Santa Cruz, California 95064, USA

Email: raja@ucolick.org

ABSTRACT

We present first results from a spectroscopic survey designed to examine the metallicity and kinematics of individual red giant branch stars in the outer halo of the Andromeda spiral galaxy (M31). This study is based on multislit spectroscopy with the Keck II 10-m telescope and Low Resolution Imaging Spectrograph of the Ca II near-infrared triplet in 99 M31 halo candidates in a field at $R = 19$ kpc on the SE minor axis with brightnesses from $20 < I < 22$. The spectra are used to isolate M31 halo red giants from foreground Milky Way dwarf stars, faint compact background galaxies, and M31 disk giants. The observed distribution of radial velocities is well fit by an equal mix of foreground Milky Way dwarf stars, drawn from a standard Galactic model and with velocities $v \lesssim 0$ km s⁻¹, and M31 halo giants represented by a Gaussian of width $\sigma_v^{\text{M31}} \sim 150$ km s⁻¹ centered on its systemic velocity of $v_{\text{sys}}^{\text{M31}} \approx -300$ km s⁻¹. A secure sample of 29 M31 red giant stars is identified on the basis of radial velocity ($v < -220$ km s⁻¹), and, in the case of four intermediate-velocity stars ($-160 < v < -220$ km s⁻¹), broadband $B - I$ color. For this sample of objects, there is rough agreement between the metallicities derived in independent ways: two different calibrations of the Ca II absorption line strength and a photometric estimate based on fitting model stellar isochrones to an object's location in a $(B - I, I)$ color-magnitude

¹Data presented herein were obtained at the W. M. Keck Observatory, which is operated as a scientific partnership among the California Institute of Technology, the University of California and the National Aeronautics and Space Administration. The Observatory was made possible by the generous financial support of the W. M. Keck Foundation.

²This research was carried out as part of DBR's Ph.D. thesis in the Department of Astronomy & Astrophysics at the University of California at Santa Cruz.

diagram. The $[\text{Fe}/\text{H}]$ distribution of M31 halo giants has an rms spread of at least 0.6 dex and spans the $\gtrsim 2$ dex range over which the abundance measurement methods are calibrated. The mean/median metallicity of the M31 halo is about $\langle [\text{Fe}/\text{H}] \rangle = -1.9$ to -1.1 dex (depending on the details of metallicity calibration and sample selection) and possibly higher: the high-metallicity end of the distribution is poorly constrained by our data since the selection function for the secure M31 sample excludes $> 80\%$ of the giants in solar/super-solar metallicity range. Possible reasons are explored for the apparent discrepancy between the mean $[\text{Fe}/\text{H}]$ found in our spectroscopic survey (corrected for metallicity selection bias) and the slightly higher mean values found in earlier photometric studies. Field halo red giants in M31 appear to be somewhat more metal-rich on average than their Milky Way counterparts. The M31 halo $[\text{Fe}/\text{H}]$ distribution is comparable to that of M31 globular clusters, Galactic globular clusters, and Local Group dwarf satellite galaxies. The data in this 19 kpc outer halo field are broadly consistent with a scenario in which the halo is built from the accretion of small stellar subsystems. There are four stars in the secure M31 sample which have particularly strong Ca II lines indicating solar metallicity, at a common velocity of $\approx -340 \text{ km s}^{-1}$ close to the galaxy’s systemic velocity, similar to what might be expected for M31 disk giants on the minor axis. An extrapolation of the inner disk brightness profile, however, falls far short of accounting for these four stars—the disk would instead have to be very large ($R_{\text{disk}} \gtrsim 80 \text{ kpc}$) and/or warped. More likely, these four stars represent a metal-rich debris trail from a past accretion event in the halo.

Subject headings: galaxies: individual: Andromeda galaxy [Messier 31 (M31), NGC 224, UGC 454, CGCG 535-017] – galaxies: formation – stars: red giants – stars: metallicity

1. Introduction

Studying the metallicity gradient and spread in metallicity of galactic spheroids is important for understanding their formation and evolutionary history. The dissipational collapse model (Eggen, Lynden-Bell, & Sandage 1962; Larson 1974) predicts a strong radial metallicity gradient and a small spread of metallicities for fields at large distances from the center of the galaxy. The gradient is due to progressive chemical enrichment during the collapse of the protogalactic gas cloud while the small spread in metallicity is due to the paucity of metals present when the outer halo stars formed. The accretion model (Searle & Zinn 1978), on the other hand, predicts no strong gradient and a larger metallicity spread. In this picture, star formation largely precedes assembly of the galactic spheroid and the stellar subsystems which go into making the galaxy can have a variety of enrichment and star formation histories which are mixed together more or less randomly when the galaxy forms. Computer simulations and semi-analytic modeling of galaxy formation have reached new levels of sophistication in terms of dynamic range and inclusion of relevant physical processes such as star formation and feedback (cf. Johnston, Hernquist, & Bolte 1996; Johnston 1998; Helmi & White

1999; Helmi & de Zeeuw 2000; Bullock, Kravtsov, & Weinberg 2001). While the simulations are not yet detailed enough to make reliable predictions about the metallicity distribution within galaxies, they generally display a Searle-Zinn flavor of accretion during the formation of galactic spheroids.

The halo of the Galaxy has been studied in both its globular cluster system and field stars. Zinn (1993) finds evidence for two subpopulations of globular clusters. An “old halo” population of clusters displays a radial $[\text{Fe}/\text{H}]$ gradient, a small age spread, and significant rotation, while the (relatively) “young halo” population displays no radial $[\text{Fe}/\text{H}]$ gradient, a large age spread, and very little rotation. Zinn associates the former population with the initial collapse of the galaxy, and the latter with accretion of stellar systems throughout the lifetime of the Galaxy. The Milky Way halo field star population, however, does not show evidence for a radial metallicity gradient and has a lower mean metallicity than the clusters (Carney et al. 1990).

The Andromeda spiral galaxy (M31) is a good object to test these competing galaxy formation models as it provides an external perspective of a large spiral similar to our own and yet is close enough for individual stars to be studied in detail. Globular clusters and field red giant branch (RGB) stars are two visible tracers of M31’s halo. Huchra, Brodie, & Kent (1991) showed that there is evidence for a weak metallicity gradient in a sample of 150 M31 globular clusters, with a mean metallicity of $[\text{Fe}/\text{H}] = -1.2$ dex, which is slightly higher than the mean value of $[\text{Fe}/\text{H}] = -1.4$ dex for Galactic globular clusters (Zinn & West 1984). The M31 clusters also have a range of metallicities comparable to that of the Galactic globular clusters. While globular clusters are relatively prominent by virtue of their luminosity and unique appearance, M31 field halo stars are more elusive.

Over the last few decades, several groups have studied the metallicity distribution of field RGB stars in M31’s halo. Fields with projected distances from the center ranging from $7 \lesssim R \lesssim 34$ kpc have been targeted in ground-based imaging surveys.³ There is rough agreement in the mean metallicity measured in these studies, with values ranging from $-0.6 \leq [\text{Fe}/\text{H}] \leq -1.0$ dex. In particular, the recent $R = 20$ kpc minor axis wide-field study by Durrell, Harris, & Pritchett (2001) finds a median $[\text{Fe}/\text{H}]$ value (0.3 dex lower than their derived $[\text{m}/\text{H}]$ value) near the low-metallicity end of this range, but even this is slightly higher than the mean of the M31 globular cluster system. Another striking result is the discovery of an apparent streamer in the projected distribution of M31 halo red giants, whose metallicity appears to be similarly high judging from broadband colors of the constituent red giants (Ibata et al. 2001). The reader is referred to Reitzel, Guhathakurta, & Gould (1998, hereafter referred to as RGG) and references therein for a discussion of earlier ground-based studies.

RGG have studied a $15' \times 15'$ field in M31’s outer spheroid at $R = 19$ kpc on the SE minor axis.

³Throughout this paper, $D = 783$ kpc is adopted as the distance to M31 (Stanek & Garnavich 1998; Holland 1998).

In that study, deep *UBRI* images obtained using the Kitt Peak National Observatory⁴ (KPNO) 4-m telescope, and *I*-band images obtained with the Keck 10-m telescope and Low Resolution Imaging Spectrograph (LRIS, Oke et al. 1995), have been used to isolate a sample of M31 halo candidate RGB stars. The M31 RGB stars are distinguished from the more numerous distant field galaxies on the basis of broadband $U - B$, $B - R$, and $R - I$ colors and image morphology. The M31 halo field contains a clear excess of faint red objects ($I \sim 20 - 23$, $B - I \sim 2 - 3.5$) relative to a well-matched photometric control sample in a comparison field. The location of this population of faint red objects in the color-magnitude diagram (CMD) is as would be expected for red giant stars at the distance of M31. The overall color and distribution in the CMD of these excess objects suggests a relatively metal-rich population $\langle [\text{Fe}/\text{H}] \rangle \gtrsim -1$ dex, with a spread of ~ 2 dex.

A couple of studies of the M31 spheroid have used the *Hubble Space Telescope* (*HST*) Wide Field/Planetary Camera 2 (WFPC2) images to distinguish between stars and distant field galaxies. Rich et al. (1996a,b, 2002) have analyzed archival images of a field around the M31 globular cluster G1 ($R = 34$ kpc, major axis) along with fields surrounding a few other clusters distributed across the galaxy’s halo; Holland, Fahlman, & Richer (1996) have analyzed fields around two clusters, G302 ($R = 7$ kpc) and G312 ($R = 11$ kpc) near M31’s minor axis.⁵ The results of these *HST* studies are in good agreement with ground-based results despite the different contamination issues (see below). These studies find the mean metallicity of M31’s halo to be comparable to that of 47 Tuc ($[\text{Fe}/\text{H}] = -0.7$ dex), with a spread of nearly 2 dex, suggesting that there was a greater degree of pre-enrichment during the assembly of M31’s spheroid than in the case of the Galaxy’s spheroid.

While *HST*’s excellent angular resolution can distinguish stars from most of the background field galaxies, M31 disk red giants, foreground Galactic dwarf stars, and faint compact galaxies remain as possible contaminants in studies of the M31 halo. Many of the *HST* studies have targeted the relatively high surface brightness inner portions of the M31 halo (in order to include a reasonable number of stars within the limited field of view of the camera) but some of these regions are projected against M31’s bright inner disk so that the danger of contamination by M31 disk giants can be particularly high. Moreover, the lack of comparison field data in most of the *HST* studies makes it impossible to carry out statistical subtraction. For ground-based surveys on the other hand, even the most careful attempts at statistical subtraction of contaminants are hampered by field-to-field variations in photometric error, seeing, and the surface density of foreground stars and background galaxies, along with asymmetries in M31’s disk. Whether one uses *HST* for high angular resolution, or ground-based telescopes for their relatively large fields of view, sample

⁴Kitt Peak National Observatory of the National Optical Astronomy Observatories is operated by the Association of Universities for Research in Astronomy, Inc., under cooperative agreement with the National Science Foundation.

⁵We hereafter refer to these as the “G1 field”, “G302 field”, etc., because of their proximity to the corresponding M31 globular clusters, but should point out that the samples under discussion contain only field stars and no cluster members.

contamination remains the main obstacle in determining the true metallicity and metallicity spread in M31’s halo.

Spectroscopy of individual RGB stars in M31 is a powerful tool for measuring the metallicity of M31’s halo. With the advent of 8–10-m class telescopes such as the Keck telescope and efficient multi-object spectrographs such as LRIS, it is feasible to observe a sizeable sample of individual stars in M31. This paper describes spectroscopy of individual RGB star candidates in M31’s halo identified in the RGG study. Preliminary spectroscopic results have been presented in Reitzel & Guhathakurta (1998, 2000), Guhathakurta & Reitzel (1998), and Guhathakurta, Reitzel, & Grebel (2000). The selection of the sample, observations, and data reduction are described in §2, the kinematics of the sample in §3, and the measurement of the metallicity of M31’s halo in §4. We discuss the results in the context of other studies of the halo and model calculations in §5, and summarize the conclusions in §6.

2. Data

2.1. Spectroscopic Targets: M31 Red Giant Candidates and Control Sample

A sample of 99 objects has been targeted for spectroscopy from the RGG photometric study of the $R = 19$ kpc SE minor axis field. Of the 2078 objects in that study which have $UBRI$ colors and morphology consistent with a star, the subset of 284 objects in the apparent magnitude range $I = 20 - 22$ are likely to be bright red giants in M31 (the tip of the RGB is at $I_{\text{TRGB}} \approx 20.5$ at the distance of M31), and 99 of these are targeted for spectroscopy. The full color range is used in choosing the spectroscopic targets, so as to avoid biasing the metallicity determination: the shape of the $B - I$ color distribution of the 99 spectroscopic targets is identical to that of the parent sample of 284 objects. The distribution of apparent I -band magnitudes for the spectroscopic targets is slightly skewed in favor of bright stars relative to that of the parent sample within the range $I = 20 - 22$, reflecting the slightly higher priority given to brighter stars during the design of the multislit masks (the significance of this selection bias is discussed in §5.2). In the RGG work, an object is assigned a classification of “star-like” only if its color excess significance criterion $\delta < 1.5$ and angular size $\theta_{\text{FWHM}} < 1''.4$ for the KPNO image and $\theta_{\text{FWHM}} < 0''.7, 0''.8, 0''.9$, and $0''.9$ for the four Keck/LRIS images (see also Gould et al. 1992). Astrometric and photometric data for the 99 spectroscopic targets are presented in Table 1: positions (good to $\sim 0''.1$) are derived from several bright US Naval Observatory catalog astrometric reference stars present in this low-latitude field; $UBRI$ photometry is from RGG, while V magnitudes are synthesized from these data and model stellar isochrones (§4.2.2).

There are two objects in the list of spectroscopic targets that do not pass the above $UBRI$ and morphology selection criteria. This is due to the fact that these objects were selected before

the final refinements to the photometric and morphological selection were made in the RGG work. One of them, t1.01, barely fails the final color selection with $\delta = 1.55$, while the second, t2.22, fails the final morphological selection with $\theta_{\text{FWHM}} = 1''.5$ on the KPNO image. It turns out that both objects are likely foreground Galactic dwarf stars based on the fact that their radial velocities are close to zero (see § 3.2 and Table 3).

Spectra have also been obtained for 13 objects with $I < 20$, which places them well above the expected tip of M31’s RGB ($I_{\text{TRGB}} \approx 20.5$). These objects form a control sample of Galactic stars whose kinematical properties are compared to the Institute for Advanced Study Galaxy (IASG) star count model (Ratnatunga & Bahcall 1985) to aid in the rejection of foreground contaminants from the main sample of M31 halo giant candidates.

2.2. Observations

The spectra were obtained using the Keck II 10-m telescope and LRIS during two 2-night observing runs in 1996 October and 1997 October. These observing runs predate the installation of the blue side of LRIS, so the instrumental details given below refer to what is now the “red side” of LRIS. The observations were carried out in multi-slit mode with a typical slit mask having 20–30 slitlets on M31 halo RGB candidates and control sample stars. Each slitlet has a width of $1''.0$ and the typical slitlet length is $10''$. The 1200 lines mm^{-1} grating provides a dispersion of $0.62 \text{ \AA pixel}^{-1}$ and was used to cover the spectral range $\lambda\lambda 7550\text{--}8850 \text{ \AA}$ containing the near-infrared Ca II triplet: $\lambda\lambda 8498, 8542, \text{ and } 8662 \text{ \AA}$. The instrumental spectral/velocity resolution is $1.94 \text{ \AA}/68 \text{ km s}^{-1}$ (FWHM) or a Gaussian σ of $0.83 \text{ \AA}/29 \text{ km s}^{-1}$. This is based on a dispersion of $0.62 \text{ \AA pixel}^{-1}$, a $1''.0$ slit width, a pixel scale of $0''.215 \text{ pixel}^{-1}$ along the spatial direction, an anamorphic magnification factor of 0.565, and the best spectrograph focus of $\text{FWHM} \sim 1.7 \text{ pixel}$ (Phillips et al. 1997). The seeing FWHM was typically better than $1''.0$, so the actual velocity resolution is slightly better than the above estimate—e.g., $\sigma \sim 25 \text{ km s}^{-1}$ for $0''.8$ seeing. A slight dither of about $1''$ along the slit was done between exposures to help with fringe removal and to minimize the effect of bad pixels. Five multislit masks were used to obtain spectra with total exposure times t_{exp} of 3.8, 3.7, 4.5, 4.5, and 1.5 hr. Individual exposure times were typically 50 min long, although some exposures had to be truncated due to telescope and instrument problems. Detailed exposure information is presented in Table 2.

For the purpose of checking the metallicity calibration, a handful of red giants were observed in M79 and NGC 6791, two reference Milky Way star clusters. Short Keck/LRIS exposures in long-slit spectroscopic mode and broad-band imaging mode were obtained during twilight/dawn on the nights of the main M31 observations. The instrumental setup for these calibration star long-slit spectra is practically identical to the above setup used for the M31 multi-slit spectra, and the reduction procedure is essentially the same as for the main M31 data set (§ 2.3). The calibration

star cluster images are analyzed with DAOPHOT/ALLSTAR (Stetson 1987, 1992) to derive V magnitudes for the red giants for which we have spectra.

2.3. Data Reduction

The data are reduced using standard IRAF⁶ tasks and the spectral reduction program Expector (Kelson 2002). The main steps are summarized below, annotated by [I] for IRAF or [E] for Expector:

- [I] **Overscan subtraction** of the mean bias level is done for each raw CCD frame and the overscan region is then **trimmed** off. Two-dimensional **bias subtraction** is carried out using the median of several 1-s dark exposures.
- [I] **Cosmic ray** events (identified by object sharpness/peak pixel brightness) are masked, including a surrounding 1-pixel buffer zone to capture low level wings.
- [I] **Geometric distortion** in the images is mapped by tracing the boundaries between slitlets using night sky atmospheric emission lines in the M31 multislit spectral exposures (‘data frames’) and emission lines in short arc lamp calibration exposures. The distortion mapping and correction are done using the tasks IDENT, REIDENT, FITCOORDS, and TRANSFORM.
- [E] **Flat field and slitlet illumination corrections** are performed using a spectral dome flat that is well-matched to each data frame in terms of LRIS flexure effects. Mechanical flexure in LRIS can cause the location of a slitlet to shift by up to 2–3 pixels from image to image. Thus “flexure matching” requires that the dome flat observations be obtained at the same telescope elevation angle and instrument rotator angle as the data frame to ensure the same orientation of LRIS with respect to the gravity vector. The matched spectral dome flat is corrected for geometric distortion as described above. The ‘slit function’ for each slitlet is obtained by collapsing along the dispersion direction (via median-filtering) the corresponding band in the rectified spectral dome flat. The ‘slit function image’, a composite of the slit illumination functions of all the slitlets, is then applied to the spectral dome flat. This produces a map of the Fabry-Perot fringe pattern and fixed-pattern quantum efficiency variations which is divided into the data frame to achieve pixel-to-pixel flat fielding. The slit function image is shifted to empirically match each data frame (to account for any difference in mechanical flexure) before it is used to apply the slitlet illumination correction.
- [E] **Wavelength calibration** is based on numerous night sky emission lines (of known wavelength) in the Ca II portion of the spectrum. An independent wavelength solution is derived

⁶IRAF is distributed by the National Optical Astronomy Observatories, which are operated by the Association of Universities for Research in Astronomy, Inc., under cooperative agreement with the National Science Foundation.

for each slitlet on a given multislit spectral frame, and all slitlets are transformed to a common wavelength grid. The exact wavelength coverage for a slitlet varies with position along the dispersion axis within the multislit mask—i.e., its CCD column number in a direct image of the mask—but all slitlets cover all three lines of the Ca II triplet, even after allowing for Doppler shifts of $\pm 5000 \text{ km s}^{-1}$.

[E] **Sky subtraction** is a critical step because of the large number of strong emission lines in this spectral region. Each slitlet is visually inspected and ‘sky windows’ (ranges of row numbers) are defined on either side of the intended target for that slitlet, taking care to avoid the point spread function wings of the target and contamination from bright neighboring objects. The mean sky spectrum at the location of the target is linearly interpolated by collapsing the rows within the sky windows, after clipping out $\sim 10\%$ of the highest and lowest pixel values. Flexure in LRIS can cause slight differences in the fringe pattern between data frame and dome flat which are not accounted for in the above procedure; this occasionally manifests itself in the form of large, systematic residuals in the vicinity of the brightest sky lines.

[I] **Extraction** of one-dimensional spectra (one target per slitlet) is carried out on each sky-subtracted multislit exposure. A 16-pixel-wide ‘target window’ is defined centered on each target, and the rows are collapsed into a weighted average using the optimal scheme described by Horne (1986). The 1-D extracted spectra are normalized by dividing by their mean continuum level. The individual normalized 1-D spectra of a given target (one per exposure) are **coadded** by weighted averaging, with the weight being the inverse of the square of the typical photon noise in a clean part of the spectrum.

Figure 1 shows the spectra and corresponding uncertainty levels for two representative targets in our sample, along with a typical night sky spectrum. The night sky spectrum is dominated by bright emission lines all across the region of the near-infrared Ca II triplet. The trio of absorption lines is clearly visible in the spectrum of the bright object ($I = 20.7$) and the two strongest lines ($\lambda\lambda 8542$ and 8662 \AA) are visible in the spectrum of the faint object ($I = 21.7$). The rest wavelengths of the Ca II absorption lines are indicated by the bold lines below the spectra. The Ca II lines for both objects are shifted to the blue, as might be expected for RGB stars in M31: $v_{\text{obs}} = -173 \text{ km s}^{-1}$ (bright object) and $v_{\text{obs}} = -500 \text{ km s}^{-1}$ (faint object). The 1σ error in the mean spectrum of a given target is empirically estimated to be rms/\sqrt{N} , where ‘rms’ is the weighted rms scatter about the weighted mean of the individual spectra extracted from the N independent exposures of the same object. The rms is not computed for objects on multislit mask #5 as the number of independent exposures N is only 2 (Table 2). The night sky spectrum is useful for identifying regions where sky subtraction is problematic; the rms for each object increases at the locations of the bright emission lines because of increased Poisson noise and residual fringing. Away from these bright night sky emission lines, the S/N ratio per pixel is $\gtrsim 20$ for the bright object and in the range 10–20 for the faint one.

A variety of factors play a role in determining how well the strength and position (i.e., radial velocity) of the Ca II absorption line triplet are measured for a given target. In addition to the usual dependence of the Poisson error on the target’s apparent I -band magnitude, absorption line strength, and effective exposure time, there are several possible sources of systematic error: large residuals at the locations of bright night sky emission lines because of imperfect fringe removal (typically due to differential LRIS mechanical flexure and/or slight wavelength mismatch between data frame and corresponding dome flat); scattered light/spectral ghosts; poor seeing; focus variations across the field of view of the mask; miscentering of a target within the slitlet due to errors in astrometry and/or slitmask misalignment; and the occasional placement of a target near the end of the slitmask which causes its spectrum to land near the edges of the CCD making sky subtraction and extraction of the spectrum problematic.

2.4. Cross-Correlation Analysis

In order to determine the radial velocity and Ca II line strength of each object, its final coadded spectrum is cross-correlated against a template spectrum. The cross-correlation function (CCF) is computed from -1000 to $+1000$ km s $^{-1}$, covering a plausible range of radial velocities for stars associated with M31. The cross-correlation technique yields an unambiguous peak and a reliable radial velocity for 80 of the 99 objects comprising the main sample of M31 targets and all 13 control objects. The CCF for each object is shown in Fig. 2.

Tests show that the strength, significance, and position of the CCF peak are insensitive to the exact choice of template (e.g., red giant vs. dwarf star), which is understandable given that the CCF signal is driven almost entirely by the three lines of the Ca II triplet whose relative strengths and line shapes are the same across these templates at the relatively low resolution of our spectra. The template used in the rest of this paper is the average spectrum of three bright control sample stars, each of which is shifted to the rest frame (zero velocity) before coaddition. The template is masked so that only a window around each of the three Ca II lines is used in the cross-correlation analysis, where the window size is optimized to maximize the S/N ratio in the resulting CCF.

Of the 19 objects for which the CCF fails to yield a reliable velocity, 8 have apparent magnitudes $I < 21.4$ and have relatively high S/N spectra, while 11 have $I > 21.4$ and are generally characterized by lower S/N data. A brief description of the objects is given here; they are excluded from the rest of the analysis in this paper.

The slitlet for one of the brighter objects, t1.27, happens to be at one end of mask 1 and its spectrum falls at the edge of the CCD frame causing spectral extraction to fail (bold solid horizontal line in bottom right panel of Fig. 2). The remaining 7 higher S/N objects display a wide range of colors, $1.5 \leq B - I \leq 4.5$, and each appears to have a featureless continuum. Most of these objects are likely to be distant compact background field galaxies for which the Ca II lines and any other prominent spectral features happen to have been redshifted out of the observed wavelength range.

This would correspond to residual background galaxy contamination at the level of $\approx 5\%$ – 10% in the RGG *UBRI* color- and morphology-selected sample from which the spectroscopic targets are drawn. A couple of the reddest objects might possibly be foreground Galactic late-M dwarfs; their spectra tend to be a poor match to the cross-correlation template, lacking the three Ca II absorption lines in particular, and the resulting CCF contains no peak at the true radial velocity of the object (or at any other velocity for that matter). None of these 7 higher S/N objects is likely to be an M31 RGB star or else the Ca II triplet lines would have been obvious (as they are for the brighter object in Fig. 1).

The 11 lower S/N objects, like their higher S/N counterparts, show a large spread in color, $1.6 \leq B - I \leq 3.9$. Nine of the 11 contain no identifiable spectral emission/absorption features that are significantly above/below the continuum with respect to the noise. One object with $I = 21.81$ and $B - I = 2.13$ (object ID t5.24 in Tables 1 and 3) shows very faint absorption features that may well be the Ca II triplet at a radial velocity of $v = -330 \text{ km s}^{-1}$, which would make this object an RGB star in M31 (§ 3.2). The last of these 11 lower S/N objects for which there is no reliable velocity measurement is object t4.14 with $I = 21.78$ and $B - I = 2.47$. It appears to have *two* sets of Ca II triplet absorption lines, with radial velocities of $v = -435$ and -147 km s^{-1} ; this object is probably a chance alignment of two stars, an M31 RGB star and a foreground Galactic dwarf star, respectively (see § 3.2). Inspection of the Keck/LRIS *I*-band image reveals a slightly elongated object; the object is not resolved into two separate peaks, and its ellipticity is not large enough for it to fail the stellar morphological selection criterion as it is within the range of values produced by focus variations across the image.

The standard Tonry-Davis (1979) parameter, $r_{\text{TD}} = h/(\sqrt{2}\sigma_{\text{CCF}})$, is computed for each CCF, where h is the height of the CCF peak and σ_{CCF} is the rms noise in the CCF. For 80 of the 99 objects comprising the main sample of M31 targets and all 13 control objects, there is an unambiguous peak in the CCF from which h is calculated; for the 19 targets for which there is no clear peak in the CCF, the highest point in the CCF is used to determine h . A linear baseline is fit to the CCF after excluding a window of width $\Delta v = 450 \text{ km s}^{-1}$ centered on the CCF peak. The peak height h and rms (and the area under the CCF peak, A_{CCF} —see § 4.2.2) are calculated relative to this baseline, with the window around the peak excluded from the rms calculation. The CCF baseline is typically flat and close to zero (Fig. 2) so the results are independent of the details of the baseline fit. The r_{TD} parameter for each object is listed in Table 3. The 80 objects in the main M31 target sample for which the radial velocity determination is successful have a mean significance level of $\langle r_{\text{TD}} \rangle = 5.75$, while $\langle r_{\text{TD}} \rangle = 11.01$ for the 13 objects in the control sample. By contrast, the significance level is far lower on average for 18 of the 19 targets (excluding t1.27) for which the radial velocity measurement fails: $\langle r_{\text{TD}} \rangle = 2.07$.

3. Kinematics

The radial velocity determined from the location of the CCF peak, v_{obs} , is corrected to the heliocentric frame using the task RVCOR in IRAF. The v_{hel} values for 80 of the 99 objects comprising the main sample of M31 targets and all 13 objects in the control sample are listed in Table 3. This section describes: empirical determination of the velocity measurement error; isolation of a secure sample of M31 RGB stars using radial velocity and (in a few cases) color information; and the dynamics of M31’s stellar halo.

3.1. Velocity Measurement Error

The measurement error in radial velocity is investigated by splitting the data for each target in masks 1-4. A total of 80 objects is used in this analysis, all of them M31 spectroscopic targets; the control sample objects are excluded from this analysis. For each of these objects, the four longest available exposures are combined into two independent coadds of two exposures each. Each of these coadds is hereafter referred to as a “coadded pair”. Reliable radial velocities are measured for both coadded pairs for 58 objects, while the velocity measurement fails for at least one of the two coadded pairs for the remaining 32 objects. The failure rate for the coadded pairs ($\approx 30\%$) is higher than the failure rate for the full coadds ($\approx 20\%$). As discussed in § 2.4, faint galaxies and Galactic M dwarfs account for about 10% of the failed measurements in the case of the full coadds, and the measurement would of course fail again for these objects in the case of the coadded pairs. The rate of failure due to insufficient S/N in the spectrum is expected to increase for the coadded pairs (compared to the full coadds) given the reduction in effective exposure time by over a factor of two.

The two independent velocity measurements for a given object, derived from its two coadded pairs, are differenced. The cumulative distribution of velocity differences for various subsamples of objects is shown in Fig. 3 along with the best-fit Gaussian. The velocity measurement accuracy is slightly greater for the brighter half of the sample (29 objects in the range $20 < I < 21.1$) than for the fainter half (29 objects in the range $21.1 < I < 22$): the rms velocity difference of the coadded pairs is $\sigma_v^{\text{pair}}(\text{bright}) = 22.8 \text{ km s}^{-1}$ and $\sigma_v^{\text{pair}}(\text{faint}) = 28.0 \text{ km s}^{-1}$, respectively. The strength of the Ca II absorption line triplet (characterized here by A_{CCF} —see § 4.2.2) does not have much of a bearing on the velocity measurement accuracy: $\sigma_v^{\text{pair}}(\text{strong-lined}) = 26.8 \text{ km s}^{-1}$ versus $\sigma_v^{\text{pair}}(\text{weak-lined}) = 24.1 \text{ km s}^{-1}$ for stars with line strengths greater/less than the median value, respectively. As discussed in § 2.3 above, a large number of factors can influence the data quality so it is no surprise that the velocity measurement error does not correlate with line strength.

Despite these complicating factors, we make the simplifying assumption that the velocity measurement error for any given target scales as $t_{\text{exp}}^{-1/2}$. The exposure time for the coadded pairs

ranges from 1.42–1.75 hr. A typical coadded pair exposure time of $t_{\text{exp}}^{\text{pair}} = 1.7$ hr is adopted for the velocity measurement error calculation; this is at the high end of the actual range implying that the velocity error is slightly overestimated in our calculation. The rms of velocity differences for the entire sample of coadded pairs is $\sigma_v^{\text{pair}}(\text{all}) = 25.4 \text{ km s}^{-1}$. The average velocity measurement uncertainty for the targets, based on the full coadd of the total available exposure time, is therefore expected to be:

$$\langle \sigma_v^{\text{tot}} \rangle = [\sigma_v^{\text{pair}}(\text{all})/\sqrt{2}] \sqrt{t_{\text{exp}}^{\text{pair}}/t_{\text{exp}}^{\text{tot}}} \quad (1)$$

where $t_{\text{exp}}^{\text{tot}}$ is the total exposure time for the mask in question (see Table 2). The mean 1σ error in velocity is approximately 12 km s^{-1} for targets in masks 1–4 and 19 km s^{-1} for those in mask 5.

The velocity measurement error for an individual target is expected to scale as: $\sigma_v^{\text{ind}} = \sigma_v^{\text{TD}}(1 + r_{\text{TD}})^{-1}$ (Tonry & Davis 1979). The velocity differences of the coadded pairs for the 58 targets are scaled following Eq. 1 to reflect the reduction of velocity error that is expected to result from the coaddition of all the exposures:

$$\Delta v_{\text{scaled}} = [\Delta v_{\text{pair}}/\sqrt{2}] \sqrt{t_{\text{exp}}^{\text{pair}}/t_{\text{exp}}^{\text{tot}}} \quad (2)$$

These scaled velocity differences are plotted versus $(1 + r_{\text{TD}})^{-1}$ in Fig. 4. The Tonry-Davis velocity error parameter σ_v^{TD} is equal to the rms of the quantity $\Delta v_{\text{scaled}}(1 + r_{\text{TD}})$; its value is empirically determined to be 77 km s^{-1} (solid lines), comparable to the instrumental velocity resolution (§ 2.2).

3.2. Defining a Secure Sample of M31 Red Giants

Kinematical information derived from spectroscopy is useful for isolating M31 halo red giants and rejecting contaminants. The *UBRI* color- and morphology-based selection in the RGG study removes most (though not all) of the background field galaxies, but stellar contaminants in the form of foreground Milky Way dwarf stars and M31 disk red giants remain in the spectroscopic target sample. Halo RGB stars in M31 are expected to span a large range of radial velocities (due to their random motion within the gravitational potential) centered on the galaxy’s systemic velocity, $v_{\text{sys}}^{\text{M31}} = -297 \text{ km s}^{-1}$ (de Vaucouleurs et al. 1991). On the other hand, if M31 disk RGB stars are present in this field, they are expected to be tightly clustered around a single velocity given the small field of view of our study. This velocity is expected to be close $v_{\text{sys}}^{\text{M31}}$ as our field of study is on the minor axis, so that the disk rotation velocity vector is in the plane of the sky with a zero line-of-sight component.

The typical contaminating foreground Galactic star in the sample is a K dwarf with colors of $B - V \approx V - I \approx 1.5$ (Fig. 6), corresponding to an absolute magnitude of $M_V \approx 7-8$. At apparent magnitudes of $I \sim 21$ or $V \sim 22.5$, in the middle of the range from which the spectroscopic targets are selected, this implies a distance modulus of $(m - M)_V^0 \approx 15$ or $D \approx 10 \text{ kpc}$. Such a star would be a few kpc out of the plane— $\sin(b) = 0.37$ for the Galactic latitude of M31—presumably in the thick disk of the Milky Way, with a small but negative radial velocity (the projection of the

thick disk rotation curve along the line of sight to M31 minus the projection of the Solar rotational speed). Redder foreground stars (late-K to M dwarfs) in a similar apparent magnitude range are somewhat less luminous than the star in the above example and are thus only a few kpc away; bluer stars (near the main-sequence turnoff for an old population) are about an order of magnitude more luminous ($M_V \approx 4-5$), which places them a few tens of kpc away in the Galaxy’s halo, with more negative radial velocities due to the reflex of the projected Solar motion.

The distribution of radial velocities measured from the Keck/LRIS spectra is shown in Fig. 5. There is a clear peak at $\lesssim 0 \text{ km s}^{-1}$ superimposed on a broader distribution plausibly centered on M31’s systemic velocity. The IASG star-count model of the Galaxy (Ratnatunga & Bahcall 1985) is used to estimate the radial velocity distribution expected for foreground Milky Way dwarf stars along this particular line of sight and for the given apparent I magnitude range. A linear combination of the IASG model v distribution and a Gaussian centered on M31’s systemic velocity of -297 km s^{-1} provides an adequate fit to the data (solid curve). The fraction of M31 halo stars in our sample is estimated to be $\approx 43 \pm 6\%$.

The spectroscopic control sample consists of stars in the apparent magnitude range $I < 20$, significantly brighter than I_{TRGB} at the distance of M31 (Fig. 6). *A priori*, these stars are likely to be Milky Way dwarf stars and form a good sample of objects with which to test the IASG model predictions. The observed radial velocity distribution of the spectroscopic control sample is more or less consistent with the IASG model prediction, although there appears to be a $20 - 50 \text{ km s}^{-1}$ offset between the two distributions with the former being more negative (solid histogram vs. dotted curve in the lower panel of Fig. 5). A similar offset between model and observed v distributions also appears to be present in the main M31 target sample (upper panel).

The Gaussian plus IASG model fit to the velocity distribution of the main sample of M31 targets is used to estimate the fractional foreground contamination within various radial velocity ranges. For example, the Galactic dwarf fraction in the sample is expected to be: 8% for $v < -220 \text{ km s}^{-1}$, 76% for $v > -220 \text{ km s}^{-1}$, 12% for $v < -160 \text{ km s}^{-1}$, 84% for $v > -160 \text{ km s}^{-1}$, and nearly 100% for stars with $v > -50 \text{ km s}^{-1}$. The lack of any substantial concentration of objects at $v_{\text{sys}}^{\text{M31}}$ in Fig. 5 indicates that there are few (if any) M31 disk giants in the sample, but this issue will be revisited later (§5.3). For a start, selecting the 25 stars with $v < -220 \text{ km s}^{-1}$ is likely to yield mostly M31 halo RGB stars with minimal contamination from Milky Way dwarf stars (at the level of only $\approx 8\%$ or 2 stars out of 25; see §4.3).

Figure 6 shows an I vs. $B - I$ CMD for all color- and morphology-selected stellar candidates in the $R = 19 \text{ kpc}$ minor axis M31 field based on the earlier photometric study by RGG. The main sample of M31 spectroscopic targets and control sample (representative subset of the stellar candidates in the range $20 < I < 22$ and $I < 20$, respectively) are shown as special symbols indicating each object’s radial velocity. It is reassuring to find that the radial velocity information and the distribution of objects on the CMD tell a consistent story. As discussed above, the control sample is a clear example of this: the photometric selection criterion indicates these objects should

be foreground Galactic dwarf stars and they all turn out to have $v > -160 \text{ km s}^{-1}$ in keeping with the IASG model prediction for such stars. The sample of 25 stars with $v < -220 \text{ km s}^{-1}$ is another example: these stars have large enough negative velocities for them to be likely M31 red giants and indeed they occupy a portion of the CMD that is bracketed by model RGB tracks at the distance of M31 spanning a plausible range of metallicities.

A similarly consistent picture emerges for the foreground Galactic dwarf stars present within the main spectroscopic target sample. Over the apparent magnitude range of interest ($I \sim 18\text{--}22$), this dwarf population contains stars with a variety of masses, absolute magnitudes, and effective temperatures, with a broad and nearly uniform color distribution from $1 \lesssim B - I \lesssim 4.5$: see the control sample with $I < 20$ in Fig. 6 and the comparison field data and IASG model predictions in RGG [Figs. 8(b–d) of that paper]. The IASG model predicts that most of the objects with $v > -160 \text{ km s}^{-1}$ in the main spectroscopic sample are Galactic dwarfs. As expected, the stars in this radial velocity range are found to span the full range of $B - I$ colors in the CMD (Fig. 6) and do not appear to be particularly strongly concentrated in the subsection of the CMD bracketed by the M31 model RGB tracks. Moreover, the $20 < I < 20.5$ portion of the CMD should be largely free of M31 giants since it is above the nominal tip of the RGB; as expected, 10 out of the 12 stars with reliable velocity measurements within this I magnitude range of the main sample have $v > -160 \text{ km s}^{-1}$ (Fig. 6).

The $B - I$ and $R - I$ color distributions are compared in Figs. 6 and 7. The foreground Galactic dwarf population spans the full width of both CMDs with a near-uniform distribution. The theoretical M31 RGB tracks have somewhat different shapes and locations relative to this foreground population in the two CMDs. As expected, secure M31 giants with $v < -220 \text{ km s}^{-1}$ are shifted further to the blue in $(R - I, I)$ than in $(B - I, I)$ relative to the rest of the data points. It should be noted that $R - I$ is not a good choice of color for metallicity discrimination: color measurement errors are more prominent in Fig. 7 than in Fig. 6, so it is not surprising that $\sim 20\%$ of the secure M31 halo giants with $v < -220 \text{ km s}^{-1}$ scatter blueward of the models in the former CMD.

The situation is somewhat more complicated for stars in the intermediate radial velocity range, $-220 < v < -160 \text{ km s}^{-1}$, and bears closer examination. Five of the 9 intermediate velocity stars have $B - I < 2$ which implies that they are too blue to be M31 red giants (Fig. 6). Following our earlier discussion, foreground stars in this color range are expected to be distant turnoff stars in the halo of the Milky Way, so it is only natural for them to have a substantial negative velocity due to the reflex of the Solar rotation vector projected in the direction of M31 ($\approx -175 \text{ km s}^{-1}$). Figure 8 shows the IASG model prediction for the radial velocity distribution of dwarfs with $B - I < 2$ versus those with $B - I > 2$ (the relative scaling of the two curves is arbitrary). The blue subset of Galactic dwarfs is expected to have the following velocity distribution: 1 star with $v < -220 \text{ km s}^{-1}$, 2 with $-220 < v < -160 \text{ km s}^{-1}$, and 7 with $v > -160 \text{ km s}^{-1}$. The observed numbers of stars with $B - I < 2$ in these velocity ranges are: 0, 5, and 4 stars, respectively (see Fig. 6), and are entirely consistent with model predictions given the (large) Poisson uncertainties and measurement errors

in radial velocity and color. Galactic dwarf stars with $B - I > 2$ on the other hand are expected to lie almost exclusively in the velocity range $v > -160 \text{ km s}^{-1}$ (solid curve in Fig. 8).

Thus, the 4 stars in the sample with $B - I > 2$ and with measured radial velocities in the range $-220 < v < -160 \text{ km s}^{-1}$ (Fig. 6) are almost certainly M31 giants; these stars are hereafter referred to as the “red intermediate-velocity stars”. These 4 stars are added to the 25 stars with $v < -220 \text{ km s}^{-1}$ (selected on the basis of radial velocity alone) to construct a *secure sample of 29 M31 red giants*. Unless otherwise mentioned, the rest of the analysis in this paper is restricted to this secure M31 sample. We recognize that even this ‘secure’ M31 sample might contain a couple of non-M31 stars; one such star is discussed in § 4.3. The secure sample probably contains about 80% of all the M31 red giants in the spectroscopic sample: of the 80 stars with reliable radial velocity measurements, 35 or so are expected to be M31 RGB stars (based on the IASG model fit to the velocity distribution), and of these about 27 or 28 are included in the secure sample. The remaining 7 or 8 M31 giants outside the secure sample are discussed in § 4.3.

3.3. Halo Dynamics

Individual field stars in M31’s halo serve as excellent dynamical tracers of the mass distribution in the galaxy. The IASG model plus Gaussian fit to the observed radial velocity distribution of the main M31 spectroscopic sample yields a best-fit Gaussian width of $\sigma_v^{\text{M31}} = 150_{-30}^{+50} \text{ km s}^{-1}$ (90% confidence limits). The velocity dispersion of M31’s halo can be determined more directly from the data, as long as one takes care to avoid the foreground Galactic dwarf contaminants. The 16 stars with $v < v_{\text{sys}}^{\text{M31}}$ are all likely to be M31 giants according to the IASG model. The rms dispersion of these stars with respect to $v_{\text{sys}}^{\text{M31}}$ is 125 km s^{-1} , in good agreement with the best-fit Gaussian width.

The centroid of the Gaussian is held fixed during the fit at $v_{\text{sys}}^{\text{M31}} = -297 \text{ km s}^{-1}$, the expected mean velocity of the halo in this minor axis field. As such, the data show no evidence for an offset between the mean velocity of M31 stars and $v_{\text{sys}}^{\text{M31}}$ —i.e., there is no sign of rotation along the minor axis. It is difficult, however, to pin down an exact upper limit for the minor axis rotation of M31’s halo from these data because of the high degree of Galactic dwarf contamination all of which appears on one side of $v_{\text{sys}}^{\text{M31}}$.

Our measurement of the line-of-sight velocity dispersion of M31 field halo giants in this $R = 19 \text{ kpc}$ field is in excellent agreement with other dynamical tracers located at a comparable distance from the galaxy’s center (cf. Evans & Wilkinson 2000, and references therein). The published radial velocities of 17 M31 globular clusters with $R > 20 \text{ kpc}$ yield a line-of-sight velocity dispersion of 158 km s^{-1} at an average projected distance from M31’s center of 23.8 kpc . The published velocities of 9 planetary nebulae with $R > 18 \text{ kpc}$ in M31’s halo yield a dispersion of 145 km s^{-1} at an average/median projected distance of $\langle R \rangle \sim 20 \text{ kpc}$.

The above estimates for the velocity dispersion of M31’s halo are somewhat low compared to

the dispersion observed for various Milky Way halo populations, and this may appear surprising at first. The reader is referred to some recent work on the dynamical modeling of the Milky Way and M31 by Wilkinson & Evans (1999), Evans & Wilkinson (2000), and Evans et al. (2000) that used the latest and most complete information available on the HI rotation curve of the disk and radial velocities of dwarf satellite galaxies, globular clusters, and planetary nebulae. They conclude that, contrary to popular belief/intuition, M31 is probably *less* massive than the Milky Way.

4. Stellar Metallicity Measurements

This section describes the measurement of the metallicities of individual M31 RGB stars using two different methods, one based on photometric data and the other based primarily on spectroscopic data. The photometric technique compares the position of each star in the $(B - I, I)$ CMD to a set of theoretical RGB tracks covering a wide range of metallicities. The spectroscopic technique is based on the weighted sum of the equivalent widths of the Ca II triplet of absorption lines, which is converted to $[\text{Fe}/\text{H}]$ via two separate empirical calibration relations derived from Galactic globular cluster red giants. Estimates are made of the measurement uncertainties (both random and systematic) in the photometric and spectroscopic methods.

Both methods implicitly *assume* that the object whose metallicity is being measured is a red giant at the distance of M31. It has already been noted though that more than half of the stars in the full sample of M31 targets are probably foreground Galactic dwarf stars (§ 3.2), so the techniques, especially the photometric one, will yield nonsensical results for these stars. While the 29 stars comprising the secure M31 sample are almost certainly red giants in M31, we expect a handful of additional M31 red giants to be hidden in the rest of the sample. Even with the photometric and radial velocity information we have in hand, it is generally difficult, if not impossible, to tell whether a *particular* star is an M31 giant or a Galactic dwarf. We have therefore decided to blindly apply the photometric technique to all 99 stars in the main M31 spectroscopic target sample and the spectroscopic technique to the subset (80 out of 99) for which there is a reliable measurement of the Ca II lines. Metallicity measurements are not made for the 13 stars comprising the control sample as they are definitely Galactic dwarfs.

4.1. Photometric Estimates

4.1.1. Method

The apparent/observed I magnitude and $B - I$ color of each star are corrected for extinction and reddening, respectively, using the Schlegel, Finkbeiner, & Davis (1998) $E(B - V)$ map and the relation: $E(B - I) = 2.4 E(B - V)$, which is based on the standard Galactic dust extinction law with $R_V = 3.1$ (Cardelli, Clayton, & Mathis 1989). The extinction-corrected apparent I magnitude

is converted to an absolute magnitude, M_I , based on our adopted M31 distance of 783 kpc (Stanek & Garnavich 1998; Holland 1998) or a true distance modulus of $(m - M)_0 = 24.47$. The absolute I -band magnitude and $B - I$ color are then compared to a set of theoretical RGB tracks in the CMD: 17 model isochrones from Bergbusch & Vandenberg (2001) with metallicities spanning the range $-2.3 \leq [\text{Fe}/\text{H}] \leq -0.3$ dex, $[\alpha/\text{Fe}] = +0.3$ dex, and age $t = 14$ Gyr (four of which are shown in Figs. 6 and 7), along with two model isochrones from the Padova group (Girardi et al. 2000) with $[\text{Fe}/\text{H}] = -0.02$ and $+0.18$ dex and $t = 14.3$ Gyr constraining the high-metallicity end. A fourth-order spline is used to interpolate between isochrones and this yields a photometric estimate of the star’s metallicity, $[\text{Fe}/\text{H}]_{\text{phot}}$. These estimates are listed in the last column of Table 3. For stars located to the left of (bluer than) the most metal-poor isochrone in the $(B - I, I)$ CMD shown in Fig. 6, the $[\text{Fe}/\text{H}]_{\text{phot}}$ estimate should be regarded as highly uncertain as it is derived by extrapolation; only one of the stars with $v < -220$ km s $^{-1}$ in the secure sample of M31 giants, object ID t3.12, is in this category, and we conclude in § 4.3 that this object is possibly a foreground Galactic dwarf.

We have chosen to apply reddening/extinction corrections on a star-by-star basis: the angular resolution of the Schlegel et al. maps is high enough ($\sim 2'$) to account for variations in the dust optical depth across the $15' \times 15'$ region of the sky from which the stars are drawn: $0.12 < E(B - I) < 0.14$. For the sake of illustration only, the four model RGB tracks shown in Figs. 6 and 7 have been reddened by a typical amount of $\langle E(B - I) \rangle = 0.13$ while the data points represent the raw, uncorrected measurements. The $[\text{Fe}/\text{H}]_{\text{phot}}$ measurement procedure is exactly the opposite of this though: it involves applying a reddening/extinction correction to the photometry of each star and comparing it to the original, unreddened model isochrones.

While the $[\text{Fe}/\text{H}]_{\text{phot}}$ measurements in this paper are based largely on the Bergbusch & Vandenberg (2001) isochrones, it should be noted that the older Padova isochrones (Bertelli et al. 1994) were used for the definition of the $UBRI$ color-based selection regions in the RGG work. The former set of isochrones are favored here as they are computed over a finer grid of metallicities. The two sets of isochrones are in very good agreement in color-color space, so there is no inconsistency between photometric selection of stellar candidates and photometric measurement of their metallicity.

4.1.2. Measurement Errors

The photometric errors (RGG) and uncertainty in the distance modulus are used to compute an error ellipse for each star in the $(B - I, I)$ CMD. The major axis of the error ellipse is tilted in general because the photometric errors in $B - I$ and I are correlated. The distance modulus error is arbitrarily assumed to be 0.1 mag and is added in quadrature to the y -axis alone. The resulting photometric-cum-distance error ellipse for a star represents its probability distribution in $(B - I, I)$ space; this is used as a weighting function to calculate the weighted average and rms in $[\text{Fe}/\text{H}]_{\text{phot}}$ over the area of the error ellipse within 5σ of a star’s location in the CMD. The

difference between the weighted average $[\text{Fe}/\text{H}]_{\text{phot}}$ and the value derived from the nominal CMD location (most probable I and $B - I$) of a star is typically only ≈ 0.03 dex; the weighted average is what is used throughout the rest of this paper.

The weighted rms represents the error in $[\text{Fe}/\text{H}]_{\text{phot}}$ due to errors in photometry and distance modulus. It does *not* take into account possible errors in the theoretical RGB tracks—e.g., any mismatch between the $UBRI$ photometric system adopted in the model computation versus that used in the RGG stellar photometry. The average error in $[\text{Fe}/\text{H}]_{\text{phot}}$ for 28 of the 29 secure M31 RGB stars within the range of the model isochrones is 0.19 dex. Extrapolation of the spline fit to the isochrones suggests that the error is nearly twice as large, 0.36 dex, for objects that lie just blueward of the calibrated range due to the fact that the lowest-metallicity isochrones tend to crowd together in the CMD so that a given color error corresponds to a larger error in metallicity. The error in $[\text{Fe}/\text{H}]_{\text{phot}}$ is not easily quantifiable for objects that lie well beyond the range of the isochrones.

4.2. Spectroscopic Estimates

4.2.1. Outline of the Method

The Ca II triplet of absorption lines, $\lambda\lambda 8498, 8542, \text{ and } 8662 \text{ \AA}$, are among the strongest features in the near-infrared portion of the spectrum for most late-type stars and have been widely utilized. Early studies took advantage of the dependence of the equivalent width of the Ca II lines on surface gravity, $\log g$, to discriminate between giant and dwarf stars (Spinrad & Taylor 1969, 1971; Anderson 1974). Subsequently, Diaz, Terlevich, & Terlevich (1989) used the Ca II lines to measure metallicity, as most of the variation in line strength is due to a linear combination of $\log g$ and $[\text{Fe}/\text{H}]$, with little dependence on T_{eff} . Since then many groups have used this dependence and found good correlations with other metallicity indicators (Armandroff & Zinn 1988; Da Costa & Seitzer 1989; Olszewski et al. 1991; Suntzeff et al. 1992). Armandroff & Da Costa (1991) developed a method to rank red giant stars by $[\text{Fe}/\text{H}]$ which is independent of distance and reddening. We have chosen to adopt this method as have many others (Armandroff, Da Costa, & Zinn 1992; Da Costa, Armandroff, & Norris 1992; Suntzeff et al. 1993; Geisler et al. 1995; Da Costa & Armandroff 1995; Suntzeff & Kraft 1996; Rutledge et al. 1997a; Rutledge, Hesser, & Stetson 1997b).

While the details of the method are described in Armandroff & Da Costa (1991), there have been subsequent improvements to the calibration relations (Rutledge et al. 1997a). The basis of the method lies in the fact that the combined equivalent width (strength) of the Ca II lines depends primarily on metallicity, but also has some dependence on the luminosity of the red giant (relative to the horizontal branch say: $V_{\text{HB}} - V$). This is due to the fact that both $\log g$ and T_{eff} decrease as one moves up the RGB at a fixed metallicity. The combined equivalent width of the Ca II triplet is defined to be the weighted sum of the equivalent widths of the three individual lines

(Rutledge et al. 1997a):

$$\Sigma\text{Ca} \equiv 0.5 \text{EW}(\lambda 8498 \text{ \AA}) + 1.0 \text{EW}(\lambda 8542 \text{ \AA}) + 0.6 \text{EW}(\lambda 8662 \text{ \AA}) \quad (3)$$

The observed equivalent width, ΣCa , is translated to a ‘reduced’ equivalent width, W' , by correcting it to a common value of $\log g$ (Rutledge et al. 1997b):

$$W' = \Sigma\text{Ca} - 0.64(V_{\text{HB}} - V) \text{ \AA} \quad (4)$$

The reduced equivalent width is converted to a metallicity estimate using two separate calibration relations (Rutledge et al. 1997b). The first is a cubic relation:

$$[\text{Fe}/\text{H}]_{\text{ZW}} = -3.005 + 0.941 W' - 0.312 (W')^2 + 0.0478 (W')^3 \text{ dex} \quad (5)$$

for the Zinn & West (1984, hereafter referred to as Zinn-West or simply ZW) metallicity scale and is calibrated over the range $-2.3 \leq [\text{Fe}/\text{H}]_{\text{ZW}} \leq -0.3$ dex. The second is a linear relation:

$$[\text{Fe}/\text{H}]_{\text{CG97}} = -2.66 + 0.42 W' \text{ dex} \quad (6)$$

for the metallicity scale based on the high-dispersion spectroscopic studies of Carretta & Gratton (1997, hereafter referred to as Carretta-Gratton or simply CG97), and is calibrated over the range $-2.2 \leq [\text{Fe}/\text{H}]_{\text{CG97}} \leq -0.6$ dex.

4.2.2. From Cross Correlation to Metallicity

The strength of the CCF peak is an excellent diagnostic of the strength of the Ca II absorption line triplet. Tests using simulated, noisy spectra show that: (1) the area under the CCF peak, A_{CCF} , is a more robust measure than the peak height h since the width of the CCF peak can vary from exposure to exposure due to variations in seeing/guiding errors and even from star to star on a given exposure due to focus variations; and (2) A_{CCF} is less affected by noise than direct measurements of the equivalent width since the former is essentially based on a matched-filter technique which optimizes the S/N ratio of the measurement. We have therefore opted to estimate the line strength ΣCa by appropriate scaling of A_{CCF} .

The CCF area is measured within a 450 km s^{-1} -wide (13 \AA -wide) window centered on the peak after subtracting off a linear baseline that is fit to regions just outside this window on either side of it. The equivalent widths of the three Ca II lines are also measured directly from the spectrum, using three 350 km s^{-1} -wide (10 \AA -wide) windows centered on the three lines each flanked by a pair of windows of the same width for measurement of the local continuum level. The three measurements are combined into a weighted sum, ΣCa , following Eq. (3). Figure 9 shows a plot of A_{CCF} versus ΣCa for all 93 objects for which there is a reliable peak in the CCF (80 out of 99 objects in the main M31 target sample and all 13 in the control sample). A straight line through the origin is

fit to these data; the best-fit slope is the scale factor needed to convert A_{CCF} into the effective combined equivalent width (in Å units): $\Sigma\text{Ca}_{\text{CCF}} = 0.0915A_{\text{CCF}}$.⁷

The correction from effective equivalent width to reduced equivalent width requires knowledge of the V -band luminosity of the star relative to the horizontal branch. The RGG photometric dataset covers $UBRI$ only, so it is necessary to synthesize a V -band magnitude from these data. Stars display a tight relationship between $B - I$ and $V - I$ across a wide range of metallicities and ages: this is illustrated in Fig. 10 for Bergbusch & Vandenberg (2001) model stellar isochrones in the range $-2.3 \leq [\text{Fe}/\text{H}] \leq -0.3$ dex and $8 \leq t \leq 18$ Gyr. This relation and the extinction-corrected B and I magnitudes of a star are used to derive V_{synth} . A horizontal branch magnitude of $V_{\text{HB}} = 25.17$ is adopted from the Holland et al (1996) *HST* study of M31 halo stars in the G312 field; the KPNO data used in the RGG work are not deep enough to detect, let alone measure, the horizontal branch.

Figure 11 shows the combined equivalent width derived from the CCF, $\Sigma\text{Ca}_{\text{CCF}}$, as a function of the V luminosity relative to the horizontal branch for the 25 stars in the secure M31 sample with $v < -220$ km s⁻¹. The tilted dashed lines are loci of constant metallicity for the different calibration relations. The quantities $\Sigma\text{Ca}_{\text{CCF}}$ and V_{synth} are used to compute the reduced equivalent width, W' , via Eq. (4) for the 80 stars in the main M31 spectroscopic target sample for which there is a reliable measurement of the Ca II lines. The quantity W' is then used in Eqs. (5 and 6) to calculate the metallicities on the Zinn-West and Carretta-Gratton scales, $[\text{Fe}/\text{H}]_{\text{ZW}}$ and $[\text{Fe}/\text{H}]_{\text{CG97}}$, respectively. These metallicity estimates, along with the different measures of the Ca II line strength, A_{CCF} , $\Sigma\text{Ca}_{\text{CCF}}$, and W' , are listed in Table 3.

4.2.3. Measurement Errors

As explained in §4.2.2, the directly measured equivalent width ΣCa is likely to be a noisier statistic than the CCF area A_{CCF} , so that the scatter in Fig. 9 is probably dominated by the former. Nevertheless, we make the conservative assumption that *all* of the scatter in the plot is caused by measurement errors in A_{CCF} . On the other hand, the errors in A_{CCF} and ΣCa are undoubtedly correlated—a noise feature near a Ca II absorption line will cause excursions of the same sign (even if not exactly the same magnitude) in both quantities—and this causes the scatter in Fig. 9 to be smaller than the true noise. The rms scatter in A_{CCF} is 5.57, which corresponds to an rms error of $5.57 \times 0.0915 = 0.51$ Å in the effective combined equivalent width $\Sigma\text{Ca}_{\text{CCF}}$. The 1σ error in V_{synth} is conservatively assumed to be the quadrature sum of $B - I$ color error (RGG) and 0.1 mag, the

⁷The specific value of the slope is tied of course to the rather arbitrary units in which A_{CCF} is measured, which in turn depends on the widths of the object/template spectral bins (0.62Å) and velocity bins (10 km s⁻¹) used in the CCF computation. The A_{CCF} values displayed in Table 3 and Fig. 9 can be converted to units of Å km s⁻¹ by multiplying by the product of the bin widths, 6.2 Å km s⁻¹; naturally the slope would then have to be reduced by a corresponding factor to $0.0915/6.2 = 0.0148$.

latter to account for possible systematic errors in the model isochrones used for the interpolation.

Propagating the $\Sigma\text{Ca}_{\text{CCF}}$ and V_{synth} errors for a typical star through the various calibration relations yields a 1σ error of about 0.05 dex in the metallicity within the calibrated ranges of the ZW and CG97 scales. This is roughly consistent with the metallicity error estimates of Rutledge et al. (1997b), which must be somewhat fortuitous given the obvious oversimplifications (leading to over-/under-estimates) in our input parameter error analysis. The rms error of 0.05 dex should be treated as the accuracy with which the stars can be assigned relative ranks in metallicity. The ability to determine a “true” $[\text{Fe}/\text{H}]$ on either metallicity scale is probably uncertain by at least 0.2 dex as a result of systematic errors—e.g., departure of the $[\alpha/\text{Fe}]$ ratio from the assumed value of +0.3 dex. We therefore add in quadrature to the random error in $[\text{Fe}/\text{H}]$ a systematic error component of 0.2 dex.

An external check of the $[\text{Fe}/\text{H}]$ calibration is carried out using Keck/LRIS observations of RGB stars in two Galactic star clusters of known metallicity: M79 ($[\text{Fe}/\text{H}]_{\text{ZW}} = -1.68$ and $[\text{Fe}/\text{H}]_{\text{CG97}} = -1.37$ dex—Carretta & Gratton 1997) and NGC 6791 ($[\text{Fe}/\text{H}]_{\text{ZW}} = +0.19$ dex—Friel & Janes 1993). Figure 12 is a plot of ΣCa versus $V - V_{\text{HB}}$ for these stars. The stars in both clusters appear to follow the slope of the constant metallicity loci thereby confirming the validity of the 0.64 factor in the W' formula [Eq. (4)]. On average, the data for M79 giants agree with both ZW and CG97 calibration relations to within 0.05 dex or better. The metallicity of NGC 6791 is beyond the upper end of the range over which the ZW calibration relation is defined and the cubic formula diverges here: the value of $[\text{Fe}/\text{H}]_{\text{ZW}}$ derived from our NGC 6791 data is nearly 2 dex higher than its standard published value. Our empirical estimate of $[\text{Fe}/\text{H}]_{\text{CG97}}$ for NGC 6791 is 0.3 dex lower than its standard ZW value, although this comparison ignores any systematic offset between the CG97 and ZW scales. In summary, the spectroscopic metallicity estimates appear to be generally uncertain in the vicinity of solar values, particularly for the ZW and empirical “phot+spec” calibrations (§ 4.3).

There is an independent indication that the uncertainty in the spectroscopic $[\text{Fe}/\text{H}]$ estimates might be greatest at the high metallicity end. The scatter in the A_{CCF} versus ΣCa plot appears to be highest at the upper end (Fig. 9). This could be due to the fact that the highest-metallicity M31 giants are, on average, fainter and consequently have lower S/N spectra than their lower-metallicity counterparts (because of the drop in the tip of the RGB magnitude with increasing $[\text{Fe}/\text{H}]$; see § 5.2). It could also be due to anomalies (say in the absorption line shapes) of the four M31 giants with the strongest Ca II lines.

4.3. Comparing Photometric and Spectroscopic Estimates

In this section, we compare the above spectroscopic metallicity estimates to the photometric estimate on a star-by-star basis. The spectroscopic and photometric metallicity determination methods and their associated systematic errors are different from/independent of each other, so

that a comparison like this should help set rough upper limits on the “external” errors in our metallicity estimates. Moreover, this comparison helps shed some more light on the question of which stars in the sample are likely to be members of M31 and which ones are not.

Figure 13 shows $[\text{Fe}/\text{H}]_{\text{CG97}}$ versus $[\text{Fe}/\text{H}]_{\text{phot}}$ and $[\text{Fe}/\text{H}]_{\text{ZW}}$ versus $[\text{Fe}/\text{H}]_{\text{phot}}$ (upper and lower panels, respectively) for the 25 stars in the secure M31 sample with radial velocities $v < -220 \text{ km s}^{-1}$. In broad terms, there is a reasonably good correlation between spectroscopic and photometric $[\text{Fe}/\text{H}]$ estimates within the calibrated ranges of the measurement methods. A more detailed comparison shows that, within the calibrated range, the $[\text{Fe}/\text{H}]_{\text{CG97}}$ and $[\text{Fe}/\text{H}]_{\text{ZW}}$ estimates are about 0.2 and 0.5 dex (respectively) more metal-poor on average than the photometric estimate. If M31 halo giants happen to have solar abundance ratios, instead of the assumed $[\alpha/\text{Fe}] = +0.3$ dex enhancement level, this would bring the spectroscopic and photometric metallicity estimates into closer agreement (§ 5.5).

The rms difference between $[\text{Fe}/\text{H}]_{\text{CG97}}$ and $[\text{Fe}/\text{H}]_{\text{phot}}$ is 0.38 dex within the calibrated range and 0.76 dex outside the range, while the corresponding $[\text{Fe}/\text{H}]_{\text{ZW}}$ versus $[\text{Fe}/\text{H}]_{\text{phot}}$ rms differences are 0.55 and 3.52 dex, respectively. The divergence of $[\text{Fe}/\text{H}]_{\text{ZW}}$ for objects with strong Ca II lines is due to the extrapolation of the cubic formula; the relative metallicity ranking for objects beyond the calibrated range should be correct, but the actual values of $[\text{Fe}/\text{H}]_{\text{ZW}}$ are probably far from the true metallicities. There are other possible reasons for the rms being high outside the calibrated range: the four stars with the strongest Ca II lines may have atypical properties (§ 5.3), while the bluest star (lowest $[\text{Fe}/\text{H}]_{\text{phot}}$ value) may be a foreground Galactic dwarf star (see below).

It is tempting to think of the above rms differences as the quadrature sum of the errors in $[\text{Fe}/\text{H}]_{\text{phot}}$ and $[\text{Fe}/\text{H}]_{\text{CG97}}$ or $[\text{Fe}/\text{H}]_{\text{ZW}}$, but there are a couple of complicating factors. Firstly, any residual foreground contamination in the sample would cause the errors in $[\text{Fe}/\text{H}]$ to be overestimated. Secondly, the errors in the photometric and spectroscopic $[\text{Fe}/\text{H}]$ estimates are correlated in principle: the same B and I magnitudes from which $[\text{Fe}/\text{H}]_{\text{phot}}$ is determined are also used to compute V_{synth} , which is used to make a surface gravity correction to the Ca II line strength in the spectroscopic $[\text{Fe}/\text{H}]$ measurement scheme. If the correlation between photometric and spectroscopic $[\text{Fe}/\text{H}]$ errors is positive, the rms difference would tend to underestimate the errors, and vice versa if the correlation is negative. The observed lack of correlation between photometric and spectroscopic $[\text{Fe}/\text{H}]$ estimates for objects with $v > -220 \text{ km s}^{-1}$ (see below) indicates that any correlation between the errors, positive or negative, is probably quite small.

In contrast to the $v < -220 \text{ km s}^{-1}$ sample, there is no obvious overall correlation between $[\text{Fe}/\text{H}]_{\text{CG97}}$ or $[\text{Fe}/\text{H}]_{\text{ZW}}$ and $[\text{Fe}/\text{H}]_{\text{phot}}$ for objects with $v > -220 \text{ km s}^{-1}$ (Fig. 14). Instead, most lie in a band of near-constant line strength (which gets mapped to $[\text{Fe}/\text{H}]_{\text{CG97}} \sim [\text{Fe}/\text{H}]_{\text{ZW}} \sim -2$ dex) despite their wide range of $B - I$ colors. The lack of correlation is only to be expected for Milky Way dwarf stars: both the photometric and spectroscopic metallicity determination methods are based on the premise that the object being measured is a red giant at the distance of M31, so $[\text{Fe}/\text{H}]$ estimates for foreground objects are totally incorrect and in different ways for the two

methods. There could of course be a small fraction of M31 red giant stars hidden in Fig. 14; in fact, we *expect* about 11 such stars to be present. Firstly, the four bold circles—red subset of stars in the intermediate velocity range, $-220 < v < -160$ km s⁻¹—belong to the secure M31 red giant sample and they indeed lie relatively close to the $x = y$ line in both panels. Secondly, the IASG model plus Gaussian fit to the velocity distribution predicts that about 16% of the 46 stars in the main sample with $v > -160$ km s⁻¹, or about 7 stars, are M31 giants (§ 3.2). The horizontal band formed by the small circles in Fig. 14 inevitably crosses the $x = y$ diagonal line, but there are a handful of stars even outside this area of intersection for which the spectroscopic and photometric [Fe/H] estimates are in rough agreement and these stars are probably M31 red giants—e.g., the five or so stars mixed in with the bold circles and possibly the star in the lower left corner of the upper panel with $[\text{Fe}/\text{H}]_{\text{CG97}} \approx [\text{Fe}/\text{H}]_{\text{phot}} \approx -3$ dex.

Conversely, one or two stars in the velocity range $v < -220$ km s⁻¹ are expected to be Milky Way dwarf stars in the foreground of M31. Following the reasoning given in § 3.2, the most likely area of foreground contamination in this velocity range is at the blue end of the color distribution. The star with the bluest color ($B - I = 2.2$) and lowest $[\text{Fe}/\text{H}]_{\text{phot}}$ in Fig. 13, object ID t3.12 in Tables 1 and 3, is likely to be a star near the main sequence turnoff in the Galactic halo. The IASG model prediction for the velocity distribution of blue stars has a tail toward negative velocities, extending past the radial velocity of the star in question, $v = -306$ km s⁻¹ (Fig. 8). Moreover, neither $[\text{Fe}/\text{H}]_{\text{CG97}}$ nor $[\text{Fe}/\text{H}]_{\text{ZW}}$ is close to $[\text{Fe}/\text{H}]_{\text{phot}}$ for this star, the difference being nearly 1 dex; instead, the spectroscopic [Fe/H] estimates are within the horizontal band at ≈ -2 dex occupied by most Milky Way dwarfs in Fig. 14.

It is instructive to directly check the degree of correlation between the reduced Ca II line strength and the photometric metallicity estimate derived from the ($B - I$, I) CMD. For the 25 stars in the M31 secure sample with $v < -220$ km s⁻¹, an empirical linear relation of the form:

$$[\text{Fe}/\text{H}]_{\text{phot+spec}} = -2.13 + 0.25 W' \quad \text{dex} \quad (7)$$

produces the optimal mapping from W' to $[\text{Fe}/\text{H}]_{\text{phot}}$. The metallicity derived using this empirical calibration relation, hereafter referred to as $[\text{Fe}/\text{H}]_{\text{phot+spec}}$, is plotted versus $[\text{Fe}/\text{H}]_{\text{phot}}$ in Fig. 15. The rms scatter in this plot is 0.35 dex within the calibrated range and 0.61 dex outside it. In fact, a linear mapping results in a somewhat lower χ^2 value than a quadratic or cubic mapping of $W' \rightarrow [\text{Fe}/\text{H}]$. It should come as no surprise that the correlation between $[\text{Fe}/\text{H}]_{\text{phot+spec}}$ and $[\text{Fe}/\text{H}]_{\text{phot}}$ is tighter than the correlation between either $[\text{Fe}/\text{H}]_{\text{CG97}}$ or $[\text{Fe}/\text{H}]_{\text{ZW}}$ and $[\text{Fe}/\text{H}]_{\text{phot}}$. The empirical “phot+spec” calibration relation is designed to optimize this correlation, while the ZW and CG97 [Fe/H] estimates are based on calibration formulae that have been derived from *independent* data sets.

We emphasize that $[\text{Fe}/\text{H}]_{\text{phot+spec}}$ should *not* be treated as a true metallicity scale, or as an alternative to the CG97 or ZW scales; it is merely designed to highlight the agreement between photometric and spectroscopic [Fe/H] estimates. The constant metallicity lines for the empirical “phot+spec” calibration in the right panels of Figs. 11 and 12 are evenly spaced just as they

are for the linear CG97 relation (middle panels), but the former set of lines have a much wider spacing reflecting the smaller coefficient of the linear term in the calibration relation [Eq. (7)]. The “phot+spec” relation is clearly inaccurate at the high metallicity end: it underpredicts the metallicity of the slightly super-solar calibration cluster NGC 6791 by 0.8 dex (right panel of Fig. 12). This end of the empirical relation is largely constrained by the four stars with the highest spectroscopic metallicities and it is possible that their $[\text{Ca}/\text{Fe}]$ abundance ratios are abnormally high (§ 5.3). If these four stars were to be excluded from the analysis, the linear coefficient in Eq. (7) would nearly double and this would bring the empirical calibration relation more or less in line with the CG97 relation.

Figure 16 shows the difference between the photometric and spectroscopic $[\text{Fe}/\text{H}]$ estimates (CG97 and ZW) as a function of mean metallicity for the 29 stars comprising the secure M31 red giant sample. The mean metallicity, $\langle[\text{Fe}/\text{H}]\rangle$, is simply the average of $[\text{Fe}/\text{H}]_{\text{CG97}}$, $[\text{Fe}/\text{H}]_{\text{ZW}}$, and $[\text{Fe}/\text{H}]_{\text{phot}}$; this is not a particularly accurate measure of metallicity and is only used here as a common x -axis scale to facilitate comparisons between the two panels. For stars with $\langle[\text{Fe}/\text{H}]\rangle$ in the sub-solar range, the spectroscopic metallicity estimates are slightly lower on average than the photometric estimate, by 0.2 and 0.5 dex for the CG97 and ZW scales, respectively. For the four stars with solar or super-solar $\langle[\text{Fe}/\text{H}]\rangle$ values (§ 5.3), $[\text{Fe}/\text{H}]_{\text{CG97}}$ is 0.75 dex higher on average than $[\text{Fe}/\text{H}]_{\text{phot}}$, while the cubic ZW relation diverges at the high Ca II line strengths that characterize these stars.

5. Discussion

5.1. Observed Metallicity Distribution of M31’s Field Halo Stars

The secure sample of 29 M31 red giants is practically free of foreground contamination so it is used to investigate the metallicity distribution of M31’s stellar halo. We should emphasize that all of the discussion in this section is based on the *observed* $[\text{Fe}/\text{H}]$ distribution. Our sample selection efficiency is *not* uniform with metallicity; thus, the mean/median and rms estimates of the $[\text{Fe}/\text{H}]$ distribution of M31’s stellar halo are revised once the selection efficiency is properly accounted for (next section).

The observed $[\text{Fe}/\text{H}]$ distributions for the secure M31 sample are shown in the three upper panels of Fig. 17 for the ZW and CG97 spectroscopic calibrations and photometric estimate. All three distributions show signs of bimodality: note the two peaks centered at $[\text{Fe}/\text{H}]_{\text{phot}} = -1.0$ and -1.8 dex. This is roughly similar to the peaks at roughly -0.8 and -1.4 dex found by Durrell et al. (1999, 2001) in their wide-field photometric study. Each of the three $[\text{Fe}/\text{H}]$ distributions displays an overall spread of $\gtrsim 2$ dex. The sample mean and median for each of the $[\text{Fe}/\text{H}]$ calibrations are listed in Table 4 and are in the range -1.0 to -1.4 and -1.3 to -1.7 dex, respectively. Removal of the four red intermediate-velocity stars from the sample does not change these numbers appreciably.

While the three estimates of the $[\text{Fe}/\text{H}]$ distribution of M31 stellar halo are broadly similar, there are some differences in detail, especially near the extremes of the distributions. For example, there are four stars with particularly strong Ca II absorption lines that lie beyond the upper end of the calibrated range of the spectroscopic scales, but there is no corresponding high-metallicity tail in the $[\text{Fe}/\text{H}]_{\text{phot}}$ distribution. The $[\text{Fe}/\text{H}]_{\text{ZW}}$ estimates for these four stars are spuriously high and this causes the mean metallicity of the secure sample to be slightly higher on the ZW scale than on the CG97 and photometric scales. The upward extrapolation of cubic ZW relation is not to be trusted and it may be preferable to instead rely on the photometric and CG97 estimates for solar or slightly super-solar metallicity giants. It should be cautioned though that the agreement between the CG97 and photometric scales is far from perfect, especially at these high metallicities. The median $[\text{Fe}/\text{H}]$ is insensitive to outliers and therefore robust; it is lowest for the ZW scale and highest for the photometric scale.

The rms spread of the $[\text{Fe}/\text{H}]$ distributions is boosted by these outlying stars, most strongly in the case of the ZW calibration (Table 4). We argue in §5.3 that the four strong-lined stars are possibly members of the M31 disk, not its halo. Thus, these stars are excluded in order to obtain a conservative lower limit to the rms spread in $[\text{Fe}/\text{H}]$ in M31’s halo: 0.5–0.6 dex. This is substantially larger than the (internal and external) measurement uncertainties in $[\text{Fe}/\text{H}]$ (§§ 4.1.2, 4.2.3, and 4.3) and thus represents the intrinsic spread in metallicity among M31 halo stars.

5.2. Selection Efficiency Function: Bias Against Metal-Rich Giants

In this section, we quantify the bias against high-metallicity red giants that is introduced by the apparent magnitude cut ($I < 22$) imposed during the selection of spectroscopic targets. Such a bias occurs due to the decrease in the luminosity of the tip of the red giant branch with increasing metallicity for $[\text{Fe}/\text{H}] \gtrsim -1$ dex. Figure 18 is a plot of apparent I -band magnitude versus $[\text{Fe}/\text{H}]_{\text{phot}}$ for the 29 stars comprising the secure M31 sample. Also shown is the expected locus of the tip of M31’s RGB as a function of metallicity derived from theoretical isochrones computed by the Padova group (Bertelli et al. 1994; Girardi et al. 1996) and Bergbusch & Vandenberg (1992): solid and dashed lines, respectively. The model isochrones are shifted by an apparent distance modulus of $(I - M_I) = 24.57$, based on $D_{\text{M31}} = 783$ kpc and a typical reddening amount of $E(B - V) = 0.06$ which corresponds to $A_I = 0.1$ (§ 4.1.1). As expected, the upper envelope of the distribution of stars in Fig. 18 generally appears to follow the tip of the RGB locus. There is the occasional star located above one or both of the loci and this could be due to a variety of factors: photometric errors, error in the M31 distance modulus/depth effect, uncertainties in the models, and stellar evolutionary effects (e.g., presence of intermediate-age asymptotic giant branch stars).

While the number of stars per unit I magnitude bin in Fig. 18 increases with decreasing brightness over most of the displayed range, it is noticeable that the increase does *not* continue

monotonically all the way to the faint end of the range over which spectroscopic targets were selected, $I = 22$. This is in contrast to what might be expected for an RGB population that is simply truncated at a specific magnitude limit. The phenomenon is more clearly illustrated in Fig. 19 which shows the distribution of apparent I magnitudes for the secure sample of 29 M31 red giants (bold histogram). The dashed and dotted lines show two model RGB luminosity functions (LFs) for comparison, derived from the Padova isochrones (Bertelli et al. 1994; Girardi et al. 1996) and they both continue to rise to $I = 22$ irrespective of the details of $[\text{Fe}/\text{H}]$ weighting.⁸ The decrease in the relative completeness fraction of the secure sample toward the faint end is a result of two factors: assignment of lower priorities in the mask design process and lower rate of spectroscopic success for faint RGB stars compared to brighter counterparts. For example, 11 of the 19 low-S/N cases for which the radial velocity measurement fails correspond to objects with $I > 21.4$ with most clustered near the faint limit of $I = 22$ (see §2.4 and Fig. 6). These two sources of magnitude bias in the secure sample are difficult (if not impossible) to quantify from first principles; we instead make an empirical determination of the combined effect of both factors.

The relative completeness fraction as a function of apparent I magnitude is parameterized as a pair of exponentials:

$$\begin{aligned} C(I) &= 1 - 0.1 \exp [(I - I_{90})/\Delta_C] && (I < I_{90}) \\ &= 0.25 + 0.65 \exp [-(I - I_{90})/\Delta_C] && (I > I_{90}) \end{aligned} \quad (8)$$

where $I_{90} = 21.55$ is the 90% completeness limit, and $\Delta_C = 0.05$ is the e -folding range of the completeness function. These parameters have been chosen to optimize the match between the observed I -band LF of the secure M31 sample on the one hand and the product of $C(I)$ and the model RGB LF on the other (histogram vs. solid line in Fig. 19). The 50% completeness limit, $I_{50} = I_{90} + \Delta_C \ln(2.6) = 21.60$, is indicated in Fig. 18. The apparent 25% floor in $C(I)$ at the faint end could be the result of some masks having substantially better data quality than the rest (for some of the reasons listed in §2.3) so that their spectroscopic success rate is essentially perfect even for objects as faint as $I = 22$. The detailed form of $C(I)$ should not be taken too literally, however—the observed secure sample LF from which $C(I)$ is derived suffers from photometric errors and large Poisson errors, and there is some uncertainty in the model RGB LFs. Fortunately, the details of $C(I)$ are not too important for metallicity-bias correction either: in fact, the corrected mean/median $[\text{Fe}/\text{H}]$ values in Table 4 would, for the most part, be lowered by $\lesssim 0.1$ dex if $C(I)$ were ignored altogether (see below).

Theoretical stellar isochrone population functions are used to compute the mass fraction (as a function of $[\text{Fe}/\text{H}]$) contained within the apparent magnitude range $20 < I < 22$ over which the M31 spectroscopic targets are selected. As shown in Fig. 18, the tip of the RGB cuts progressively deeper

⁸Although the location of the RGB tip is dependent on metallicity, the shape of the composite LF is only weakly dependent on the assumed $[\text{Fe}/\text{H}]$ distribution of the RGB population. The two model LFs in Fig. 19 are based on Gaussian and top-hat $[\text{Fe}/\text{H}]$ distributions and yet the resulting LFs are very similar.

into the upper part of this range with increasing metallicity: $I_{\text{TRGB}} \lesssim 20.6$ for $[\text{Fe}/\text{H}] < -1$ dex but drops to $I_{\text{TRGB}} \sim 21.3$ for $[\text{Fe}/\text{H}] = 0$ dex. This causes the mass fraction to decrease with increasing metallicity for $[\text{Fe}/\text{H}] > -1$ dex. The steepness of the decrease is slightly accentuated by the increasing degree of incompleteness toward the faint end of the range, even though $C(I)$ itself is metallicity-independent. Figure 20 shows the resulting mass fraction or metallicity selection efficiency function for the secure M31 sample: the solid line represents a calculation based on the Padova group’s isochrones (Bertelli et al. 1994; Girardi et al. 1996) taking $C(I)$ into account—this is hereafter adopted for the metallicity-bias correction; the dashed and dotted lines represent calculations based on the Padova and Bergbusch & Vandenberg (1992) isochrones, respectively, in which $C(I)$ is ignored (set to unity). The selection efficiency curves are normalized at low $[\text{Fe}/\text{H}]$ as we are only interested in their shapes. The significant difference between the selection efficiency curves derived from the two sets of isochrones reflects one of the inherent sources of uncertainty in the metallicity-bias correction. Both sets of isochrones correspond to an age $t \approx 14$ Gyr with a mass function slope close to the Salpeter (1955) value of $x = +1.35$; it should be noted though that the metallicity-dependence of the selection efficiency is the same for all mass function slopes and all ages older than a few Gyr, even though the upper RGB mass fraction at any given metallicity depends strongly on these parameters.

To account for metallicity selection bias, every star is assigned a relative weight based on its $[\text{Fe}/\text{H}]_{\text{phot}}$ value, the weight being the reciprocal of the relative $[\text{Fe}/\text{H}]$ selection efficiency (solid line in Fig. 20). The weight is approximately unity for each low-metallicity star, but increases to 1.4, 2, and 5 for stars with $[\text{Fe}/\text{H}]_{\text{phot}} = -1, -0.5,$ and 0 dex, respectively. One of the four stars in the kinematically-coherent metal-rich group (object ID t1.17—§ 5.3) has the highest $[\text{Fe}/\text{H}]_{\text{phot}}$ value of all stars in the secure M31 sample, -0.24 dex. The weighted (i.e., corrected) $[\text{Fe}/\text{H}]$ histograms for the secure M31 sample are shown in the lower panels of Fig. 17. The histograms are normalized by the mean weight of the stars in the secure sample; thus the net area under each $[\text{Fe}/\text{H}]$ distribution is the same before and after correction and is equal to 29, the observed number of secure M31 red giants.

A comparison between the uncorrected and corrected $[\text{Fe}/\text{H}]_{\text{phot}}$ distributions shows that the high-metallicity end is systematically boosted in the latter. This is also true for the $[\text{Fe}/\text{H}]$ distributions on the ZW and CG97 scales but the effect is not nearly as systematic, as the weight is derived from $[\text{Fe}/\text{H}]_{\text{phot}}$ even for the spectroscopic $[\text{Fe}/\text{H}]$ histograms and the correlation between the spectroscopic and photometric metallicity estimates is not exactly one to one. The selection bias correction causes the mean and median values of all the $[\text{Fe}/\text{H}]$ distributions to increase slightly (the corrected values are listed in Table 4). The upward shift in the mean/median of the $[\text{Fe}/\text{H}]_{\text{phot}}$ distribution is a few tenths of a dex. Disregarding the very high (and almost certainly spurious) $[\text{Fe}/\text{H}]_{\text{ZW}}$ estimates for the four metal-rich stars in a coherent group, the shift in the spectroscopic $[\text{Fe}/\text{H}]$ distributions is somewhat smaller than for $[\text{Fe}/\text{H}]_{\text{phot}}$, about $+0.1$ dex.

It should be kept in mind that the type of selection bias discussed in this section is not unique to our study—the drop in I_{TRGB} with increasing $[\text{Fe}/\text{H}]$ makes the highest-metallicity giants

harder to detect and photometer than their low-metallicity counterparts in all photometric studies. Photometric studies of the M31 halo, especially ones based on *HST* images, often reach as deep as 5 mag into the RGB LF so the selection bias is not as severe as in our $I = 20 - 22$ spectroscopic sample which contains only the brightest RGB stars. Other tracers of the halo are affected too: for example, a high-metallicity globular cluster has a fainter integrated luminosity than a low-metallicity cluster of the same total mass and mass function slope as a result of the drop in I_{TRGB} , and this causes a relative underrepresentation of the former in any apparent-magnitude-limited sample.

5.3. Possible Disk Stars or Metal-Rich Debris?

Figure 21 shows a plot of metallicity (two spectroscopic estimates and photometric estimate) versus radial velocity for all 80 spectroscopic targets with reliable measurements. The objects in the range $v < -220 \text{ km s}^{-1}$ appear to cluster into three distinct groups: (a) 5 objects with the most negative velocities, $v \leq -460 \text{ km s}^{-1}$, mostly have low $[\text{Fe}/\text{H}]$; (b) 16 objects with $-340 < v < -220 \text{ km s}^{-1}$ exhibit a somewhat larger spread in $[\text{Fe}/\text{H}]$ over low to moderate values; and (c) 4 objects with $v \approx -340 \text{ km s}^{-1}$ have relatively high $[\text{Fe}/\text{H}]$ values. The lack of objects in the range $-460 < v < -360 \text{ km s}^{-1}$ appears to be a real feature of our sample; it is not caused by reduced detectability of the Ca II absorption line triplet in the vicinity of strong night sky emission lines (top panel of Fig. 1).

The last group of 4 stars—t1.17, t2.01, t1.06, and t1.04—lies close to M31’s systemic velocity in our minor axis field of study: thus, their kinematical properties are similar to what one might expect for red giants in M31’s disk. While these stars do not stand out in any particular way in the velocity histogram (Fig. 5), they are distinguished from the rest by their *combination* of high metallicity and common (close to systemic) velocity. In fact the 4 stars really stand out in terms of their spectroscopic $[\text{Fe}/\text{H}]$ estimates: they rank 3rd–6th, respectively, out of the full sample of 93 targets (80 in the main M31 target sample, 13 in the control sample) in terms of reduced Ca II equivalent width W' . The only 2 stars with stronger Ca II lines, t5.13 and t3.28, have radial velocities of $v = +239$ and -141 km s^{-1} , respectively, and this makes it likely that both are foreground Milky Way dwarf stars. This hypothesis is strengthened by the observation that the difference between $[\text{Fe}/\text{H}]_{\text{CG97}}$ and $[\text{Fe}/\text{H}]_{\text{phot}}$ for these stars is 6.2 and 1.8 dex, respectively (upper panel of Fig. 14). By contrast, the 4 stars ranked 3rd–6th lie closer to the $[\text{Fe}/\text{H}]_{\text{CG97}} = [\text{Fe}/\text{H}]_{\text{phot}}$ line in the upper panel of Fig. 13, as might be expected for red giants at the distance of M31 (the possible implications of their $\sim +0.8$ dex offset are discussed below). The $[\text{Fe}/\text{H}]_{\text{ZW}}$ estimates for the 4 stars are significantly greater than $[\text{Fe}/\text{H}]_{\text{phot}}$ but the difference appears to be a systematic function of metallicity (lower panel of Fig. 16) which suggests that this is due to the divergence of the cubic ZW relation beyond the directly-calibrated range. The spuriously-high $[\text{Fe}/\text{H}]_{\text{ZW}}$ estimates for these stars are to be disregarded whether or not the stars turn out to be members of the M31 halo.

In light of the possibility, albeit small (see below), that this kinematically-coherent group of 4 metal-rich stars belongs to M31’s disk rather than its halo, the mean, median, and rms of the halo $[\text{Fe}/\text{H}]$ distribution are recomputed with these stars excluded from the secure M31 sample (Table 4). The 4 stars are at or near the high end of the observed $[\text{Fe}/\text{H}]$ distribution, so their exclusion results in a 0.2 – 0.3 dex drop in the mean/median $[\text{Fe}/\text{H}]$ values. The mean (median) $[\text{Fe}/\text{H}]_{\text{CG97}}$ and $[\text{Fe}/\text{H}]_{\text{phot}}$ values for just the kinematically-coherent group of 4 stars are also listed in Table 4: +0.11 (0.00) and -0.64 (-0.62) dex, respectively.

The External Galaxy Model (Hodder 1995), an adaptation of the Bahcall & Soneira (1984) Galactic star count model to an external spiral galaxy, predicts that the M31 disk contamination fraction in our $R = 19$ kpc minor axis spectroscopic field should be as low as 0.01% (RGG). If the kinematically-coherent group of 4 metal-rich are indeed members of the M31 disk, they would represent a $> 10\%$ disk contamination fraction (4 out of 29), three orders of magnitude higher than expected based on extrapolation of M31’s inner disk brightness profile. The M31 disk is highly inclined with an apparent 4:1 aspect ratio ($1/\cos(i) = 1/\cos(77^\circ) \gtrsim 4$); thus, the projected distance of our field from the galaxy center, $R = 19$ kpc, corresponds to a radial distance of over 80 kpc in the plane of the disk, and this would be anomalously large for a spiral galaxy disk. A favorable warp in the disk could cause it to intersect the line of sight to our spectroscopic field without it needing to be this large. As a matter of fact, old photographic plates, modern CCD mosaic images, and H I data all point to the presence of substantial (major and minor axis) warps in M31’s stellar and gaseous disks (Newton & (Emerson 1977; Innanen, Harris, & Webbink 1983; Brinks & Shane 1984; Guhathakurta, Choi, & Reitzel 2000). It is unclear from these data, however, whether the M31 disk warp favors the detection of disk stars in our particular SE minor-axis field or works against it. Sarajedini & Van Duyne (2001) claim to have detected an M31 thick disk population with $\langle [Fe/H] \rangle \sim -0.2$ dex and it is possible that our group of 4 metal-rich kinematically-coherent stars belongs to this population. The properties of M31’s thick disk are not well characterized at the moment, however, so one cannot make a reliable estimate of the probability of detecting 4 thick disk stars in our field of study.

The Ibata et al. (2001) large-scale study of the M31 halo may be useful for gaining insight into the nature of this kinematically-coherent group of 4 metal-rich giants found in our spectroscopic study. In addition to the giant streamer that Ibata et al. draw attention to, there is a hint of a much smaller “feature” (possibly a minor debris trail of some sort) at the location of our spectroscopic field: $\sim 1.4^\circ$ from the galaxy’s center on the minor axis (see Fig. 1 of their paper). Thus, these 4 stars may have nothing to do with M31’s disk after all, and may instead represent a coherent piece of metal-rich debris from a past accretion event in the M31 halo.

Figure 22 shows the sky-positions of all spectroscopic targets grouped by radial velocity. Figure 23 shows the sky-positions of only the 29 secure M31 giants grouped by spectroscopic $[\text{Fe}/\text{H}]$ estimate. There is no obvious correlation in these plots between radial velocity or $[\text{Fe}/\text{H}]$ and a star’s position on the sky. The 4 kinematically-coherent metal-rich stars appear to lie in a straight line, but the small number of stars and the odd shape of the “footprint” of the spectroscopic targets

make this a tantalizing suggestion at best, with little or no statistical significance.

The average $[\text{Fe}/\text{H}]_{\text{CG97}}$ value for this group of 4 stars is 0.7–0.8 dex higher than their average $[\text{Fe}/\text{H}]_{\text{phot}}$ value (Fig. 13 and Table 4). It is possible that the 4 stars have distinctly higher $[\text{Ca}/\text{Fe}]$ ratios than the other secure M31 giants in the sample, perhaps anomalously high ratios: they truly stand out in terms of their Ca II line strengths but not in terms of their $[\text{Fe}/\text{H}]_{\text{phot}}$ values. Their $[\text{Fe}/\text{H}]_{\text{CG97}}$ versus $[\text{Fe}/\text{H}]_{\text{phot}}$ discrepancy is unlikely to be a result of extrapolation error in the CG97 relation beyond the upper end of the calibrated range [Eq. (6)]. Our empirical check using spectra of red giants in NGC 6791, a cluster of known metallicity ($[\text{Fe}/\text{H}]_{\text{ZW}} = +0.19$ dex), shows that if anything the CG97 relation *underpredicts* the metallicity of this cluster by 0.3 dex (Fig. 12). Another manifestation of this possible $[\text{Ca}/\text{Fe}]$ anomaly in these 4 stars (relative to NGC 6791 giants) can be found in the third panel of Fig. 12. The empirical “phot+spec” calibration relation is designed to achieve equality between spectroscopic and photometric $[\text{Fe}/\text{H}]$ estimates for the 4 metal-rich stars, but in doing so it underpredicts the metallicity of NGC 6791 by 0.8 dex (§ 4.3).

It may be impossible to tell (certainly from the data at hand, and perhaps in general) whether this kinematically-coherent group of 4 metal-rich giants has an “internal” origin—i.e., M31’s warped and/or disrupted disk—or an “external” one—i.e., one of the satellites currently undergoing tidal disruption (M32 or NGC 205) or a recently-accreted satellite galaxy that has been completely disrupted. In any case, a growing body of evidence has accumulated over the years showing that galaxy interactions are probably quite common in the M31 subgroup (Byrd 1979; Innanen et al. 1983; Ibata et al. 2001; Choi, Guhathakurta, & Johnston 2002).

5.4. Comparison to Photometric Studies: Is M31’s Halo Metal-Rich?

Previous photometric studies of the M31 halo—wide-field ground-based studies by Durrell, Pritchett, & Harris (1994), RGG, and Durrell et al. (1999, 2001), complemented by deeper *HST*/WFPC2 studies of smaller fields by Rich et al. (1996a,b, 2002) and Holland et al. (1996)—all yield mean $[\text{Fe}/\text{H}]$ values for the M31 halo that are systematically (if slightly) *higher* than the findings of our present spectroscopic study. In fact, the claim is made in some of these photometric studies that field halo stars in M31 have a significantly higher average metallicity than its globular cluster system, with a mean $[\text{Fe}/\text{H}]$ comparable to or in excess of the Galactic globular cluster 47 Tuc (−0.7 dex). This is very different from the case of the Milky Way where the field halo population has a slightly lower mean metallicity than its globular clusters (Fig. 24).

These results must be treated with caution though. The various M31 halo samples discussed above are drawn from many different parts of the galaxy so any intercomparison may be affected by the possible presence of large-scale gradients or metallicity substructure (§ 5.6). Moreover, even the photometric metallicity determination methods are not the same across the various studies (use of different colors, RGB fiducials vs. theoretical isochrones, different metallicity scales, etc.); unlike our present study, these earlier studies did not have the benefit of independent spectroscopic

determination of $[\text{Fe}/\text{H}]$. Finally, sample selection criteria and contamination levels are quite varied across the samples. While the inner halo fields are expected to contain a smaller fraction of foreground Milky Way dwarf contaminants than the outer halo fields, they tend to contain a greater fraction of M31 disk star contamination. The Holland et al. and Rich et al. *HST* studies of the G302, G312, and G1 fields made no correction for sample contamination in their photometric metallicity estimates. While statistical subtraction of foreground and background contaminants was attempted in the ground-based studies, these attempts were only partly successful at removing contaminants. The matching of comparison field data to the main data set is hardly ever perfect: differences in seeing, depth, crowding, Galactic latitude and longitude, etc. invariably limit the fidelity of the statistically-subtracted sample. The upshot of this is that any conclusions about the M31 halo metallicity or structure drawn from the above photometric studies are bound to be somewhat uncertain.

The spectroscopically-selected secure sample of M31 halo giants presented in this study is probably the cleanest sample of bright RGB stars in the M31 outer halo to date, but it suffers from severe incompleteness at the high-metallicity end of the distribution (§ 5.2). While attempts have been made to correct for this metallicity bias, our detection efficiency for near-solar-metallicity giants is simply too low for us to be able to constrain the high end of the $[\text{Fe}/\text{H}]$ distribution. Some metal-rich stars have in fact been detected in our survey, but not a single one with $[\text{Fe}/\text{H}] \gtrsim 0$ dex. The observed raw (i.e., uncorrected) $[\text{Fe}/\text{H}]$ distribution for the secure M31 sample spans more than 2 dex, and the bias-corrected distribution appears to cut off quite sharply just shy of solar $[\text{Fe}/\text{H}]$ where the selection function of our spectroscopic survey also drops off [see panel (f) of Fig. 17 for example]. Thus, it is entirely feasible that our spectroscopic survey is missing giants of near-solar $[\text{Fe}/\text{H}]$ and that the M31 halo is just as metal-rich as the photometric studies indicate. In other words, the apparent discrepancy between the mean $[\text{Fe}/\text{H}]$ found in our spectroscopic study and the generally higher values found in earlier photometric studies may simply be an artifact of selection effects in our study.

The discrepancy cannot be attributed to a systematic difference between spectroscopic and photometric $[\text{Fe}/\text{H}]$ measurement methods. As discussed in § 4.3 and illustrated in Fig. 13, a star-by-star comparison reveals a reasonably good agreement between these two $[\text{Fe}/\text{H}]$ estimates. Put differently, even the mean *photometric* $[\text{Fe}/\text{H}]$ estimate for our spectroscopically-confirmed sample of secure M31 halo giants is lower than the mean value found in other photometric surveys. Thus, the origin of the difference must lie in the red giant samples themselves.

A few other possible reasons for the discrepancy can be ruled out as well. Metallicity substructure in the M31 halo cannot be the culprit: the RGG and Durrell et al. (1999, 2001) studies were carried out in the same $R = 19$ kpc minor axis field as our spectroscopic study and yet these studies find a slightly higher mean $[\text{Fe}/\text{H}]$ value. Sampling effects and pre-selection criteria for the spectroscopic targets cannot be blamed either: the RGG study and this spectroscopic study use the same *UBRI*-based photometric criteria to isolate red giant candidates; in fact, the shape of the $B - I$ color distribution of our 99 spectroscopic targets is identical to that of the parent sample

of 284 red giant candidates in the RGG study (*UBRI*- and morphology-selected objects in the $20 < I < 22$ range).

As part of a large, ongoing spectroscopic survey of the M31 halo, we have collected similar Keck/LRIS spectra for about 40–75 RGB candidates per field in each of the G1, G302, and G312 fields, the same fields that were targeted in earlier *HST*/WFPC2 photometric studies (Holland et al. 1996; Rich et al. 1996a,b). Analysis of these additional LRIS spectra is in progress (Guhathakurta 2002; Guhathakurta et al. 2002) and this should ultimately shed some light on the origin of the apparent [Fe/H] discrepancy. These spectroscopic data will provide a measure of the foreground Galactic dwarf/M31 disk giant contamination fraction in the *HST* photometric samples. Moreover, the greater than two-fold increase in the overall spectroscopic sample size in the M31 halo should improve the statistics on any rare population of high-[Fe/H] giants, which are of course made even more scarce by the metallicity bias in our selection function.

5.5. Comparison to Models and Other Halo Tracers

Simple chemical enrichment models are a useful guide to help interpret the observed metallicity distribution in the secure sample of M31 stars. A steady-gas-loss model (Da Costa et al. 2000; Hartwick 1976) is one where the instantaneous recycling approximation is made and where the gas loss is assumed to be proportional to the rate of star formation. In such a model, the metallicity distribution may be written as:

$$f(z) = (1/y)\exp[-(z - z_0)/y] \quad z \geq z_0 \quad (9)$$

where z_0 is the initial abundance and y is the yield. The yield and the mean abundance are related via: $y = \langle z \rangle - z_0$. The two free parameters for this model are $\langle z \rangle$ (or equivalently $\langle [\text{Fe}/\text{H}] \rangle$) and z_0 (or $[\text{Fe}/\text{H}]_0$).

The model which best fits the uncorrected [Fe/H] distributions has $[\text{Fe}/\text{H}]_0 = -10.0$ dex and $\langle [\text{Fe}/\text{H}] \rangle = -1.5$ dex. This model is plotted as a thin solid line over the metallicity distributions in each panel of Figs. 17 and 24 and as a bold solid line in panel (b) of the latter figure. The dashed and dotted lines in panel (b) of Fig. 24 are models with $\langle [\text{Fe}/\text{H}] \rangle = -2.0$ and -0.5 dex, respectively, with $[\text{Fe}/\text{H}]_0 = -10.0$ dex in both cases. The best fit model does a reasonable job of matching the overall metallicity distribution (see Fig. 17 and 24). If the hint of bimodality seen in the observed [Fe/H] distributions is confirmed with larger samples of stars, a single model will clearly not fit the data, but a two-component model might. Moreover, a great deal of pre-enrichment does not appear to be needed to explain the [Fe/H] distribution of the secure sample of M31 halo stars. The details of this “toy” chemical evolution model are not to be taken too literally: there are many simplifying assumptions on which such models are founded and the real set of physical conditions in place during the formation of the M31 halo are likely to have been considerably more complex. Moreover, the match between the model and observed [Fe/H] distributions in no way guarantees the uniqueness of this particular theoretical interpretation. We merely use the models as a very

rough guide to understanding the chemical enrichment history of the M31 halo, and as a point of reference for intercomparison of the $[\text{Fe}/\text{H}]$ distributions observed for the different M31 and Milky Way halo tracer populations.

The metallicity distribution of the secure M31 field halo giant sample is compared to other halo tracers in the Local Group (Fig. 24). The corrected distribution of $[\text{Fe}/\text{H}]_{\text{CG97}}$ values is plotted in panel (a), and the moments of this distribution appear in Table 4. It should be noted that different studies compute metallicity differently and the reader is referred to each reference for the details of each metallicity calculation. The data are scaled to match the overall number of objects in the secure M31 halo sample, 29, in order to facilitate comparison between the various samples.

The metallicity distribution of M31’s globular cluster system is presented in panel (c) of Fig. 24. The distribution is quite similar to that of the M31 field stars. Both have a spread of about 2 dex and a mean value around -1.2 dex (Barmby et al. 2000). The Milky Way globular clusters have a slightly lower mean metallicity, -1.4 dex (Harris 1996) and a more strongly bimodal distribution [panel (d)]. Carney et al. (1990) find a mean metallicity of $[\text{Fe}/\text{H}] = -1.72$ dex for field halo stars in the Milky Way and a metallicity probability distribution function (Laird et al. 1988) which has a spread of 2 dex and a lower mean than M31’s stellar halo [panel (e)].

Panel (f) of Fig. 24 shows the metallicity distribution of the Local Group dwarf satellite galaxies from the compilation of Grebel (1999, 2000). The histogram represents a direct sum over all satellite galaxies, with each galaxy getting the same weight. Alternatively, each satellite galaxy can be represented by a Gaussian whose mean/width is equal to the satellite’s measured mean/spread in $[\text{Fe}/\text{H}]$. Each Gaussian is weighted by the luminosity of the satellite it represents, and the individual Gaussians are then combined. The bold solid curve is the luminosity-weighted sum over all satellites, while the dashed curve is the sum over all except the Large Magellanic Cloud and M32. The direct sum and restricted luminosity-weighted sum are a good match to the observed $[\text{Fe}/\text{H}]$ distribution of M31 field halo giants, while luminosity-weighted sum over the full sample is dominated by a few luminous systems with relatively high metallicity (the Magellanic Clouds, M32, and NGC 205) and is a poor match. It should be noted that while the halos of M31 and the Milky Way may have been assembled from dwarf satellites, the properties of the surviving satellites seen today could be different from the properties of the satellites that were accreted to form these halos. Thus, one should not read too literally into the match/mismatch between the observed M31 halo $[\text{Fe}/\text{H}]$ distribution and that of the present-day satellites.

5.6. Implications

The field red giant population of the M31 halo is more metal-rich on average than that of the Milky Way. This implies that M31 underwent a larger amount of enrichment before the halo was assembled than did the Milky Way. In addition, M31 displays a slightly larger spread of metallicities. The large spread in $[\text{Fe}/\text{H}]$ observed in M31 tends to support the accretion model for

halo formation. *At face value*, a comparison of *HST* studies of M31’s inner halo to our spectroscopic study of its outer halo suggests that the mean metallicity decreases radially outwards. If such a radial gradient is truly present (see §5.4 caveats below), it would be consistent with the prediction of the monolithic collapse model.

While these implications appear to be inconsistent, the accretion models are currently too simplistic. A radial gradient could result even in the context of the accretion scenario, as the more massive satellites tend to have higher metallicities, and these are unlikely to be completely disrupted until they stray close to the center of the parent galaxy. By contrast, the less massive, lower-metallicity satellites will be completely disrupted before dynamical friction has had a chance to cause them sink too far into the parent galaxy potential.

One complication in comparing the observed metallicity distribution of M31 to other halo tracers is the underlying assumption that M31 giants have an enhancement in their alpha elements similar to that of the oldest Galactic globular clusters, $[\alpha/\text{Fe}] = +0.3$ dex. If the M31 halo is instead younger with solar element ratios, $[\alpha/\text{Fe}] = 0$ dex, as is the case for the young Milky Way globular clusters Pal 12 and Ruprecht 106 (Brown, Wallerstein, & Zucker 1997), then the spectroscopic metallicity estimates would have to be revised upwards by 0.3 dex. The photometric estimates would also be revised, but the change would not be nearly as large as +0.3 dex.⁹

6. Summary

The main points of this paper may be summarized as follows:

- A combination of imaging and spectroscopic data are used to examine the structure, metallicity, and dynamics of M31’s stellar halo. Deep Kitt Peak 4-m *UBRI* CCD images of a 19 kpc minor axis field in M31 are used to screen a sample of candidate field halo red giants using photometric and morphological criteria; a subset consisting of 99 such candidates, with brightnesses in the range $20 < I < 22$, form the target sample for the spectroscopic study.
- Multi-slit spectroscopy with the Keck II 10-m telescope and the Low Resolution Imaging Spectrograph of the Ca II near-infrared triplet is used to make secure identification of M31

⁹One way to understand this is to consider a star of a given $B - I$ color and a theoretical isochrone that passes through the star’s location in the CMD. If alpha elements were the *only* ones doing the line blanketing, changing $[\alpha/\text{Fe}]$ from +0.3 to 0 dex could be compensated by an equal and opposite change in $[\text{Fe}/\text{H}]$ (i.e., a 0.3 dex increase) to keep the color of the isochrone fixed. This would mean that the $[\text{Fe}/\text{H}]_{\text{phot}}$ estimate for the star would increase by this amount. If, on the other hand, the line blanketing from alpha elements were a negligible fraction of the overall amount of line blanketing, the change in $[\alpha/\text{Fe}]$ would not affect the color of the isochrone at all, and the $[\text{Fe}/\text{H}]_{\text{phot}}$ estimate for the star would stay unchanged. The real situation is somewhere between these two extreme examples, perhaps closer to the latter, which implies that the boost in $[\text{Fe}/\text{H}]_{\text{phot}}$ due to the change in $[\alpha/\text{Fe}]$ would be significantly less than +0.3 dex.

halo red giant branch stars by discriminating them from foreground Galactic dwarf stars, M31 disk red giants, and background field galaxies. Spectra of 13 additional bright objects ($I < 20$), foreground Milky Way stars along the line of sight to M31, have also been obtained and these serve as a control sample.

- The distribution of radial velocities of the main M31 spectroscopic target sample is well fit by an equal mix of foreground dwarfs (drawn from a standard Galactic model, with a peak close to $v \approx 0 \text{ km s}^{-1}$) and giants in M31’s halo represented by a Gaussian of width $\sigma_v^{\text{M31}} \sim 150 \text{ km s}^{-1}$ centered on its systemic velocity of $v_{\text{sys}}^{\text{M31}} \approx -300 \text{ km s}^{-1}$. A secure, largely uncontaminated sample of 29 M31 halo red giants is identified primarily on the basis of their large negative radial velocities, with limited use of broadband color information (in the context of a Galactic model) to reject foreground dwarf star contaminants at intermediate velocities.
- Metallicity measurements are made on a star-by-star basis using two independent methods: the strength of the Ca II absorption line triplet (calibrated via the Zinn-West or Carretta-Gratton relations for Galactic globular clusters) and the location of the star in the $B - I$ vs. I color-magnitude diagram relative to model red giant fiducials.
- The photometric and spectroscopic $[\text{Fe}/\text{H}]$ estimates are in reasonable agreement with each other for the secure M31 giants, especially those with metallicities within the calibrated range of the $[\text{Fe}/\text{H}]$ determination methods; the extrapolation of the cubic Zinn-West relation beyond the upper end of the calibrated range predicts substantially higher metallicities than the other $[\text{Fe}/\text{H}]$ estimates.
- The median metallicity of M31 halo red giants is in the range, $\langle [\text{Fe}/\text{H}] \rangle = -1.8$ to -1.1 dex, for various sample selection criteria and metallicity measurement methods. It should be cautioned, however, that our survey is very inefficient at finding M31 giants of solar/super-solar metallicity; in fact, none are detected with $[\text{Fe}/\text{H}]_{\text{phot}} \gtrsim 0$ dex. Thus, even though the quoted median values are corrected for selection bias against high-metallicity stars, they may be substantially lower than the true median metallicity of M31’s halo. The mean $[\text{Fe}/\text{H}]_{\text{ZW}}$ values scatter over a somewhat larger range than the corresponding median values due to a few stars with very high spectroscopic metallicities (see below) for which the extrapolation of the cubic Zinn-West relation diverges. In all cases, the observed M31 halo $[\text{Fe}/\text{H}]$ distribution has an rms spread of at least 0.6 dex, comparable to that of Milky Way field halo giants, M31 globular clusters, Galactic globular clusters, and Local Group dwarf satellite galaxies, and spans the full 2 dex range over which the metallicity measurement methods are calibrated, $-2 \lesssim [\text{Fe}/\text{H}] \lesssim 0$ dex.
- Photometrically-determined $[\text{Fe}/\text{H}]$ values from *Hubble Space Telescope* studies of the inner halo of M31, 7 and 11 kpc from the center on the minor axis, and from ground-based studies of the outer halo, the same $R = 19$ kpc minor axis field targeted in this spectroscopic study, yield a systematically higher mean metallicity (by up to 1 dex) than our study and a comparably

large spread of about 2 dex. As noted above, however, the mean $[\text{Fe}/\text{H}]$ of M31 halo giants may be severely underestimated in our spectroscopic survey because it is virtually incapable of detecting stars with solar or greater metallicity. Moreover, the previous photometric studies use different sample selection criteria than this study: in particular, their lack of spectroscopic data leaves open the possibility that the samples are contaminated by M31 disk giants and/or foreground Galactic dwarf stars. These factors make it difficult to compare the average $[\text{Fe}/\text{H}]$ values measured in different parts of M31’s halo.

- Within the secure sample of M31 red giants, there are four stars with red $B - I$ colors and exceptionally strong Ca II absorption lines indicating solar or super-solar metallicities. These stars lie within a relatively narrow velocity range at $\approx -340 \text{ km s}^{-1}$. This combination of high metallicity and common velocity close to M31’s systemic velocity is what might be expected for M31 disk giants in this minor-axis field. More likely, these stars represent metal-rich debris from a past accretion event.

Acknowledgments

We would like to acknowledge the support and help of several people who made this project possible: Linda Pittroff and Johnny Warren for reduction of cluster red giant calibration data, Drew Phillips for assistance with LRIS multislit mask design, mask alignment, and calibration procedures, Jeff Lewis, Bill Mason and Dave Cowley for mask fabrication, Dan Kelson for help with the Expecto spectral data reduction software, Eva Grebel for providing data on Local Group dwarf satellites, and Tom Bida, Randy Campbell and the rest of the Keck observatory staff for their expert guidance during the observing runs. We would also like to thank Mike Bolte, Phil Choi, Andy Gould, Bob Kraft, Ruth Peterson and Linda Schroeder for valuable suggestions and fruitful discussions, and the anonymous referee for a careful reading of the manuscript and detailed report which has led to key improvements in the paper. DBR is grateful to Mike Rich for his support during the final stages of the project. DBR and PG were funded in part by a CalSpace grant and by NASA grants NAG 5-3232 (Long Term Space Astrophysics) and NAG 5-8348 (Astrophysics Data Program).

REFERENCES

- Anderson, C. M. 1974, *ApJ*, 190, 585
- Armandroff, T. E., & Da Costa, G. S. 1991, *AJ*, 101, 1329
- Armandroff, T. E., Da Costa, G. S., & Zinn, R. 1992, *AJ*, 104, 164
- Armandroff, T. E., & Zinn, R. 1988, *AJ*, 96, 92
- Bahcall, J. N., & Soneira, R. M. 1984, *ApJS*, 55, 67
- Barmby, P., Huchra, J. P., Brodie, J. P., Forbes, D. A., Schroder, L. L., & Grillmair, C. J. 2000, *AJ*, 119, 727
- Bergbusch, P. A., & Vandenberg, D. A. 1992, *ApJ*, 81, 163
- Bergbusch, P. A., & Vandenberg, D. A. 2001, *ApJ*, 556, 322
- Bertelli, G., Bressan, A., Chiosi, C., Fagotto, F., & Nasi, E. 1994, *A&AS*, 106, 275
- Brinks, E., & Shane, W. W. 1984, *A&AS*, 55, 179
- Brown, J. A., Wallerstein, G., & Zucker, D. 1997, *AJ*, 114, 180
- Byrd, G. G. 1979, *ApJ*, 231, 32
- Bullock, J. S., Kravtsov, A. V., & Weinberg, D. H. 2001, *ApJ*, 548, 33
- Cardelli, J. A., Clayton, G. C., & Mathis, J. S. 1989, *ApJ*, 345, 245
- Carney, B. W., Aguilar, L., Latham, D. W., & Laird, J. B. 1990, *AJ*, 99, 201
- Carretta, E., & Gratton, R. G. 1997, *A&AS*, 121, 95 (CG97)
- Choi, P. I., Guhathakurta, P., & Johnston, K. V. 2002, *AJ*, in press (astro-ph/0111465)
- Da Costa, G. S., & Armandroff, T. E. 1995, *AJ*, 109, 2533
- Da Costa, G. S., Armandroff, T. E., Caldwell, N., & Seitzer, P. 2000, *AJ*, 119, 705
- Da Costa, G. S., Armandroff, T. E., & Norris, J. E. 1992, *AJ*, 104, 154
- Da Costa, G. S., & Seitzer, P. 1989, *AJ*, 97, 405
- de Vaucouleurs, G., de Vaucouleurs, A., Corwin Jr., H. G., Buta, R. J., Fouque, P., & Paturel, G. 1991, *The Third Reference Catalogue of Bright Galaxies (RC3)*, Springer-Verlag, New York
- Diaz, A. I., Terlevich, E., & Terlevich, R. 1989, *MNRAS*, 239, 325

- Durrell, P. R., Harris, W. E., & Pritchett, C. J. 1994, *AJ*, 108, 2114
- Durrell, P. R., Harris, W. E., & Pritchett, C. J. 2001, *AJ*, 121, 2557
- Durrell, P. R., Harris, W. E., Pritchett, C. J., & Davidge, T. 1999, *BAAS*, 195, 0404D
- Eggen, O. J., Lynden-Bell, D., & Sandage, A. R. 1962, *ApJ*, 136, 748
- Evans, N. W., & Wilkinson, M. I. 2000, *MNRAS*, 316, 929
- Evans, N. W., Wilkinson, M. I., Guhathakurta, P., Grebel, E. K., & Vogt, S. S. 2000, *ApJ*, 540, L9
- Friel, E. D., & Janes, K. A. 1993, *Å*, 267, 75
- Geisler, D., Piatti, A. E., Clariá, J., & Minniti, D. 1995, *AJ*, 109, 605
- Girardi, L., Bressan, A., Bertelli, G., & Chiosi, C. 2000, *A&AS*, 141, 371
- Girardi, L., Bressan, A., Chiosi, C., Bertelli, G., & Nasi, E. 1996, *A&AS*, 117, 113
- Gould, A., Guhathakurta, P., Richstone, D., & Flynn, C. 1992, *ApJ*, 388, 345
- Grebel, E. K. 1999, in “The Stellar Content of the Local Group”, eds. P. Whitelock & R. Cannon (IAU Symp. 192; San Francisco: ASP), 17
- Grebel, E. K. 2000, in “Star Formation from the Small to the Large Scale”, eds. F. Favata, A. A. Kaas, & A. Wilson (ESA SP-445; Noordwijk: ESA), 87
- Guhathakurta, P. 2002, in “The Shapes of Galaxies and their Halos”, ed. P. Natarajan (World Scientific), in press
- Guhathakurta, P., Choi, P. I., & Reitzel, D. B. 2000, *BAAS*, 197, 37.02
- Guhathakurta, P., & Reitzel, D. B. 1998, in *Galactic Halos*, ed. D. Zaritsky (ASP Conf. Series, No. 136), 22
- Guhathakurta, P., Reitzel, D. B., & Grebel, E. K. 2000, in “Discoveries and Research Prospects from 8- to 10-Meter-Class Telescopes”, ed. J. Bergeron, *Proc. SPIE*, 4005, 168
- Guhathakurta, P., Reitzel, D. B., Pittroff, L. C., & Phillips, A. C. 2002, *AJ*, in preparation
- Harris, W. H. 1996, *AJ*, 112, 1487
- Hartwick, F. D. A. 1976, *ApJ*, 209, 418
- Helmi, A., & White, S. D. M. 1999, *MNRAS*, 307, 495
- Helmi, A., & de Zeeuw, T. 2000, *MNRAS*, 319, 657
- Hodder, P. J. C. 1995, Ph.D. thesis, University of British Columbia

- Holland, S. 1998, *AJ*, 115, 1916
- Holland, S., Fahlman, G. G., & Richer, H. B. 1996, *AJ*, 112, 1035
- Horne, K. 1986, *PASP*, 98, 609
- Huchra, J. P., Brodie, J. P., & Kent, S. M. 1991, *ApJ*, 370, 495
- Ibata, R., Irwin, M. J., Ferguson, A. M. N., Lewis, G., & Tanvir, N. 2001, *Nature*, 412, 49
- Innanen, K. A., Harris, W. E., & Webbink, R. F. 1983, *AJ*, 88, 338
- Johnston, K. V. 1998, *ApJ*, 495, 297
- Johnston, K. V., Hernquist, L., & Bolte, M. 1996, *ApJ*, 465, 278
- Kelson, D. 2002, *ApJ*, in preparation
- Laird, J. B., Rupen, M. P., Carney, B. W., & Latham, D. W. 1988, *AJ*, 96, 1908
- Larson, R. B. 1974, *MNRAS*, 166, 585
- Newton, K., & Emerson, D. T. 1977, *MNRAS*, 181, 573
- Oke, J. B., Cohen, J. G., Carr, M., Cromer, J., Dingizian, A., Harris, F. H., Labrecque, S., Lucinio, R., Schall, W., Epps, H., & Miller, J. 1995, *PASP*, 107, 375
- Olszewski, E. W., Schommer, R. A., Suntzeff, N. B., & Harris, H. C. 1991, *AJ*, 101, 515
- Phillips, A. C., Guzmán, R., Gallego, J., Koo, D. C., Lowenthal, J. D., Vogt, N. P., Faber, S. M., & Illingworth, G. D. 1997, *ApJ*, 489, 543
- Ratnatunga, K. U., & Bahcall, J. N. 1985, *ApJS*, 59, 63
- Reitzel, D. B., & Guhathakurta, P. 1998, in *Galactic Halos*, ed. D. Zaritsky (ASP Conf. Series, No. 136), 30
- Reitzel, D. B., & Guhathakurta, P. 2000, in *The Galactic Halo: From Globular Clusters to Field Stars*, eds. A. Noels, P. Magain, D. Caro, E. Jehin, G. Parmentier, & A. Thoul (Proc. 35th Liège International Astrophys. Coll.), 365
- Reitzel, D. B., Guhathakurta, P., & Gould, A. 1998, *AJ*, 116, 707 (RGG)
- Rich, R. M., Corsi, C. E., Bellazzini, M., Federici, L., Cacciari, C., & Fusi Pecci, F. 2002, in *Extragalactic Star Clusters*, eds. E. K. Grebel, D. Geisler, & D. Minniti (IAU Symp. 207), in press (astro-ph/0106015)
- Rich, R. M., Mighell, K. J., Freedman, W. L., & Neill, J. D. 1996a, *AJ*, 111, 768

- Rich, R. M., Mighell, K. J., Freedman, W. L., & Neill, J. D. 1996b, in *Formation of the Galactic Halo...Inside and Out*, eds. H. Morrison & A. Sarajedini (ASP Conf. Series, No. 92), 544
- Rutledge, G. A., Hesser, J. E., Stetson, P. B., Mateo, M., Simard, L., Bolte, M., Friel, E., & Copin, Y. 1997a, *PASP*, 109, 883
- Rutledge, G. A., Hesser, J. E., & Stetson, P. B. 1997b, *PASP*, 109, 907
- Salpeter, E. E. 1955, *ApJ*, 121, 161
- Sarajedini, A., & Van Duyne, J. 2001, *AJ*, 122, 2444
- Schlegel, D. J., Finkbeiner, D. P., & Davis, M. 1998, *ApJ*, 500, 525
- Searle, L., & Zinn, R. 1978, *ApJ*, 225, 357
- Spinrad, H., & Taylor, B. J. 1969, *ApJ*, 157, 1279
- Spinrad, H., & Taylor, B. J. 1971, *ApJS*, 22, 445
- Stanek, K. Z., & Garnavich, P. M. 1998, *ApJ*, 503, L131
- Stetson, P. B. 1987, *PASP*, 99, 191
- Stetson, P. B. 1992, in *Astronomical Data Analysis Software*, eds. D. M. Worrall, C. Biemesderfer, & J. Barnes (ASP Conf. Series, No. 25), 297
- Suntzeff, N. B., & Kraft, R. P. 1996, *AJ*, 111, 1913
- Suntzeff, N. B., Mateo, M., Terndrup, D. M., Olszewski, E. W., Geisler, D., & Weller, W. 1993, *ApJ*, 418, 208
- Suntzeff, N. B., Schommer, R. A., Olszewski, E. W., & Walker, A. R. 1992, *AJ*, 104, 1743
- Tonry, J., & Davis, M. 1979, *AJ*, 84, 1511
- Wilkinson, M. I., & Evans, N. W. 1999, *MNRAS*, 310, 645
- Zinn, R. 1993, in *The Globular Cluster-Galaxy Connection*, eds. G. H. Smith & J. P. Brodie (ASP Conf. Series, No. 48), 38
- Zinn, R., & West, M. J. 1984, *ApJS*, 55, 45 (ZW)

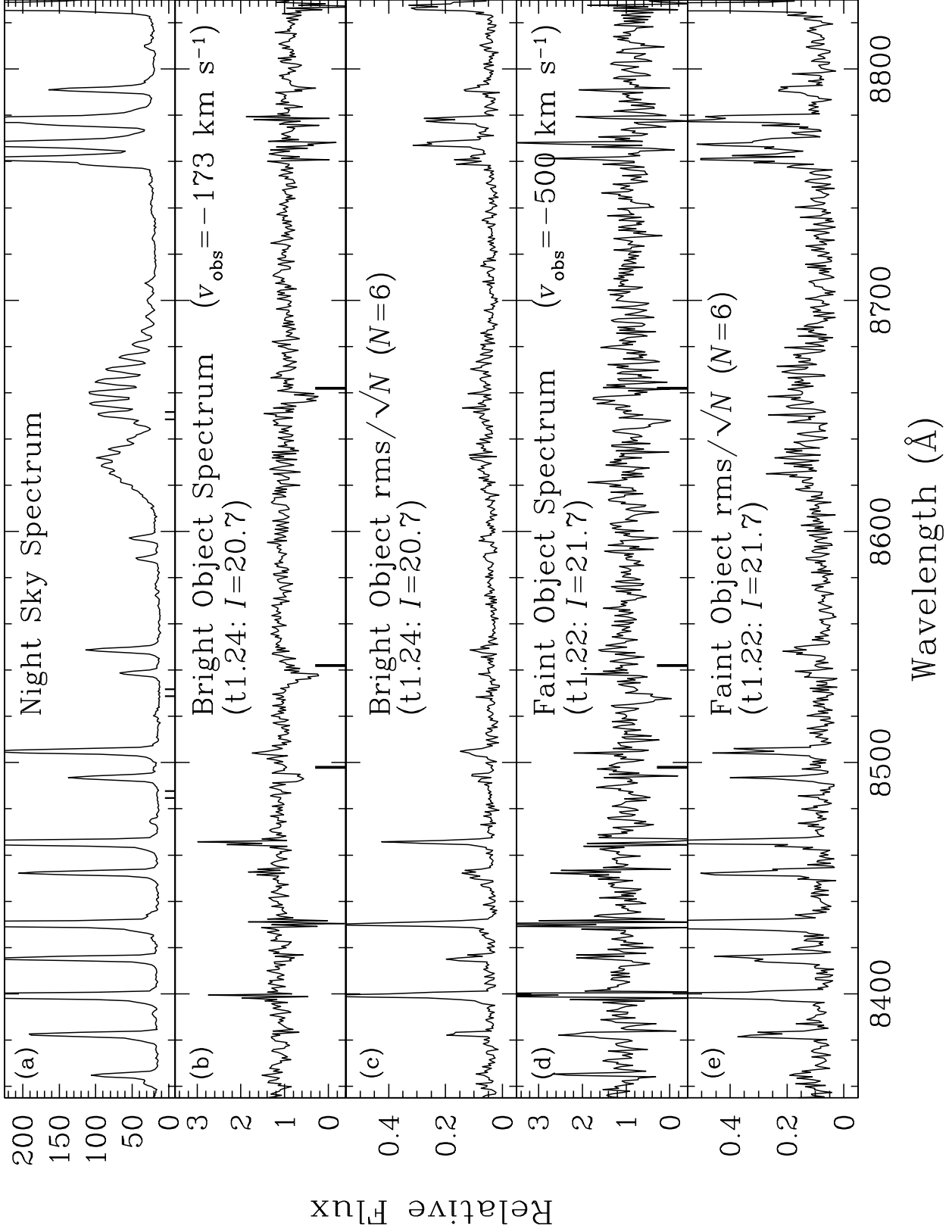


Fig. 1.— (a) Typical night sky emission-line spectrum in the region of the Ca II near-infrared triplet. The 3 pairs of bold line segments along the bottom of the panel mark the regions in which the Ca II lines would appear for objects in the radial velocity range, $-460 < v < -360$ km s⁻¹; these regions are in relatively clean parts of the spectrum which are not too badly affected by night sky emission lines. Thus, the observed lack of M31 giants in this velocity range is *not* a result of selection bias (see Fig. 21 and §5.3). (b) The spectrum of a typical bright ($I = 20.7$) object, t1.24 in Table 1, with the continuum normalized to unity. The rest-frame wavelengths of the Ca II near-infrared triplet are denoted by 3 bold line segments below the spectrum. The absorption lines in the spectrum are blueshifted by an amount corresponding to the observed radial velocity of the object, $v_{\text{obs}} = -173$ km s⁻¹ (prior to heliocentric correction). (c) The rms error per pixel of the mean spectrum, obtained by dividing the observed rms dispersion among the 6 individual spectral exposures by the square root of the number of exposures, $N = 6$. The rms error of the mean is about 0.05 or less for the most part, corresponding to a signal-to-noise ratio > 20 , except in the vicinity of strong night sky lines where the rms is boosted by increased photon noise and fringing. (d) Same as (b) for a typical faint ($I = 21.7$) object, t1.22, for which $v_{\text{obs}} = -500$ km s⁻¹. (e) Same as (c) for the faint object whose spectrum is shown in (d). The rms level is typically between 0.05 and 0.10 between strong night sky lines, corresponding to a signal-to-noise ratio between 10 and 20.

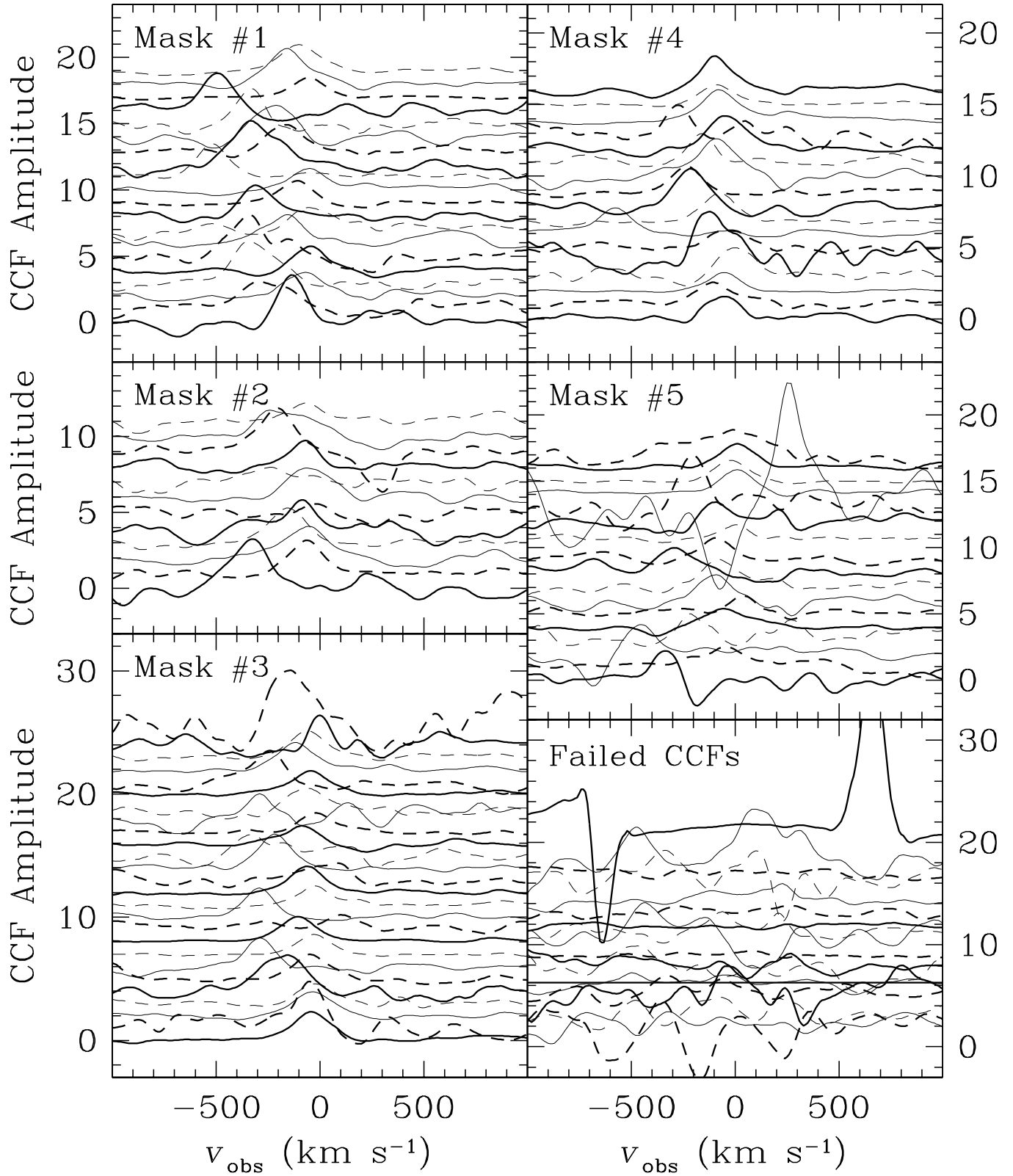


Fig. 2.— Cross correlation functions (CCFs) for all 112 objects for which spectroscopy is available: 99 M31 red giant candidates and 13 control sample stars. The 93 objects for which reliable velocity determination is possible are grouped by mask number: 20, 12, 26, 17, and 18 objects for masks 1–5, respectively. The CCFs in each panel are sorted in order of increasing object ID number (Tables 1 and 3) from bottom to top following the sequence of line types: bold solid, bold dashed, thin solid, thin dashed, bold solid, etc.. The CCF peaks tend to be concentrated around $v \approx -500$ to 0 km s^{-1} , a velocity range occupied by M31 red giants and foreground Milky Way dwarf stars. The 19 objects for which the velocity measurement fails are grouped together in the bottom right panel, sorted as before by object ID number and in the order mask 1–5. These CCFs are noticeably noisier than the rest.

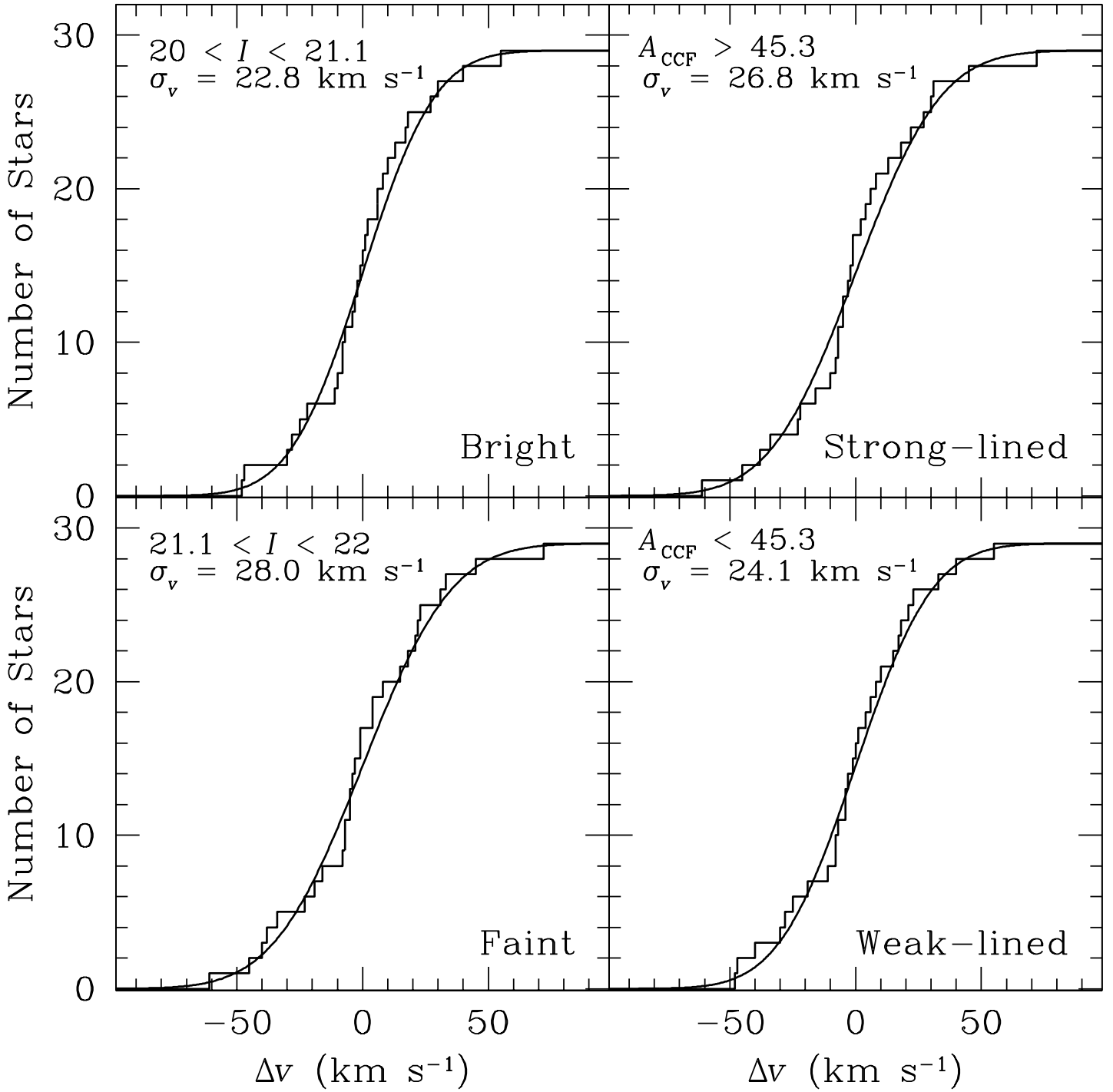


Fig. 3.— Cumulative distribution of radial velocity differences, derived by splitting the exposure time for each target in masks 1–4 into two independent coadds of two exposures each (see § 3.1). The bright ($I < 21.1$) and faint ($I > 21.1$) subsamples are shown in the upper-left and lower-left panels, respectively; the strong-lined ($A_{CCF} > \langle A_{CCF} \rangle$) and weak-lined ($A_{CCF} < \langle A_{CCF} \rangle$) subsamples are shown in the upper-right and lower-right panels, respectively. The solid curve is the best-fit Gaussian with σ_v^{pair} given for each distribution. The four subsamples show roughly similar distributions. The bright subsample has the smallest velocity measurement error. The strength of the Ca II absorption lines does not appear to have a large effect on the velocity measurement error.

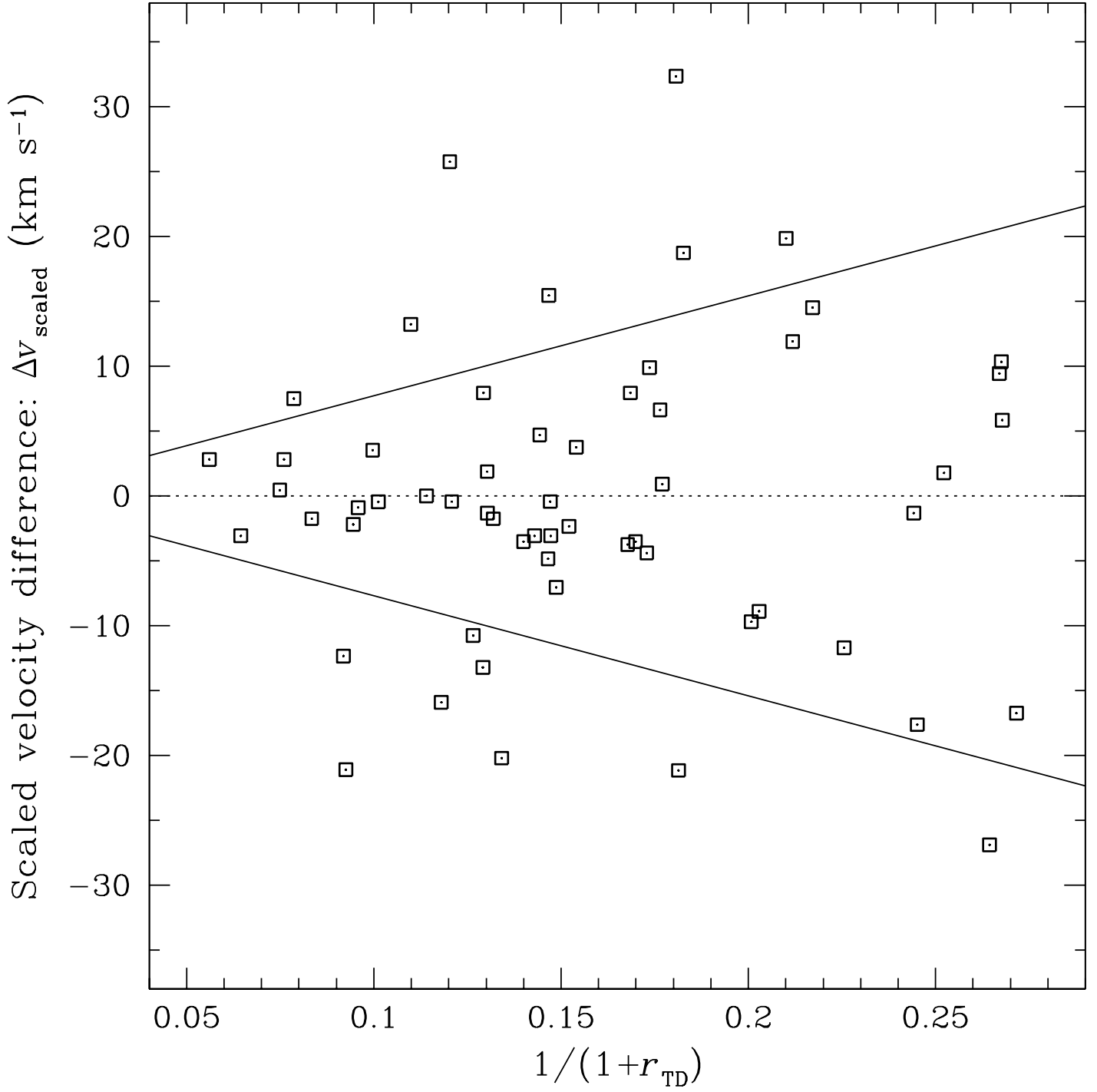


Fig. 4.— Radial velocity difference for each pair of split exposure coadds for targets in masks 1–4, scaled (down) to correspond to the total exposure time, plotted as a function of $(1 + r_{\text{TD}})^{-1}$, where r_{TD} is the usual Tonry-Davis (1979) parameter indicating the significance of the peak in the overall coadded CCF. The solid lines show an empirical formula for measuring the $\pm 1\sigma$ velocity error as described in § 3.1: $\pm 77 \text{ km s}^{-1}/(1 + r_{\text{TD}})$.

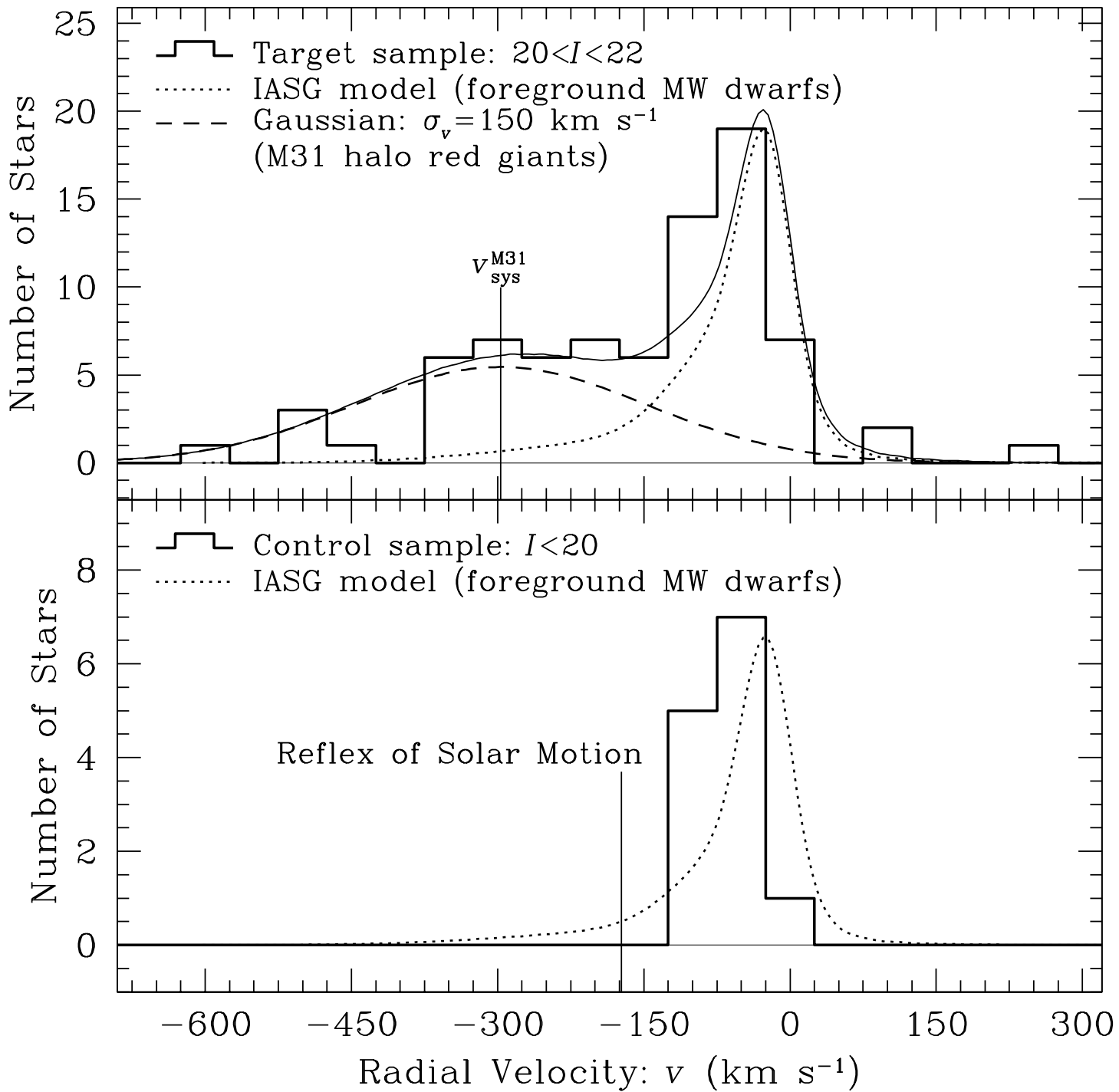


Fig. 5.— Distribution of heliocentric radial velocities for the main sample of M31 spectroscopic targets (upper panel) and control sample (lower panel). The main sample (histogram in upper panel) is well fit by the combination of a Gaussian of width $\sigma = 150 \text{ km s}^{-1}$ centered on M31’s systemic velocity of $v_{\text{sys}}^{\text{M31}} = -297 \text{ km s}^{-1}$ (dashed line) and the prediction of the IASG star count model of the Milky Way (Ratnatunga & Bahcall 1985), the taller dotted curve peaked at $v \approx -25 \text{ km s}^{-1}$. The solid curve is the sum of these two models and it is normalized to match the total number of objects in the histogram, 80. The IASG model curve in the lower panel is normalized to the number of objects in the control sample, 13. The reflex of the solar motion is indicated, the inverse of the projection of the solar rotation velocity vector in the direction of M31. The observed peak of the velocity distribution of foreground Galactic dwarf stars appears to be about $20 - 50 \text{ km s}^{-1}$ more negative than the prediction of the IASG model (both panels).

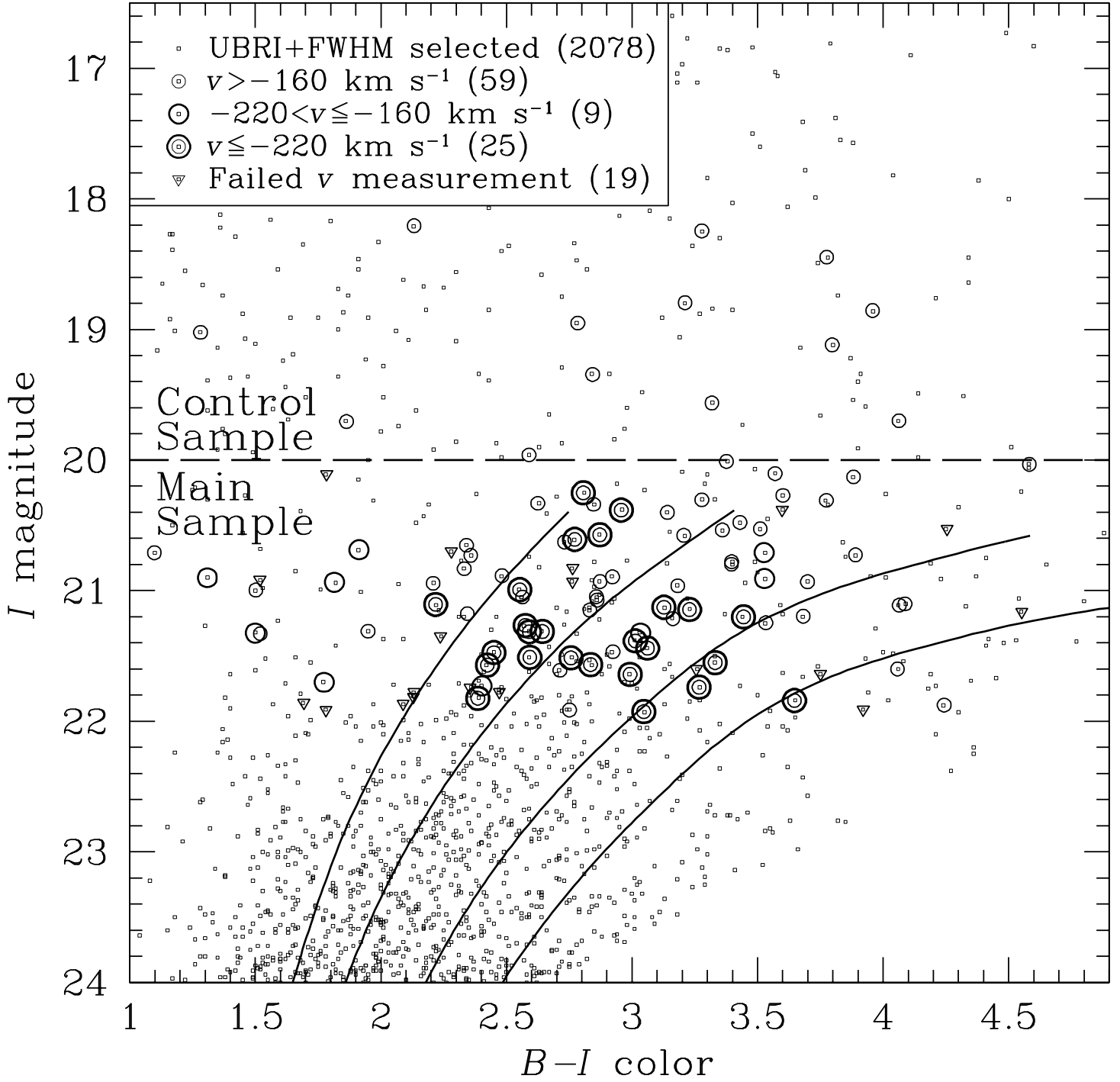


Fig. 6.— Color-magnitude diagram showing all *UBRI*- and FWHM-selected stellar candidates from the RGG photometric study (small squares). Larger circumscribed symbols indicate spectroscopic targets with: $v > -160 \text{ km s}^{-1}$ (thin circles), $-220 < v \leq -160 \text{ km s}^{-1}$ (bold circles), $v \leq -220 \text{ km s}^{-1}$ (bold+thin double circles), and those for which there is no reliable velocity measurement (triangles). The number of objects in each velocity category is indicated in parentheses; the number in the $v > -160 \text{ km s}^{-1}$ category includes all 13 control sample stars. Model red giant branch fiducials from Bergbusch & Vandenberg (2001) reddened by $\langle E(B - I) \rangle = 0.13$, the typical value derived from the Schlegel et al. (1998) dust map over the field of view of the spectroscopic targets, are plotted as solid lines with $[\text{Fe}/\text{H}]$ increasing from left to right: -2.31 , -1.41 , -0.71 , and -0.30 dex. The $v \leq -220 \text{ km s}^{-1}$ objects are secure M31 members; these span the range of colors occupied by the model isochrones indicating a roughly 2 dex metallicity spread in M31’s stellar halo. The bold and thin circles occupy increasingly larger $B - I$ color ranges due to increasing fractions of foreground contaminants in these subsamples.

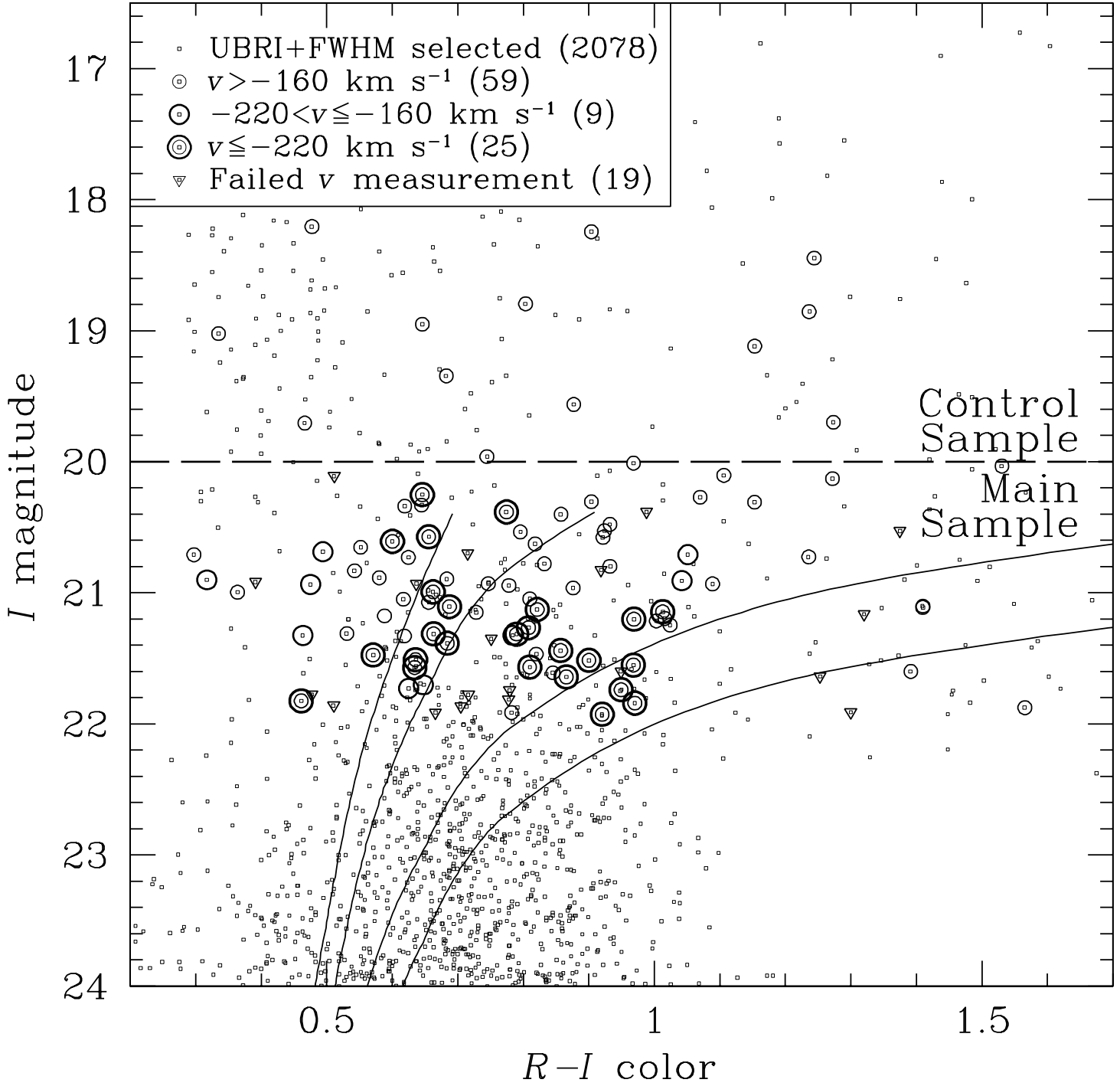


Fig. 7.— Same as Fig. 6, except $R - I$ is plotted on the abscissa instead of $B - I$. The location of M31 red giants relative to foreground Milky Way dwarfs and background field galaxies is expected to be different in $(B - I, I)$ versus $(R - I, I)$ CMDs. For example, note the difference in the shape and position of the set of isochrones in the two CMDs in relation to the distribution of foreground stars with $I < 20$. As expected, the secure sample of M31 giants ($v < -220 \text{ km s}^{-1}$) is shifted further to the blue (left) in this figure than in Fig. 6 relative to the rest of the data points.

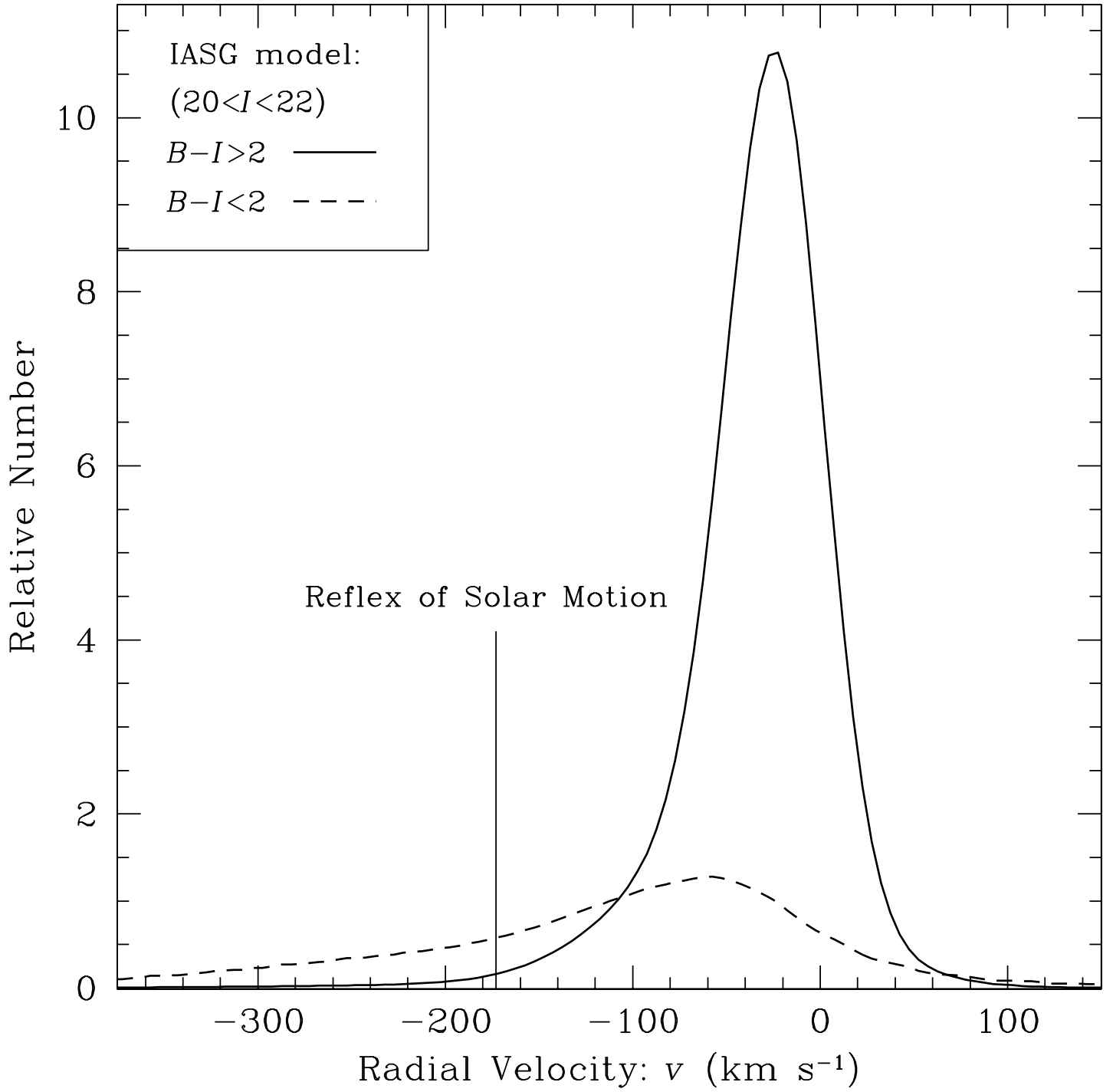


Fig. 8.— The predicted radial velocity distribution of foreground Galactic dwarf stars in direction of M31 from the IASG model (Ratnatunga & Bahcall 1985). The solid curve is for red stars ($B - I > 2$) and the dashed curve is for blue stars ($B - I < 2$), both for the apparent-magnitude range, $20 < I < 22$. The foreground contamination for the $v < -160$ km s⁻¹ subsamples is almost entirely in the form of turnoff stars in the Milky Way with $B - I < 2$. The solar reflex motion in the direction of M31 is indicated (same as in lower panel of Fig. 5).

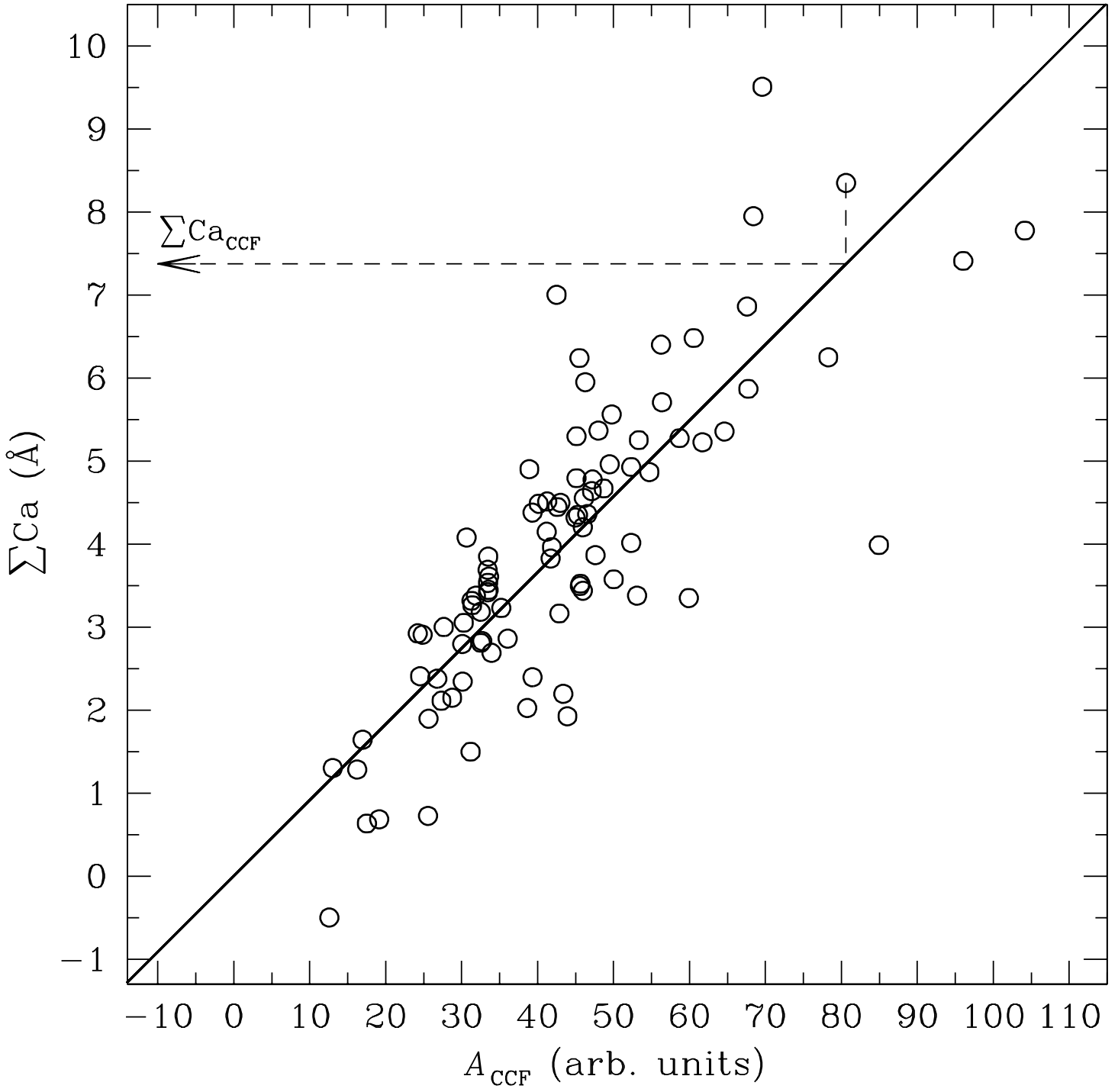


Fig. 9.— The weighted, summed Ca II line strength, ΣCa , plotted against the strength of (area under) the cross correlation peak, A_{CCF} . Tests show that the A_{CCF} statistic is less noisy than the directly measured line strength, ΣCa , so we prefer to use the former for metallicity determination. The dashed lines and arrow demonstrate how the *effective* summed line strength, $\Sigma\text{Ca}_{\text{CCF}}$, is calculated from A_{CCF} using the mean empirical relation shown as a solid line (§ 4.2.2).

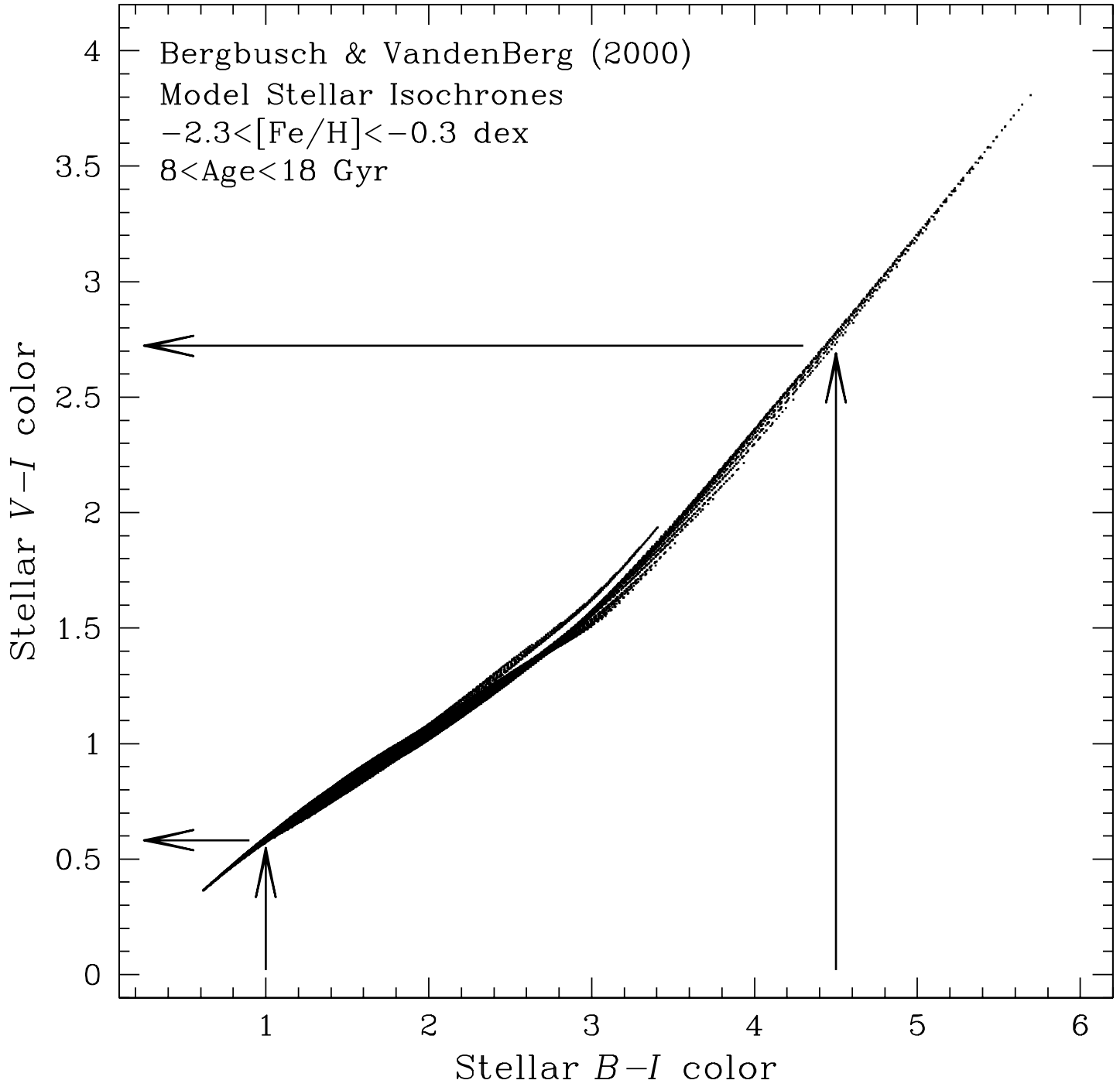


Fig. 10.— Color-color diagram of $V - I$ versus $B - I$ for the Bergbusch & Vandenberg (2001) model stellar isochrones with metallicities in the range $-2.31 \leq [\text{Fe}/\text{H}] \leq -0.3$ dex and ages in the range $8.0 \leq t \leq 18.0$ Gyr. The arrows demonstrate how the apparent V_{synth} magnitude of a star is estimated by interpolating between the measured (and subsequently dereddened) B and I apparent magnitudes. The range of $B - I$ over which this interpolation is carried out is spanned by the two pairs of arrows. Even though the model isochrones span a wide range of metallicity and age, they map onto a well-defined, narrow locus in the $(V - I, B - I)$ plane.

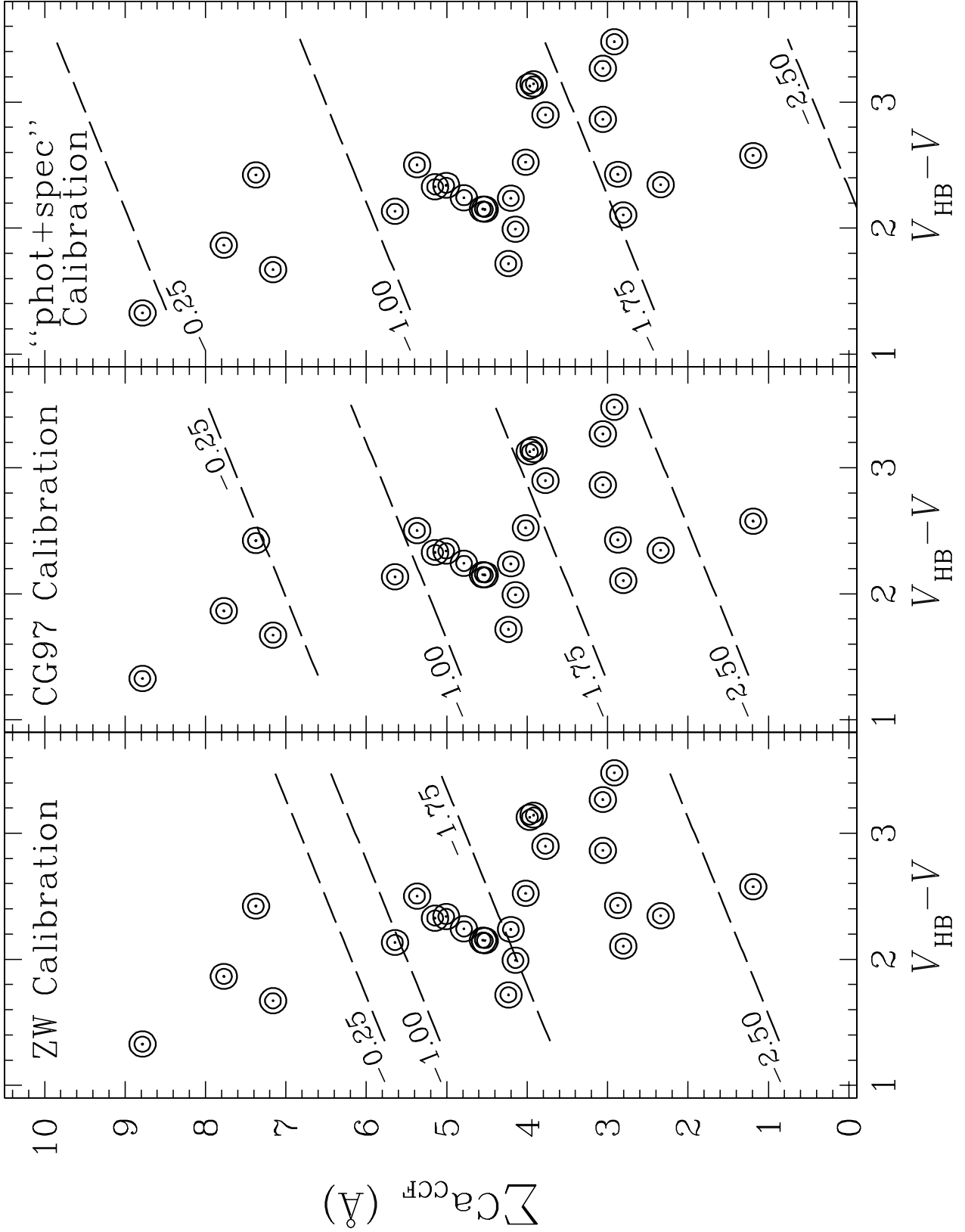


Fig. 11.— The effective weighted sum of the equivalent widths of the Ca II lines, $\Sigma\text{Ca}_{\text{CCF}}$, plotted versus the “distance” (in mag) above the level of the horizontal branch, $V_{\text{HB}} - V$, for objects with $v \leq -220 \text{ km s}^{-1}$. The quantity $\Sigma\text{Ca}_{\text{CCF}}$ is derived from the strength of the cross-correlation peak using an empirical scaling between this quantity and the directly-measured Ca II equivalent width (§ 4.2.2). Dashed lines of constant $[\text{Fe}/\text{H}]$ are shown for the Zinn-West and Carretta-Gratton metallicity scales (left and middle panels, respectively), and for an empirical calibration of the reduced Ca II equivalent width based on photometric metallicity estimates dubbed $[\text{Fe}/\text{H}]_{\text{phot+spec}}$ (right panel). This empirical “phot+spec” calibration of $[\text{Fe}/\text{H}]$ is merely put forward to demonstrate that the Ca II line strength is tightly correlated with the photometric $[\text{Fe}/\text{H}]$ estimate for M31 giants (§ 4.3); $[\text{Fe}/\text{H}]_{\text{phot+spec}}$ is *not* to be treated as a ‘true’ metallicity scale or as an alternative to ZW and CG97 calibrations.

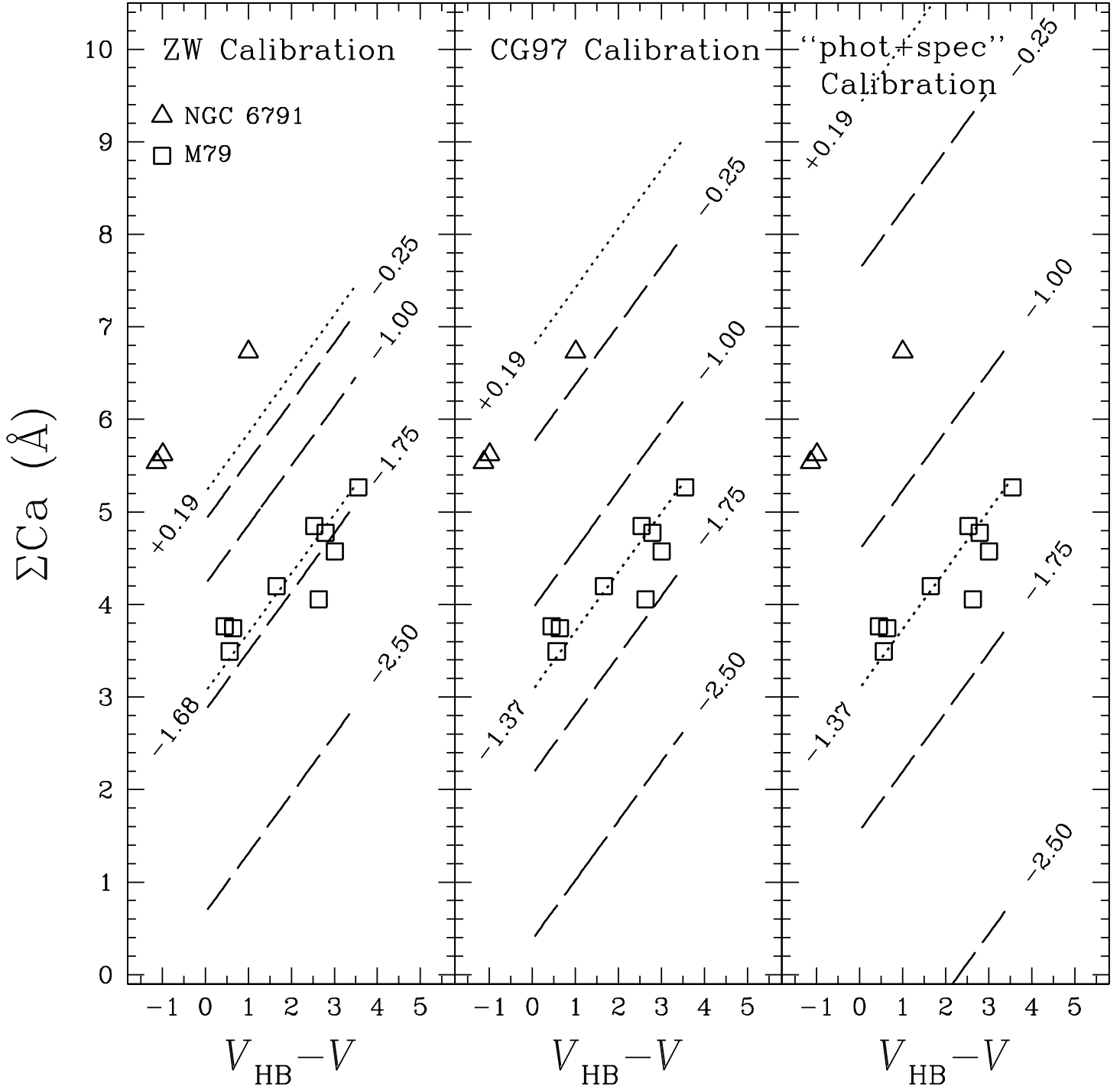


Fig. 12.— Same as Fig. 11 for red giants in two Galactic star clusters of known metallicity that are used to check the calibration of the spectroscopic $[\text{Fe}/\text{H}]$ scale: M79 with $[\text{Fe}/\text{H}]_{\text{ZW}} = -1.68$ dex and $[\text{Fe}/\text{H}]_{\text{CG97}} = -1.37$ dex (squares) and NGC 6791 with $[\text{Fe}/\text{H}]_{\text{ZW}} = +0.19$ dex (triangles). There is no $[\text{Fe}/\text{H}]$ measurement for NGC 6791 on the Carretta-Gratton scale, so the Zinn-West value of $+0.19$ dex is used in all three panels. The CG97 value for M79 is adopted for the empirical “phot+spec” calibration. The dotted lines indicate the metallicity of M79 and NGC 6791 for each calibration, marking the expected location of cluster red giants in the plots. The large discrepancy between the expected versus observed location of NGC 6791 giants in the “phot+spec” panel indicates that this empirical calibration relation is inaccurate at the high-metallicity end.

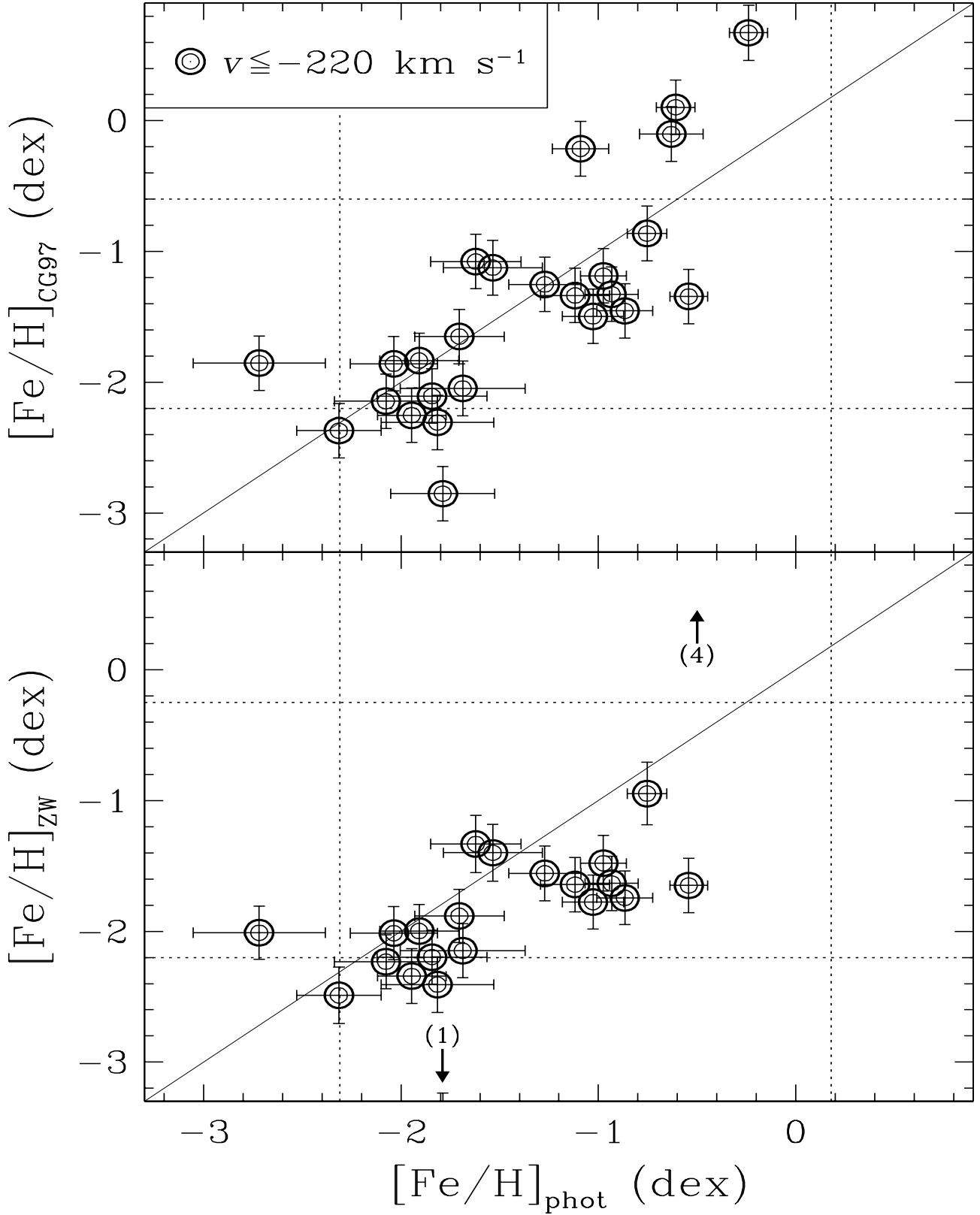


Fig. 13.— A star-by-star comparison of the photometric versus spectroscopic $[\text{Fe}/\text{H}]$ estimates for stars with $v \leq -220 \text{ km s}^{-1}$. The Carretta-Gratton and Zinn-West calibrations of the spectroscopic metallicity scales are shown in the upper and lower panels, respectively. The photometric estimate is based on the location of the star in the $(B - I, I)$ CMD. Also indicated are 1σ errors in each of the three $[\text{Fe}/\text{H}]$ estimates (§§ 4.1.2 and 4.2.3). Four objects (possible M31 disk stars/metal-rich debris—§ 5.3) are above the upper end and one object is below the lower end of the displayed y -axis range in the lower panel (see arrows). The calibration range for each method is indicated by dotted lines. The $[\text{Fe}/\text{H}]_{\text{CG97}}$ estimate correlates reasonably well with $[\text{Fe}/\text{H}]_{\text{phot}}$ over a wide range of metallicities; $[\text{Fe}/\text{H}]_{\text{ZW}}$ tends to be somewhat lower than $[\text{Fe}/\text{H}]_{\text{phot}}$ within the calibrated range and substantially higher than $[\text{Fe}/\text{H}]_{\text{phot}}$ beyond the upper end of the calibrated range where the cubic ZW relation diverges.

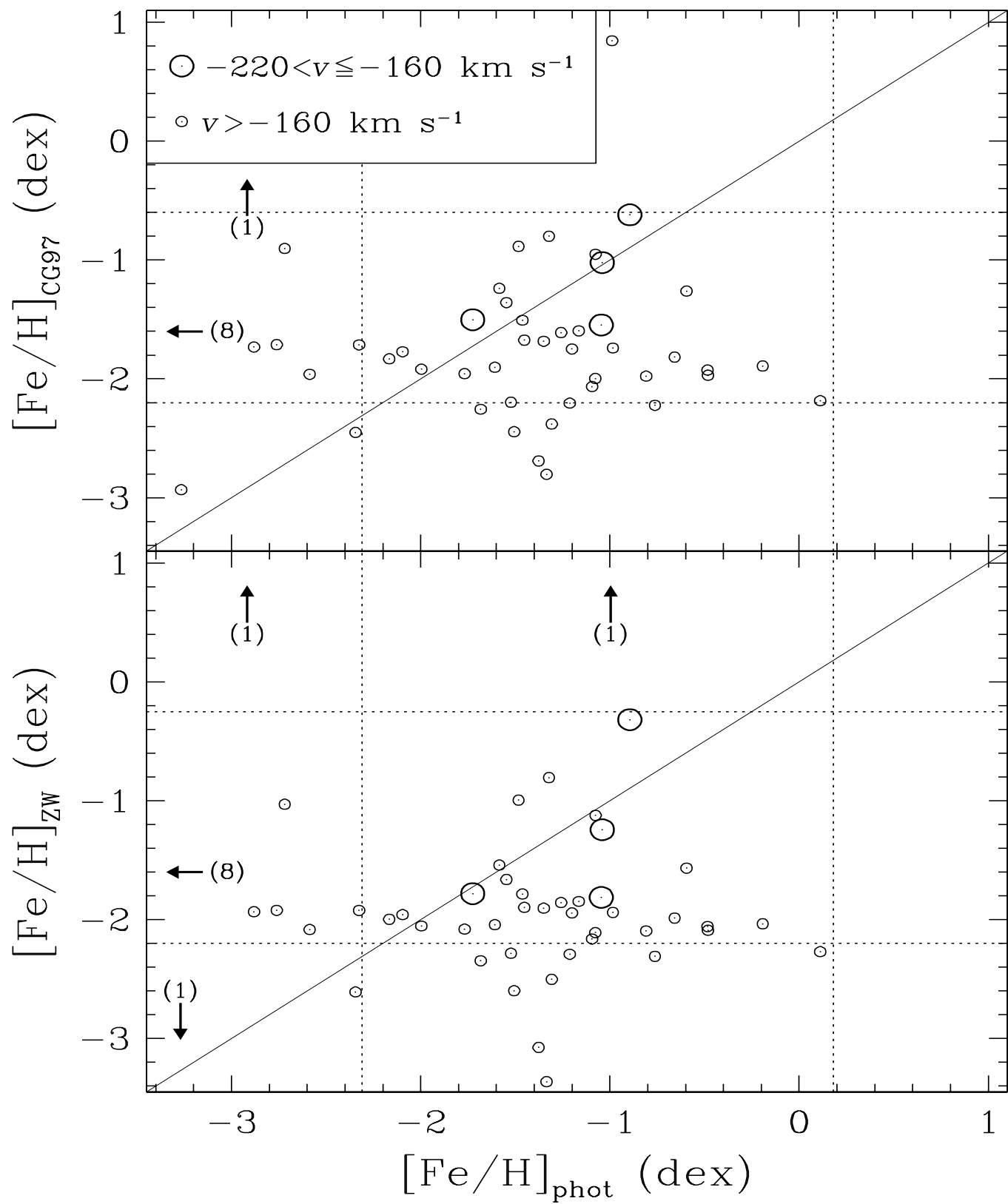


Fig. 14.— Same as Fig. 13 for objects with $v > -160 \text{ km s}^{-1}$ (small thin circles) and $-220 < v \leq -160 \text{ km s}^{-1}$ (large bold circles). Objects which lie beyond the displayed range of the plots are indicated by arrows with the number of objects in parentheses. Note the lack of an overall correlation in this plot in contrast to Fig. 13. It is likely that a handful of M31 red giants (< 10) are hidden in this plot, and while they might lie close to the $x = y$ line, their correlation is swamped by the vast majority of contaminating foreground Milky Way stars which are understandably uncorrelated. In particular, the four stars with $-220 < v \leq -160 \text{ km s}^{-1}$ that appear in this plot (red subset) are expected to be M31 red giants, and it is reassuring that these lie relatively close to the $x = y$ line.

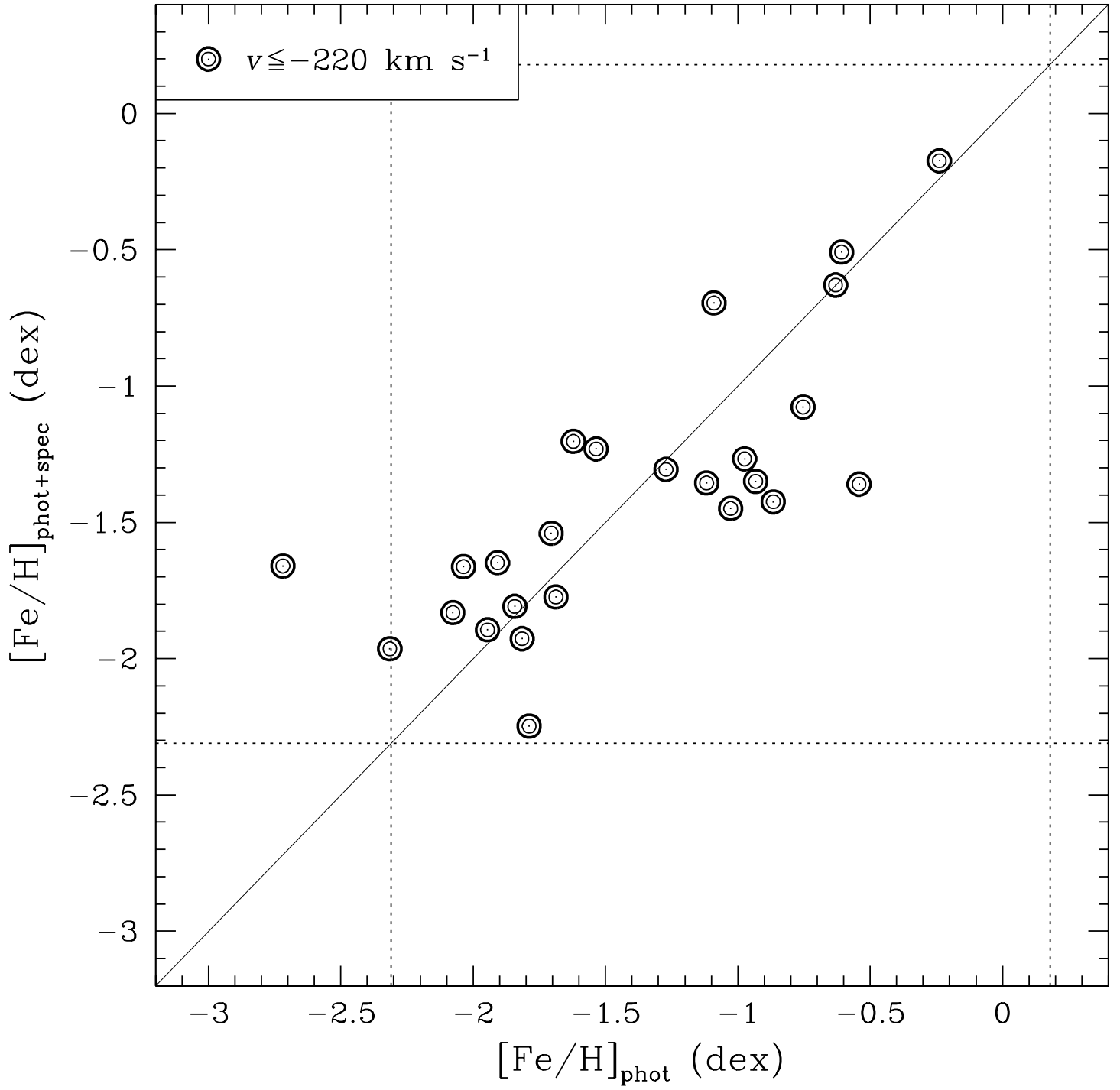


Fig. 15.— Spectroscopic estimate of the metallicity using the empirical “phot+spec” calibration relation, $[\text{Fe}/\text{H}]_{\text{phot+spec}}$ (§ 4.3), plotted versus the photometric estimate of the metallicity, $[\text{Fe}/\text{H}]_{\text{phot}}$, for stars with $v \leq -220 \text{ km s}^{-1}$. Calibration ranges for the two methods are indicated by the dotted lines. The clear trend seen in this plot indicates that the Ca II line strength of a star correlates reasonably well with its location in the $(B - I, I)$ CMD.

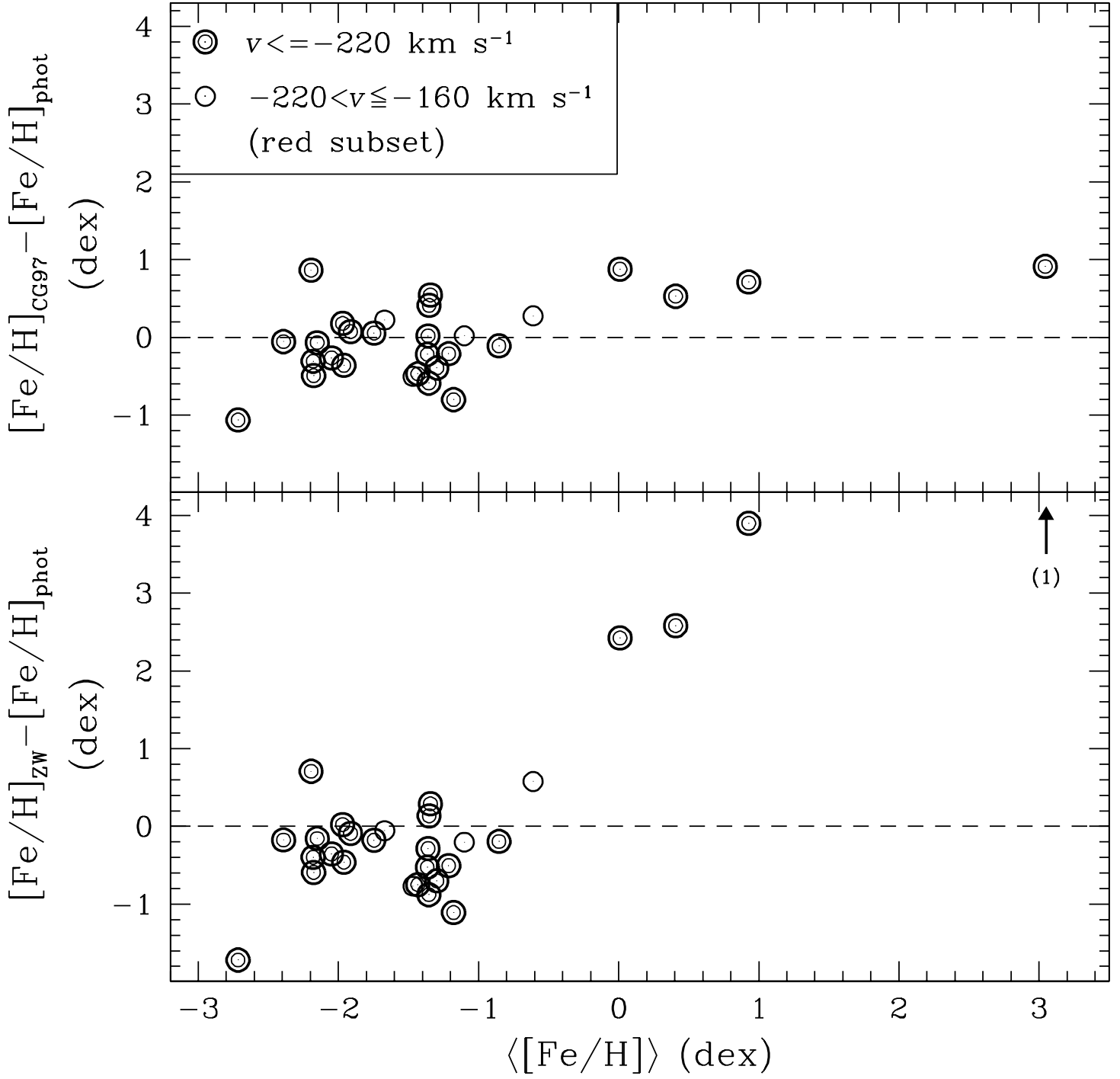


Fig. 16.— (*Upper panel*) Difference between the spectroscopic metallicity estimate on the Carretta-Gratton scale and the photometric estimate plotted versus $\langle[\text{Fe}/\text{H}]\rangle$, the average of three metallicity estimates, two spectroscopic (CG97 and ZW) and one photometric, for the secure sample of 29 M31 red giants. This mean $[\text{Fe}/\text{H}]$ value is only used to provide a common scale on which to rank stars in our comparison of the different metallicity measurement methods. There are four stars with solar/super-solar $\langle[\text{Fe}/\text{H}]\rangle$ values that lie systematically above the zero line (§ 5.3). (*Lower panel*) Same as upper panel, except the difference is with respect to the spectroscopic metallicity estimate on the Zinn-West scale. The extrapolation of the cubic ZW relation diverges at high metallicities beyond the calibrated range; the arrow indicates that one star is located beyond the upper end of the displayed y -axis range.

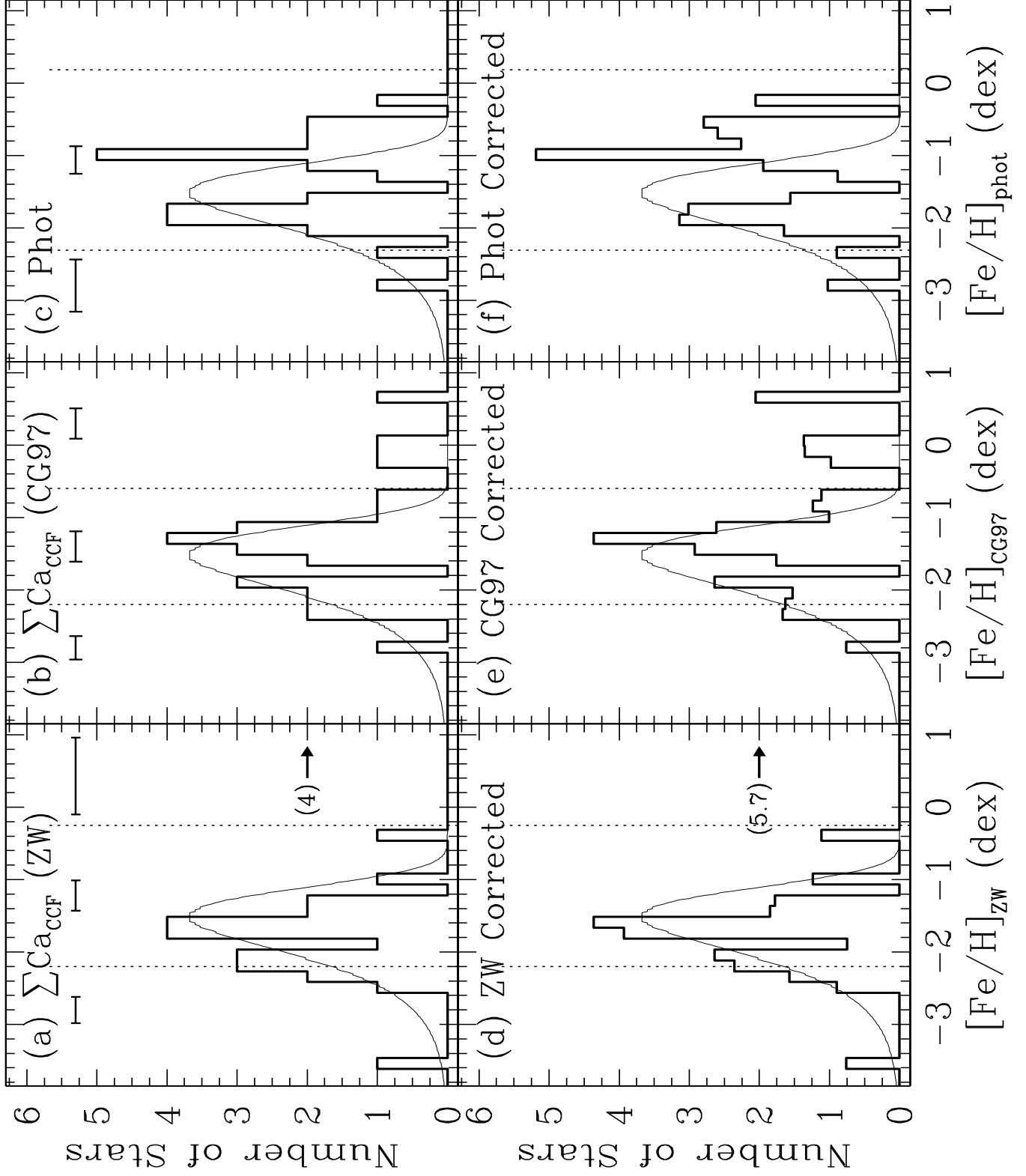


Fig. 17.— (a)–(c) Metallicity distribution (uncorrected) for the secure sample of 29 M31 red giants on the spectroscopic Zinn-West and Carretta-Gratton scales and photometric scales, respectively (bold histograms). The calibration range for each method is indicated by the vertical dotted lines. The typical 1σ measurement errors in $[\text{Fe}/\text{H}]$ for each method for objects inside and outside the calibrated ranges are shown above each histogram. The $[\text{Fe}/\text{H}]$ distribution for a steady gas loss model with $[\text{Fe}/\text{H}]_0 = -10.0$ dex and $\langle[\text{Fe}/\text{H}]\rangle = -1.5$ dex is shown as a thin solid curve; it is a reasonably good match to the observations. All three metallicity scales show a large spread with tails extending toward the low and high ends of the distribution. (d)–(f) Same as (a)–(c), except the metallicity distributions are corrected for the bias against high-metallicity stars caused by the drop in I_{TRGB} and incompleteness at the faint end of the secure sample. Each star is weighted by the inverse of the selection efficiency function (solid line in Fig. 20) and the histograms are normalized by average weight per star in the sample so as to preserve the total area at the actual number of stars in the secure M31 sample, 29 (§ 5.2). The arrows in the left panels indicates that there are 4 stars beyond the upper end of the displayed $[\text{Fe}/\text{H}]_{\text{ZW}}$ range, or 5.7 stars after the metallicity-bias correction.

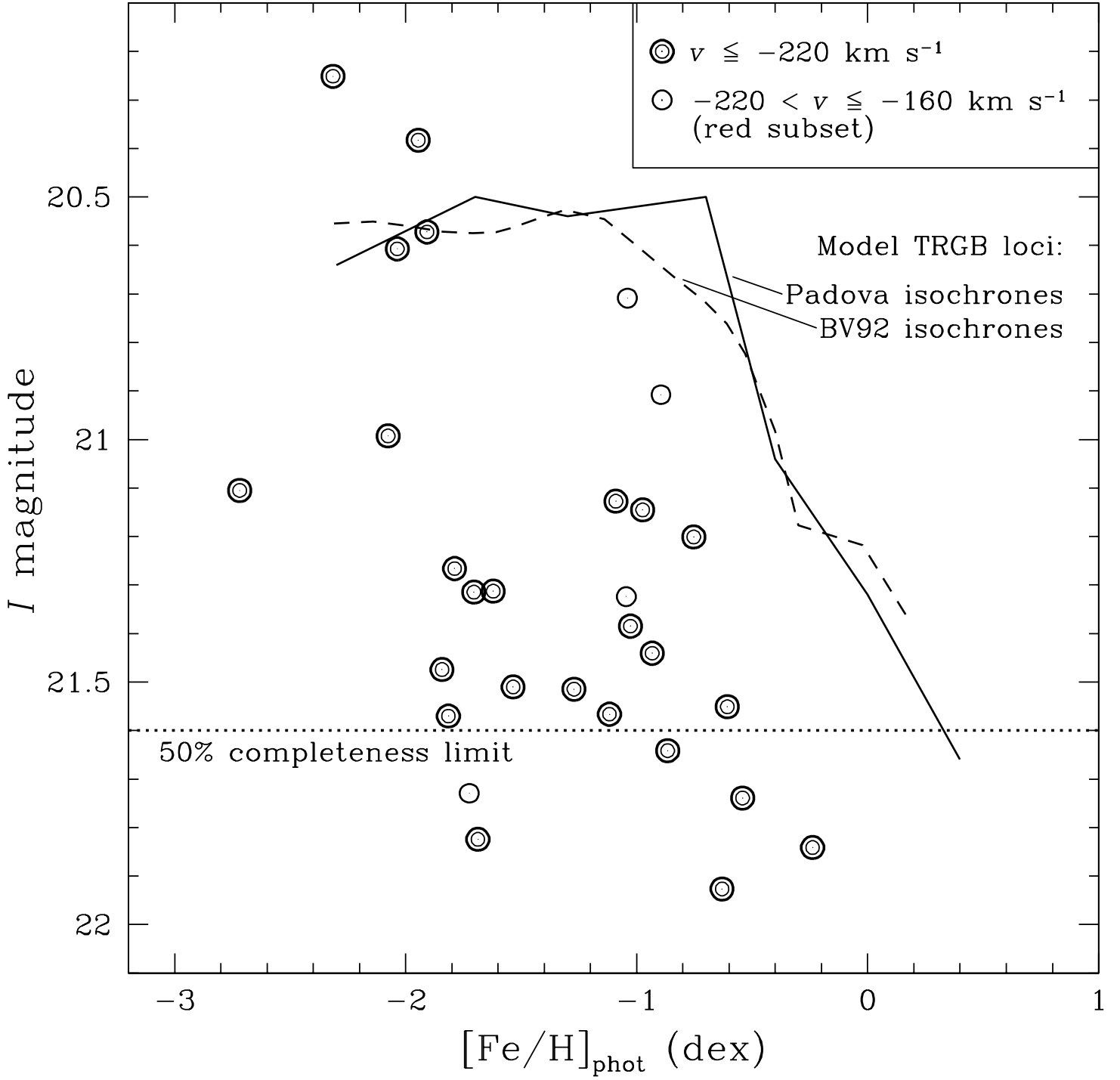


Fig. 18.— Apparent I -band magnitude versus photometric metallicity estimate for the secure M31 giant sample. Double circles indicate objects with $v \leq -220$ km s $^{-1}$; open circles represent the red subset of objects with $-220 < v \leq -160$ km s $^{-1}$. The expected locus of the tip of M31’s red giant branch is derived from the Padova group’s (Bertelli et al. 1994; Girardi et al. 1996) model isochrones (solid line) and Bergbusch & Vandenberg (1992) model isochrones (dashed line). The brightness of the tip of the RGB drops significantly for $[\text{Fe}/\text{H}] \gtrsim -1$ dex, and this tends to bias any magnitude-limited sample against high-metallicity red giants. The dotted horizontal line marks the estimated 50% completeness limit for the secure sample (§ 5.2).

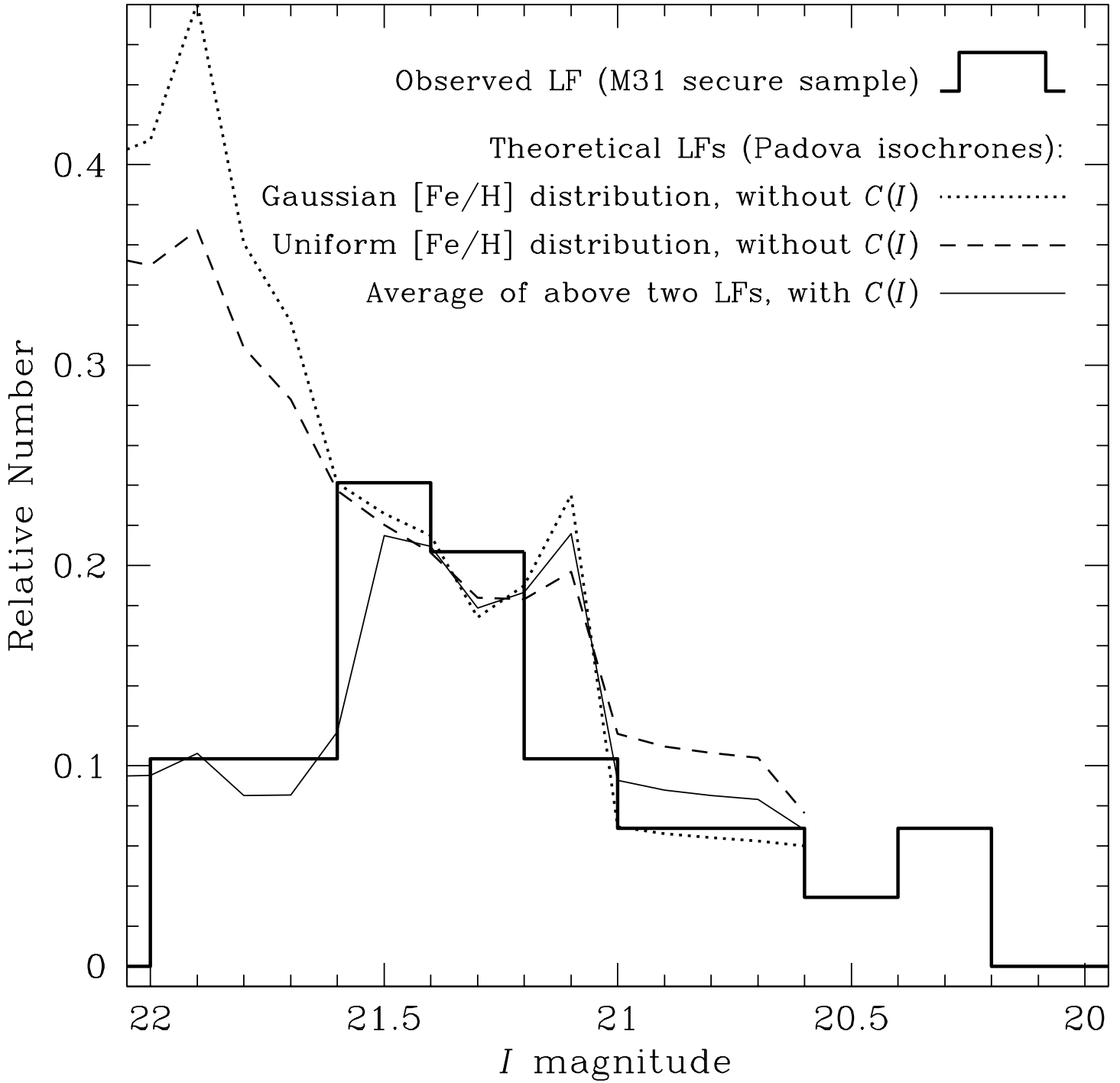


Fig. 19.— Distribution of I -band magnitudes for the secure M31 giant sample (bold histogram) compared to theoretical red giant luminosity functions derived from the Padova group’s isochrones (Bertelli et al. 1994; Girardi et al. 1996) for two assumed $[\text{Fe}/\text{H}]$ distributions: Gaussian, comparable to that observed in M31’s halo (dotted line), and uniform over the range $-2.3 < [\text{Fe}/\text{H}] < +0.4$ dex (dashed line). The model LFs are normalized to match the data at the bright end. The thin solid line is the average of these two model LFs with a faint-end exponential cutoff applied to mimic the decrease in completeness fraction of the secure sample with decreasing brightness; it is a good match to the observed distribution (see § 5.2).

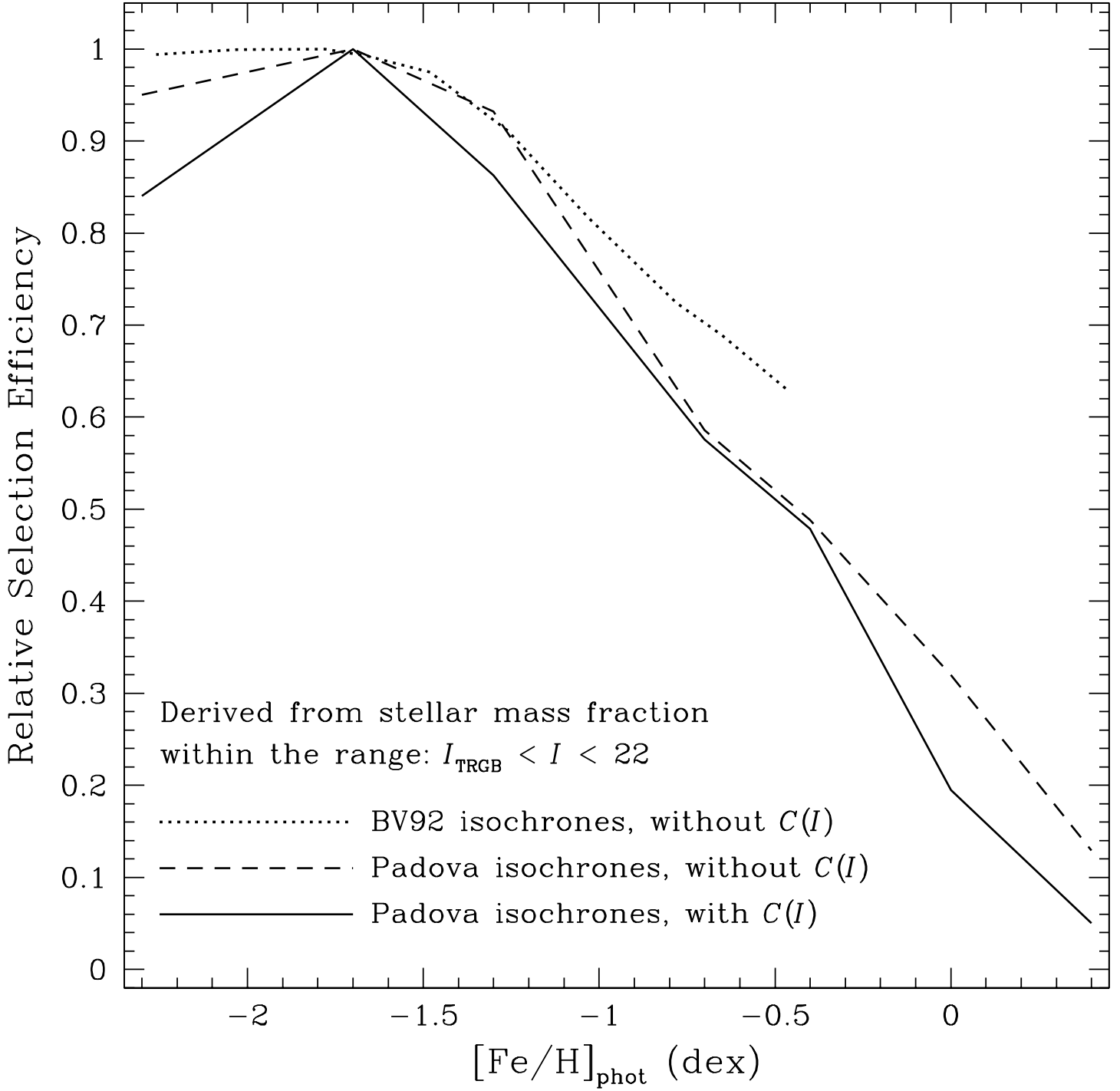


Fig. 20.— Relative selection efficiency as a function of $[\text{Fe}/\text{H}]_{\text{phot}}$ for the secure sample of M31 red giants. The selection efficiency is derived from the mass fraction in the apparent-magnitude range, $20 < I < 22$, or effectively, $I_{\text{TRGB}} < I < 22$, in theoretical isochrone population functions. The solid line is based on the Padova group’s isochrones (Bertelli et al. 1994; Girardi et al. 1996) accounting for the fact that the completeness level of the secure M31 sample falls off toward $I = 22$ (§ 5.2); the reciprocal of this is used to correct for the bias against high-metallicity stars. For comparison, the dashed line also represents a calculation based on the Padova group’s isochrones but with no correction for faint-end incompleteness [$C(I) = 1$], while the dotted line is based on the Bergbusch & Vandenberg (1992) isochrones and also ignores the completeness correction. The selection efficiency is normalized to unity at low metallicities where it is roughly constant; it drops linearly with increasing metallicity for $[\text{Fe}/\text{H}] \gtrsim -1.5$ dex to a value of about 0.5 at $[\text{Fe}/\text{H}] = -0.5$ dex. The drop in selection efficiency toward high $[\text{Fe}/\text{H}]$ is slightly steeper if the completeness function is included in the calculation (solid vs. dashed lines), and significantly steeper for the Padova isochrones than the Bergbusch & Vandenberg isochrones (dashed vs. dotted lines). Details of the $[\text{Fe}/\text{H}]$ selection efficiency calculation are in § 5.2.

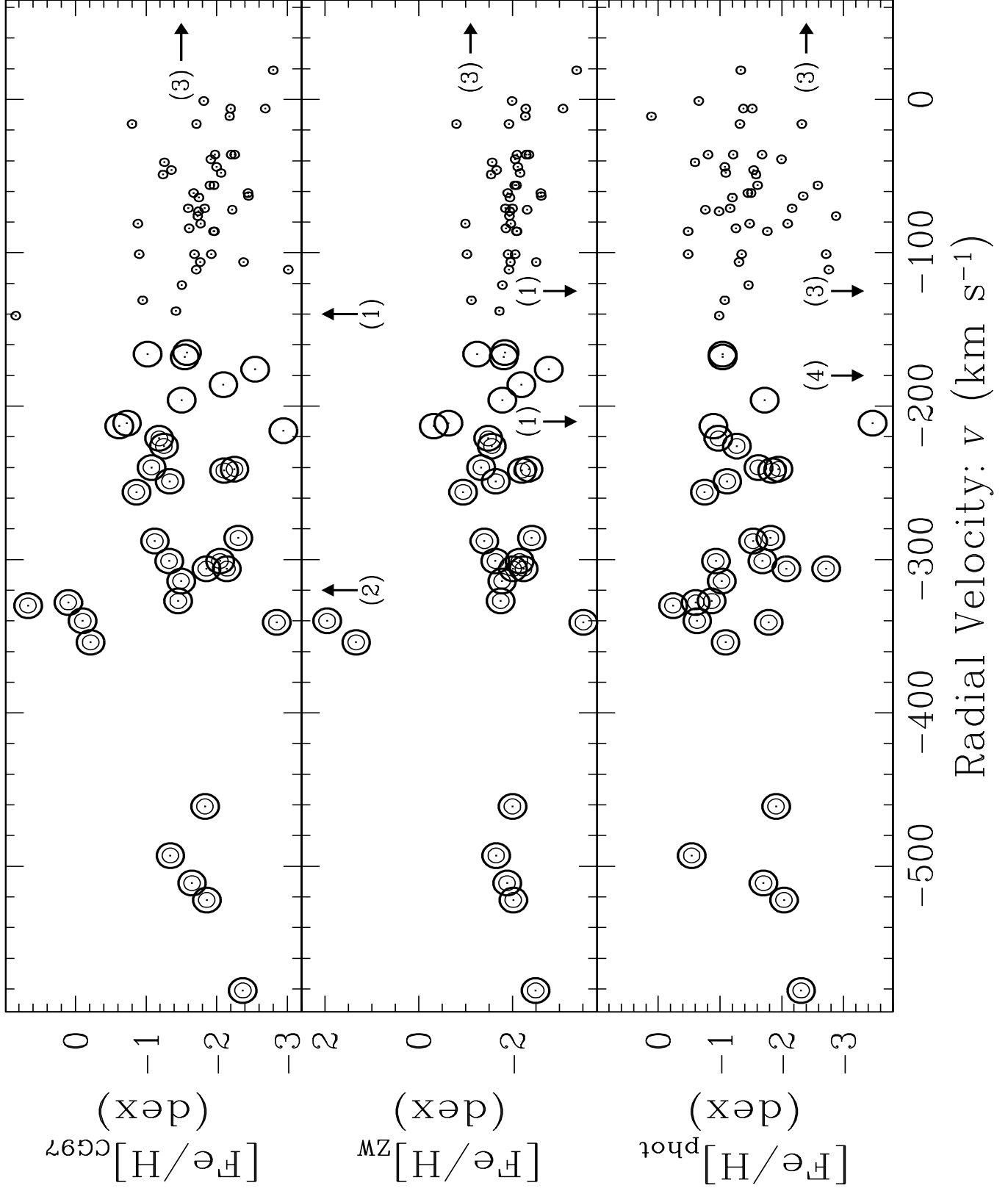


Fig. 21.— Metallicity on the spectroscopic Carretta-Gratton (top) and Zinn-West (middle) scales and photometric scale (bottom) plotted versus radial velocity: $v > -160 \text{ km s}^{-1}$ (small circles), $-220 < v \leq -160 \text{ km s}^{-1}$ (large circles), and $v \leq -220 \text{ km s}^{-1}$ (large double circles). Objects lying beyond the limits of the plot are indicated by an arrow and the number of such objects in each velocity category; of the three stars beyond the right edge, one lies beyond the upper end of the displayed y -axis range in the top and middle panels, while another lies beyond the lower end of the y range in the middle panel. There are four high-metallicity M31 red giants in the top panel with $v \approx -340 \text{ km s}^{-1}$. They are near the upper end of the $[\text{Fe}/\text{H}]_{\text{phot}}$ distribution and are the 3rd–6th most metal-rich on the ZW and CG97 scales (the two objects with stronger Ca II lines are probably *not* M31 halo giant stars). The velocities of these four metal-rich giants are consistent with that expected for M31 disk stars on the minor axis, $v \approx v_{\text{sys}}^{\text{M31}} = -297 \text{ km s}^{-1}$.

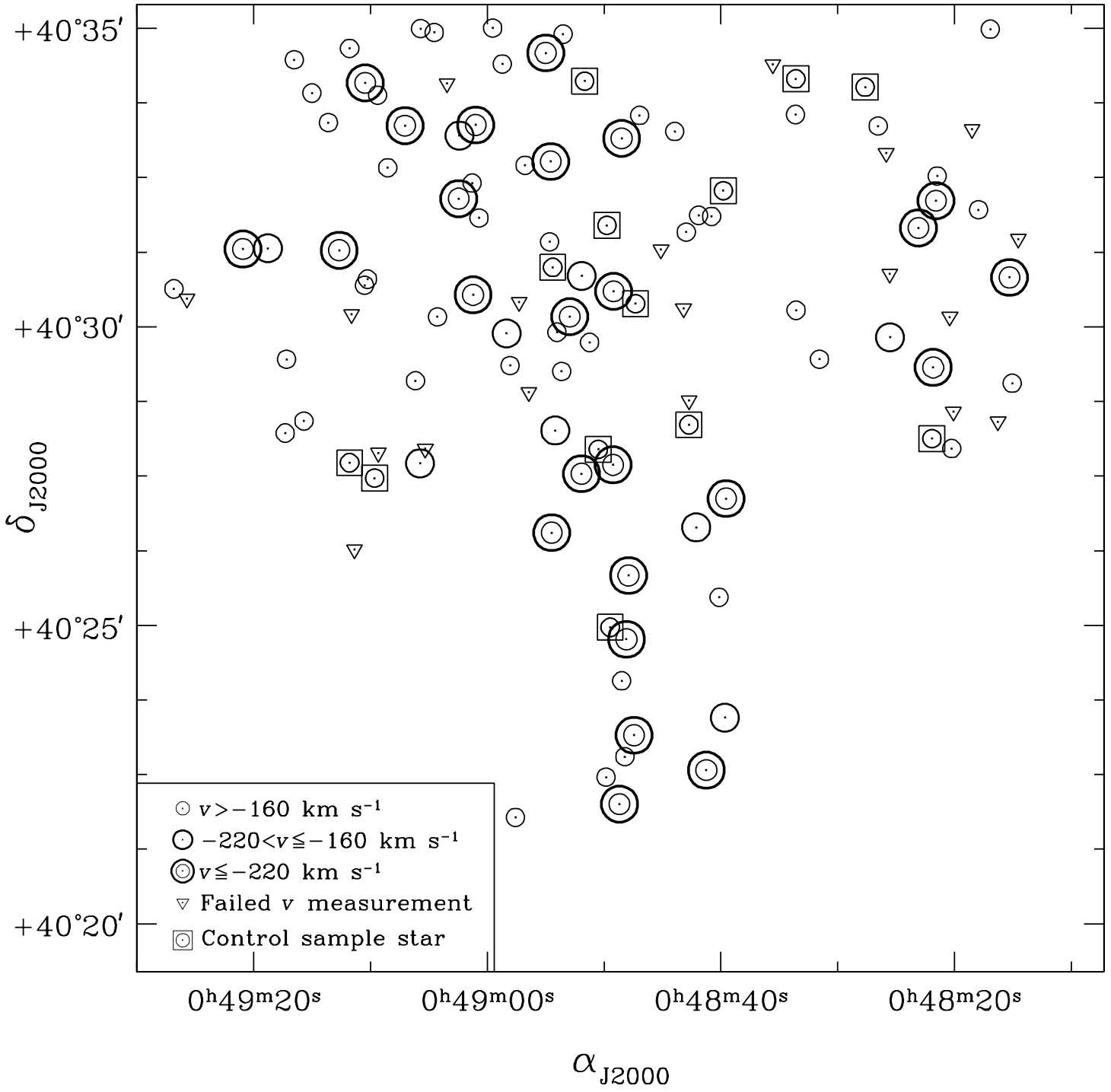


Fig. 22.— The location on the sky of all 112 objects in the spectroscopic sample grouped by radial velocity: $v > -160 \text{ km s}^{-1}$ (small circles), $-220 < v \leq -160 \text{ km s}^{-1}$ (large circles), $v \leq -220 \text{ km s}^{-1}$ (large double circles), and objects for which there is no reliable measurement of radial velocity (triangles). An extra square has been placed around each of the 13 control sample stars; all of them have radial velocities $v > -160 \text{ km s}^{-1}$. The shape of the overall “footprint” of the sample is determined by the relative locations and orientations of the 5 multi-slit masks used for the LRIS spectroscopic observations.

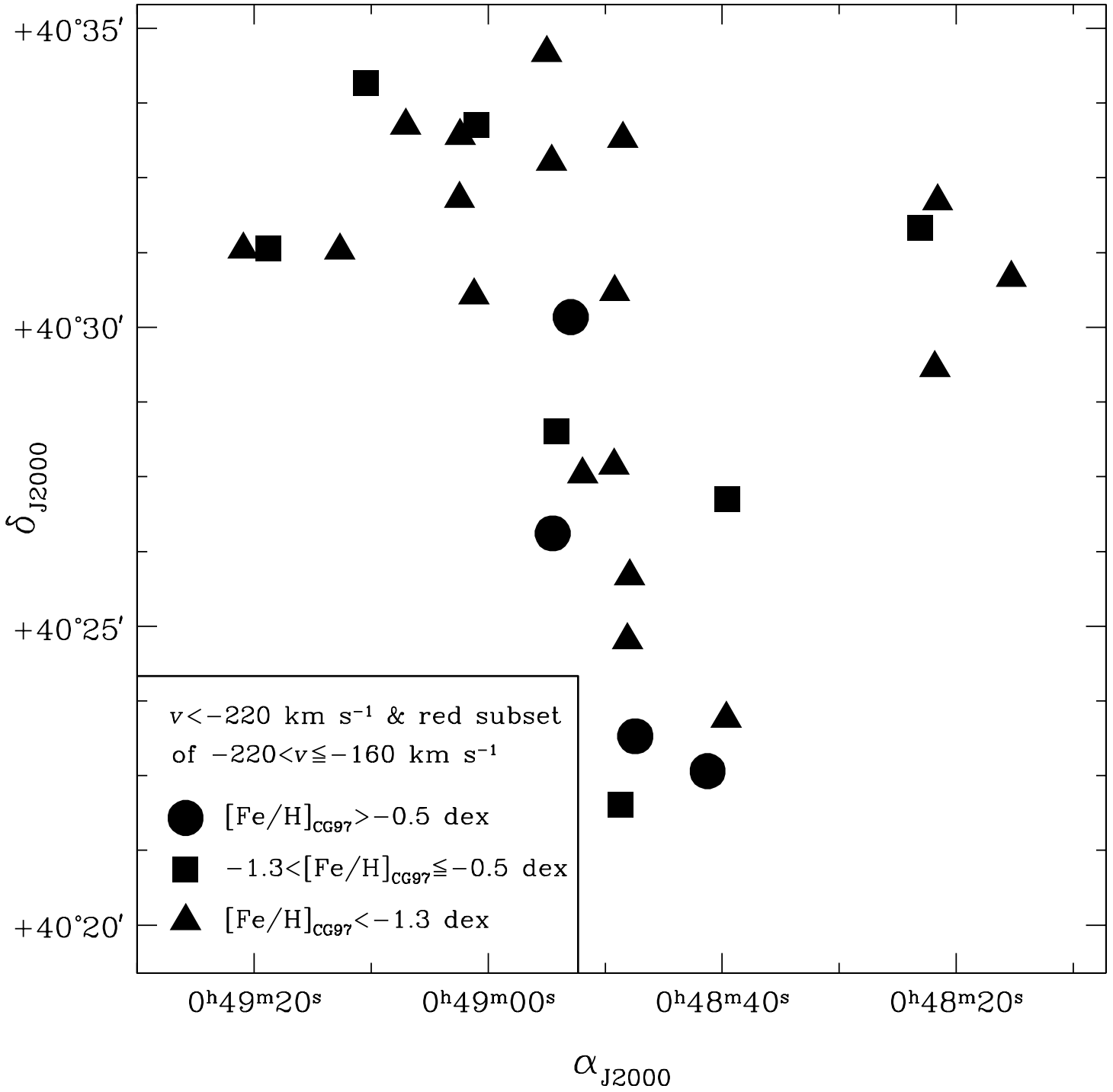


Fig. 23.— Same as Fig. 22, except only the 29 red giants comprising the secure M31 sample are shown grouped by metallicity on the Carretta-Gratton scale: $[\text{Fe}/\text{H}]_{\text{CG97}} > -0.5$ dex (circles), $-1.3 < [\text{Fe}/\text{H}]_{\text{CG97}} \leq -0.5$ dex (squares), and $[\text{Fe}/\text{H}]_{\text{CG97}} < -1.3$ dex (triangles). The first group (most metal-rich giants) consists of the the four stars that possibly belong to M31’s disk or represent debris from a past accretion event (see § 5.3).

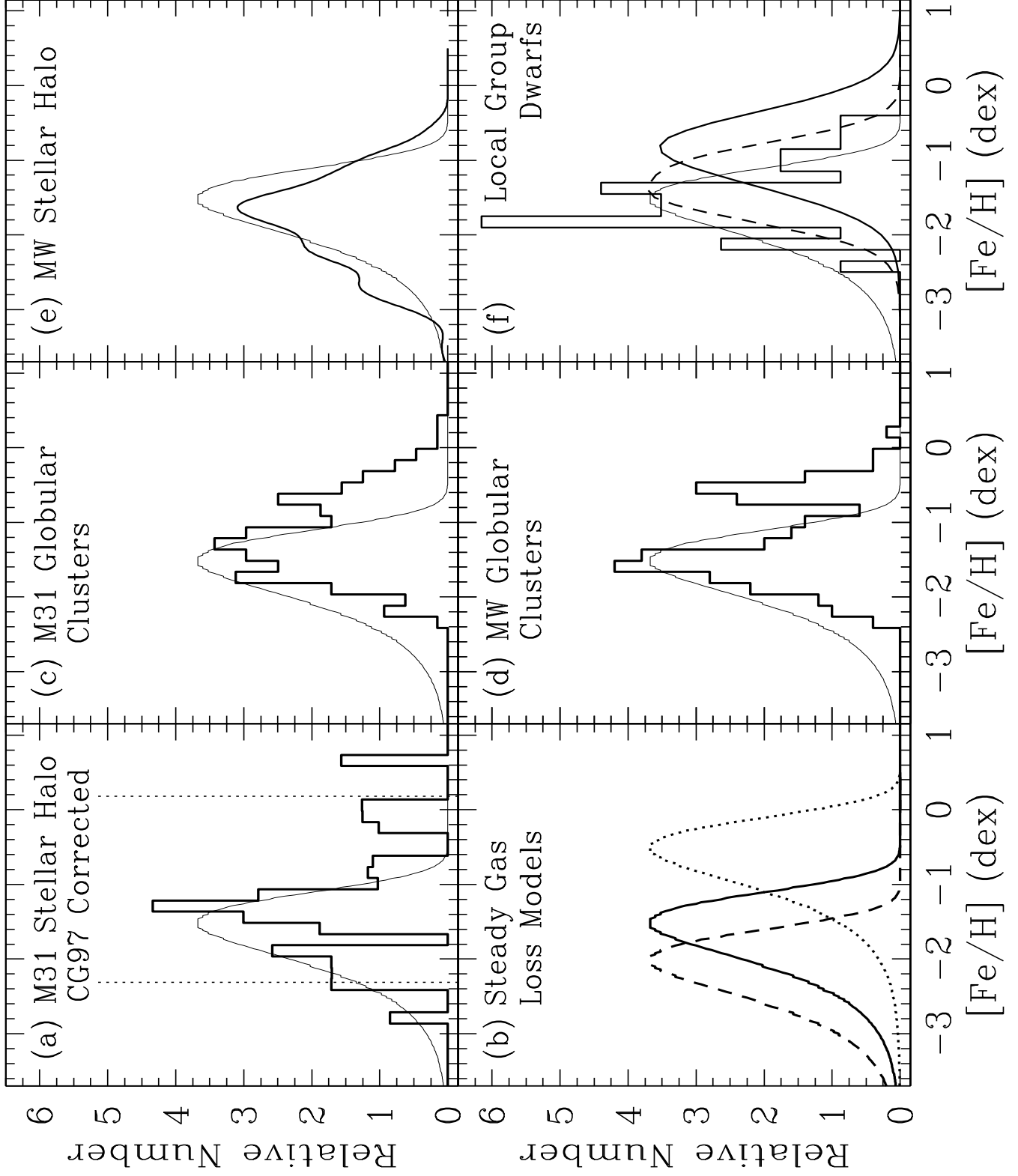


Fig. 24.— Comparison of the metallicity distribution of M31’s halo to models and other M31 and Milky Way halo samples (see § 5.5 for details including data sources for other halo tracers). (a) Secure sample of M31 halo red giant stars on the Carretta-Gratton scale, corrected for metallicity-selection effects caused by the drop in I_{TRGB} and faint-end incompleteness [bold histogram; same as Fig. 17(e)]. The dotted vertical lines mark the range over which the CG97 relation is calibrated. The small subset of giants with solar or higher metallicity may be members of M31’s disk rather than its halo (§ 5.3). (b) Chemical enrichment models with steady gas loss for $[\text{Fe}/\text{H}]_0 = -1.0$ dex and $\langle[\text{Fe}/\text{H}]\rangle = -2.0$ (dashed line), -1.5 (solid line), and -0.5 dex (dotted line). (c) The M31 globular cluster system (bold histogram). (d) The Milky Way globular cluster system (bold histogram). (e) Field stars in the Milky Way halo (bold solid line). (f) Ensemble of dwarf satellite galaxies in the Local Group: luminosity-weighted sum (bold solid line), direct sum giving equal weight to each galaxy (bold histogram), and luminosity-weighted sum of all except the two luminous metal-rich satellites, the Large Magellanic Cloud and M32 (bold dashed line). All curves are normalized to the actual number of stars in the secure M31 sample, 29. The $\langle[\text{Fe}/\text{H}]\rangle = -1.5$ dex steady-gas-loss model [bold solid line in panel (b)] is shown as a thin solid line in each of the other panels to facilitate comparison among the data sets.

Table 1. Astrometry and photometry¹ for M31 spectroscopic targets and control sample

ID ²	α_{J2000} (h : m : s)	δ_{J2000} ($^{\circ}$: $'$: $''$)	U ³ (mag)	B (mag)	V_{synth} ⁴ (mag)	R (mag)	I (mag)	$B - I$ (mag)
t1.01	00:48:57.59	+40:21:47.0	22.96	22.85	22.18	21.95	21.33	1.52
t1.02 ⁵	00:48:48.68	+40:22:00.3	24.81	24.10	22.84	22.15	21.51	2.59
t1.03	00:48:49.83	+40:22:27.3	25.46	24.38	22.85	22.22	21.21	3.16
t1.04 ⁵	00:48:41.25	+40:22:34.4	26.27	24.25	22.75	21.95	21.13	3.13
t1.05	00:48:48.22	+40:22:47.9	26.48	24.19	22.60	21.73	20.80	3.40
t1.06 ⁵	00:48:47.43	+40:23:09.5	26.12	24.97	23.50	22.85	21.93	3.05
t1.08 ⁵	00:48:39.66	+40:23:27.1	26.49	24.36	22.88	22.11	21.32	3.03
t1.10	00:48:48.49	+40:24:04.2	24.50	23.61	22.37	21.67	21.05	2.56
t1.12 ⁵	00:48:48.09	+40:24:46.0	25.88	24.40	22.93	22.07	21.38	3.01
c1.13	00:48:49.48	+40:24:58.0	24.83	22.88	21.31	20.44	19.56	3.32
t1.14	00:48:40.15	+40:25:28.2	25.63	24.18	22.58	21.61	20.78	3.40
t1.15 ⁵	00:48:47.91	+40:25:50.1	24.88	23.38	22.03	21.21	20.61	2.77
t1.17 ⁵	00:48:54.49	+40:26:33.1	25.77	25.49	23.84	22.81	21.84	3.65
t1.18	00:48:42.11	+40:26:38.4	22.09	22.21	21.65	21.22	20.90	1.31
t1.20 ⁵	00:48:39.55	+40:27:07.4	24.91	23.96	22.67	21.98	21.31	2.64
t1.21 ⁵	00:48:51.93	+40:27:32.3	25.79	24.63	23.18	22.51	21.64	2.99
t1.22 ⁵	00:48:49.24	+40:27:41.3	26.78	25.01	23.45	22.69	21.74	3.27
c1.23	00:48:50.49	+40:27:56.9	20.27	20.30	19.75	19.36	19.02	1.28
t1.24 ⁵	00:48:54.18	+40:28:15.7	25.50	24.23	22.61	21.76	20.71	3.53
c1.25	00:48:42.73	+40:28:21.6	21.99	21.57	20.71	20.17	19.70	1.86
t1.27	00:48:42.73	+40:28:46.0	24.24	23.59	22.53	22.10	21.35	2.24
t2.01 ⁵	00:48:52.94	+40:30:10.2	26.21	24.88	23.31	22.52	21.55	3.33
t2.02	00:48:54.03	+40:29:54.5	25.15	24.04	22.42	21.45	20.53	3.51
t2.03	00:48:54.66	+40:31:25.5	25.59	23.80	22.40	21.68	20.93	2.87
t2.04	00:48:56.44	+40:28:54.3	23.57	23.55	22.79	22.37	21.86	1.69
t2.05	00:48:57.27	+40:30:24.9	22.52	22.44	21.77	21.31	20.92	1.52
t2.06	00:48:58.35	+40:29:53.4	22.99	22.60	21.72	21.18	20.69	1.91
t2.08	00:49:01.29	+40:32:24.5	25.21	24.32	23.00	22.45	21.61	2.71
t2.09 ⁵	00:49:02.45	+40:32:08.9	24.77	23.91	22.65	22.10	21.31	2.59
t2.11	00:49:10.51	+40:30:41.7	25.87	24.88	23.22	22.21	21.20	3.68
t2.12 ⁵	00:49:12.68	+40:31:17.0	24.64	23.92	22.74	22.05	21.47	2.45
t2.16	00:49:17.19	+40:29:27.3	25.97	24.63	22.97	22.02	20.93	3.70

Table 1—Continued

ID ²	α_{J2000} (h : m : s)	δ_{J2000} (° : ′ : ″)	U^3 (mag)	B (mag)	V_{synth}^4 (mag)	R (mag)	I (mag)	$B - I$ (mag)
t2.17 ⁵	00:49:18.79	+40:31:18.9	25.74	24.44	22.81	21.95	20.91	3.53
t2.18 ⁵	00:49:20.93	+40:31:18.1	25.57	24.40	23.02	22.38	21.57	2.83
t2.21	00:49:25.72	+40:30:28.1	24.54	24.10	22.97	22.52	21.74	2.35
t2.22	00:49:26.84	+40:30:38.2	24.81	23.52	22.40	21.76	21.18	2.34
c3.01	00:48:39.79	+40:32:16.9	22.64	21.73	20.38	19.60	18.95	2.78
t3.02	00:48:40.80	+40:31:51.0	24.65	23.37	22.17	21.47	20.89	2.48
t3.03	00:48:41.91	+40:31:52.1	25.21	23.78	22.25	21.50	20.58	3.21
t3.04	00:48:42.97	+40:31:35.2	25.06	24.08	22.41	21.46	20.31	3.77
t3.05	00:48:43.95	+40:33:16.3	25.01	23.93	22.54	21.73	21.07	2.86
t3.06	00:48:45.13	+40:31:17.7	24.54	23.96	22.98	22.57	21.87	2.09
t3.07	00:48:46.96	+40:33:32.5	23.83	22.96	21.68	20.98	20.33	2.62
t3.08 ⁵	00:48:48.50	+40:33:09.5	26.22	24.50	23.02	22.30	21.44	3.06
c3.09	00:48:49.76	+40:31:42.0	24.58	22.91	21.24	20.27	19.12	3.80
c3.10	00:48:51.66	+40:34:07.0	21.22	20.34	19.33	18.68	18.21	2.13
t3.11	00:48:53.51	+40:34:54.2	22.86	23.26	22.36	21.84	21.31	1.95
t3.12 ⁵	00:48:55.00	+40:34:35.3	23.76	23.32	22.27	21.79	21.11	2.22
t3.13	00:48:56.77	+40:32:42.4	26.65	24.62	22.92	21.96	20.73	3.89
t3.14	00:48:58.71	+40:34:24.2	24.63	23.36	22.03	21.45	20.63	2.73
t3.15	00:48:59.54	+40:35:00.4	25.67	25.66	23.92	22.99	21.60	4.06
t3.16 ⁵	00:49:01.00	+40:33:22.9	25.42	24.27	22.93	22.41	21.51	2.76
t3.17 ⁵	00:49:02.39	+40:33:12.2	25.29	24.13	22.98	22.35	21.73	2.40
t3.18	00:49:03.46	+40:34:04.5	23.91	23.91	22.90	22.25	21.78	2.13
t3.19	00:49:04.54	+40:34:55.8	26.95	25.18	23.43	22.52	21.11	4.06
t3.20	00:49:05.70	+40:34:59.7	24.90	23.54	22.03	21.26	20.40	3.14
t3.21 ⁵	00:49:07.05	+40:33:22.3	24.60	24.21	23.07	22.29	21.82	2.39
t3.22	00:49:08.53	+40:32:40.0	24.97	24.14	22.61	21.84	20.96	3.18
t3.23	00:49:09.39	+40:33:52.9	24.87	23.58	22.02	21.21	20.30	3.28
t3.24 ⁵	00:49:10.46	+40:34:05.2	26.01	24.64	23.04	22.17	21.20	3.44
t3.25	00:49:11.79	+40:34:39.9	25.63	23.98	22.60	21.88	21.15	2.83
t3.26	00:49:13.61	+40:33:25.3	24.15	23.19	21.80	20.96	20.34	2.85
t3.27	00:49:15.01	+40:33:54.9	26.15	26.12	24.20	23.44	21.88	4.24
t3.28	00:49:16.53	+40:34:28.4	24.84	24.66	23.32	22.70	21.91	2.75

Table 1—Continued

ID ²	α_{J2000} (h : m : s)	δ_{J2000} (° : ′ : ″)	U^3 (mag)	B (mag)	V_{synth}^4 (mag)	R (mag)	I (mag)	$B - I$ (mag)
t4.01	00:48:16.93	+40:34:59.1	24.88	23.90	22.51	21.86	21.05	2.86
t4.02	00:48:35.56	+40:34:23.8	25.01	23.98	22.34	21.37	20.38	3.60
c4.03	00:48:33.59	+40:34:09.2	23.67	22.55	21.29	20.70	19.96	2.59
c4.04	00:48:27.65	+40:34:00.9	24.13	22.81	21.10	20.09	18.86	3.96
t4.05	00:48:33.61	+40:33:33.4	25.58	24.78	23.15	22.27	21.25	3.53
t4.06	00:48:26.54	+40:33:21.8	25.75	24.39	22.96	22.29	21.47	2.92
t4.07	00:48:18.49	+40:33:18.6	23.55	23.69	22.88	22.58	21.91	1.78
t4.08	00:48:25.85	+40:32:54.5	25.44	24.85	23.30	22.55	21.60	3.26
t4.09	00:48:21.48	+40:32:31.7	26.82	25.19	23.44	22.51	21.10	4.09
t4.10 ⁵	00:48:21.58	+40:32:06.7	24.56	23.06	21.69	20.90	20.25	2.81
t4.11	00:48:17.94	+40:31:57.7	24.17	23.39	21.80	20.98	20.01	3.38
t4.12 ⁵	00:48:23.08	+40:31:39.5	25.44	24.37	22.83	22.16	21.14	3.23
t4.13	00:48:14.53	+40:31:28.3	24.34	23.59	22.24	21.74	20.83	2.76
t4.14	00:48:25.54	+40:30:53.1	24.76	24.25	23.05	22.49	21.78	2.47
t4.15 ⁵	00:48:15.29	+40:30:49.7	24.39	23.34	21.90	21.16	20.38	2.96
t4.16	00:48:33.56	+40:30:16.6	23.84	23.16	22.05	21.37	20.83	2.33
t4.17	00:48:20.40	+40:30:09.9	25.87	25.39	23.72	22.89	21.64	3.75
t4.18	00:48:25.52	+40:29:49.5	23.37	22.75	21.93	21.41	20.94	1.81
t4.19	00:48:31.56	+40:29:27.5	25.28	23.82	22.39	21.58	20.89	2.92
t4.20 ⁵	00:48:21.82	+40:29:19.2	25.30	23.99	22.82	22.20	21.57	2.42
t4.21	00:48:15.06	+40:29:03.3	23.77	22.99	21.87	21.20	20.65	2.34
t4.22	00:48:20.10	+40:28:34.8	24.35	23.69	22.34	21.57	20.93	2.76
t4.23	00:48:16.27	+40:28:24.6	23.06	22.98	21.89	21.41	20.70	2.28
c4.24	00:48:21.92	+40:28:07.7	23.36	22.22	20.55	19.69	18.45	3.77
t4.25	00:48:20.24	+40:27:57.6	23.82	23.09	21.96	21.35	20.73	2.36
t5.02	00:48:43.20	+40:30:18.4	25.74	24.78	22.87	21.90	20.53	4.25
t5.03 ⁵	00:48:54.58	+40:32:46.2	24.12	23.84	22.59	22.07	21.27	2.58
c5.04	00:48:47.31	+40:30:23.3	23.34	22.19	20.80	20.03	19.34	2.84
t5.05 ⁵	00:48:49.19	+40:30:35.6	24.96	23.44	22.04	21.23	20.57	2.87
t5.06	00:48:51.92	+40:30:51.2	22.96	22.82	22.16	21.79	21.32	1.50
c5.07	00:48:54.40	+40:30:59.8	25.90	23.76	22.02	20.97	19.70	4.06
t5.08	00:48:51.24	+40:29:44.3	24.97	24.01	22.32	21.40	20.13	3.88

Table 1—Continued

ID ²	α_{J2000} (h : m : s)	δ_{J2000} (° : ′ : ″)	U^3 (mag)	B (mag)	V_{synth}^4 (mag)	R (mag)	I (mag)	$B - I$ (mag)
t5.09	00:49:00.70	+40:31:49.4	22.66	22.50	21.84	21.36	21.00	1.50
t5.10	00:48:53.64	+40:29:15.2	25.19	23.87	22.23	21.34	20.27	3.60
t5.11 ⁵	00:49:01.22	+40:30:32.1	23.99	23.55	22.31	21.66	20.99	2.55
t5.12	00:48:58.05	+40:29:21.1	24.92	23.91	22.31	21.41	20.48	3.43
t5.13	00:49:04.27	+40:30:10.1	23.26	23.15	22.11	21.72	20.94	2.21
t5.14	00:49:10.25	+40:30:48.0	25.36	24.61	22.63	21.56	20.03	4.58
t5.15	00:49:06.15	+40:29:05.7	21.77	21.81	21.35	21.01	20.71	1.10
t5.16	00:49:11.63	+40:30:12.7	26.39	25.83	24.13	23.21	21.91	3.92
t5.17	00:49:05.31	+40:27:57.4	26.34	25.71	23.76	22.48	21.16	4.55
t5.18	00:49:05.76	+40:27:42.8	23.78	23.48	22.67	22.35	21.70	1.77
t5.19	00:49:09.34	+40:27:53.3	22.05	21.89	21.08	20.62	20.11	1.78
c5.20	00:49:09.65	+40:27:27.9	23.04	22.01	20.47	19.60	18.80	3.21
c5.21	00:49:11.79	+40:27:43.4	22.64	21.52	19.96	19.15	18.25	3.28
t5.22	00:49:15.70	+40:28:25.4	24.96	23.67	22.04	21.21	20.10	3.57
t5.23	00:49:17.30	+40:28:13.2	24.87	23.90	22.31	21.33	20.54	3.36
t5.24	00:49:11.36	+40:26:16.3	23.49	23.94	22.94	22.59	21.81	2.13

¹ $UBRI$ photometry from RGG study.

²Object ID key: single letter prefix (‘t’/‘c’ for main sample of M31 targets/control sample), mask number (1–5), period, and slit number.

³26 objects in the main M31 spectroscopic target sample and 1 control sample object have $U > U_{\text{lim}}$, where $U_{\text{lim}} = 25.60$ is the 3σ limiting magnitude, and were treated as U upper limits in the $UBRI$ -based selection process in the RGG study. Of the 29 objects comprising the secure M31 sample, 11 have $U > U_{\text{lim}}$ and 2 of the 11 are red intermediate-velocity stars.

⁴Synthesized from apparent B magnitude and $B - I$ color of each object, using the relation between $V - I$ and $B - I$ colors for model stellar isochrones (Bergbusch & Vandenberg 2001).

⁵Member of secure sample of M31 red giants: 25 stars with $v < -220 \text{ km s}^{-1}$ and 4 red ($B - I > 2$) stars with $-220 < v < -160 \text{ km s}^{-1}$ (§ 3.2).

Table 2. Details of observations

Multislit mask #:	1	2	3	4	5
Number of target stars	18	15	25	22	19
Number of control stars	3	0	3	3	4
Date of observation (UT)	10/3/96	10/4/96	10/22/97	10/23/97	10/23/97
Total exposure time (hr)	3.8	3.7	4.5	4.5	1.5
Number of exposures	6	6	5	5	2
Indiv. exposure times (s)	3000	2099	3600	3600	2700
	3000	3000	3600	3600	2700
	3000	3000	3600	3600	—
	3000	711	2700	2700	—
	821	1900	2700	2700	—
	978	2652	—	—	—

Table 3. Spectroscopic results for M31 targets and control sample

ID ¹	v_{hel} (km s ⁻¹)	r_{TD}^2	A_{CCF}^3 (arb. units)	$\sum \text{Ca}_{\text{CCF}}^4$ (Å)	W'^5 (Å)	$[\text{Fe}/\text{H}]_{\text{ZW}}^6$ (dex)	$[\text{Fe}/\text{H}]_{\text{CG97}}^7$ (dex)	$[\text{Fe}/\text{H}]_{\text{phot}}^8$ (dex)
t1.01	-138	5.57	53.09	4.86	2.94	-1.72	-1.42	(-4.76)
t1.02 ⁹	-288	3.60	56.27	5.15	3.66	-1.40	-1.12	-1.53
t1.03	-73	5.81	40.14	3.67	2.19	-1.94	-1.74	-0.98
t1.04 ⁹	-354	8.88	80.61	7.37	5.82	(+1.33)	-0.21	-1.09
t1.05	-44	5.93	35.22	3.22	1.58	-2.11	-2.00	-1.08
t1.06 ⁹	-340	5.49	78.28	7.16	6.09	(+1.95)	-0.10	-0.63
t1.08 ⁹	-168	3.93	44.98	4.11	2.65	-1.81	-1.55	-1.05
t1.10	-39	3.43	38.92	3.56	1.77	-2.05	-1.92	-2.00
t1.12 ⁹	-314	7.47	45.95	4.20	2.77	-1.78	-1.50	-1.03
c1.13	-109	9.66	33.54	3.07	—	—	—	—
t1.14	-48	4.47	33.60	3.07	1.42	-2.16	-2.06	-1.09
t1.15 ⁹	-522	16.84	42.85	3.92	1.91	-2.01	-1.86	-2.04
t1.17 ⁹	-330	7.19	96.04	8.78	7.93	(+8.70)	(+0.67)	-0.24
t1.18	-186	7.31	39.33	3.60	1.34	-2.19	-2.10	(-6.13)
t1.20 ⁹	-240	4.96	58.70	5.37	3.77	-1.33	-1.08	-1.62
t1.21 ⁹	-327	6.90	45.32	4.15	2.87	-1.74	-1.45	-0.87
t1.22 ⁹	-493	6.68	46.28	4.23	3.13	-1.65	-1.34	-0.54
c1.23	-55	13.61	30.12	2.75	—	—	—	—
t1.24 ⁹	-166	12.16	60.55	5.54	3.90	-1.24	-1.02	-1.04
c1.25	-104	8.94	48.69	4.45	—	—	—	—
t1.27	—	—	—	—	—	—	—	-2.43
t2.01 ⁹	-328	4.76	84.96	7.77	6.58	(+3.29)	(+0.10)	-0.61
t2.02	-64	9.81	43.01	3.93	2.17	-1.94	-1.75	-1.20
t2.03	-49	4.65	56.37	5.16	3.38	-1.54	-1.24	-1.58
t2.04	—	2.08	—	—	—	—	—	(-3.65)
t2.05	—	1.37	—	—	—	—	—	(-5.21)
t2.06	-165	9.44	52.34	4.79	2.58	-1.83	-1.58	(-4.05)
t2.08	-84	2.74	42.51	3.89	2.50	-1.86	-1.61	-1.26
t2.09 ⁹	-511	4.51	43.93	4.02	2.40	-1.88	-1.65	-1.70
t2.11	-41	6.45	50.04	4.58	3.33	-1.57	-1.26	-0.59
t2.12 ⁹	-242	2.35	31.40	2.87	1.32	-2.20	-2.11	-1.84
t2.16	-72	5.15	26.77	2.45	1.04	-2.31	-2.22	-0.76

Table 3—Continued

ID ¹	v_{hel} (km s ⁻¹)	r_{TD}^2	A_{CCF}^3 (arb. units)	$\sum C_{\text{aCCF}}^4$ (Å)	W'^5 (Å)	[Fe/H] _{ZW} ⁶ (dex)	[Fe/H] _{CG97} ⁷ (dex)	[Fe/H] _{phot} ⁸ (dex)
t2.17 ⁹	-213	2.73	69.60	6.37	4.86	-0.32	-0.62	-0.90
t2.18 ⁹	-249	4.53	49.48	4.53	3.15	-1.64	-1.34	-1.12
t2.21	—	1.65	—	—	—	—	—	-1.81
t2.22	-63	2.74	24.85	2.27	0.50	-2.61	-2.45	-2.34
c3.01	-61	10.39	47.61	4.35	—	—	—	—
t3.02	-16	3.98	45.64	4.17	2.25	-1.92	-1.71	-2.33
t3.03	-61	8.10	46.11	4.22	2.35	-1.90	-1.67	-1.45
t3.04	-36	6.14	31.19	2.85	1.08	-2.29	-2.20	-1.21
t3.05	-81	4.14	64.61	5.91	4.22	-0.99	-0.89	-1.48
t3.06	—	1.83	—	—	—	—	—	-2.36
t3.07	-56	4.89	42.60	3.90	1.66	-2.08	-1.96	-2.59
t3.08 ⁹	-301	5.80	49.76	4.55	3.17	-1.63	-1.33	-0.93
c3.09	-36	17.17	33.46	3.06	—	—	—	—
c3.10	-111	17.82	41.20	3.77	—	—	—	—
t3.11	+79	3.08	12.56	1.15	-0.65	(-3.76)	(-2.93)	(-3.27)
t3.12 ⁹	-306	10.99	41.25	3.77	1.92	-2.01	-1.85	-2.72
t3.13	-36	5.79	33.50	3.06	1.63	-2.09	-1.98	-0.81
t3.14	-81	12.35	45.14	4.13	2.12	-1.96	-1.77	-2.10
t3.15	+89	3.12	28.76	2.63	1.83	-2.04	-1.89	-0.19
t3.16 ⁹	-226	14.51	52.32	4.79	3.35	-1.56	-1.25	-1.27
t3.17 ⁹	-196	2.68	45.50	4.16	2.76	-1.78	-1.50	-1.72
t3.18	—	3.21	—	—	—	—	—	-2.33
t3.19	-101	4.67	31.31	2.86	1.75	-2.06	-1.93	-0.48
t3.20	-36	7.76	32.52	2.97	0.96	-2.35	-2.26	-1.68
t3.21 ⁹	-301	1.94	30.66	2.80	1.46	-2.15	-2.05	-1.69
t3.22	-71	3.72	45.58	4.17	2.53	-1.85	-1.60	-1.16
t3.23	-56	9.88	41.73	3.82	1.80	-2.04	-1.90	-1.61
t3.24 ⁹	-256	5.73	61.70	5.64	4.28	-0.95	-0.86	-0.75
t3.25	-121	9.58	48.01	4.39	2.75	-1.78	-1.51	-1.46
t3.26	-71	9.03	45.15	4.13	1.97	-2.00	-1.83	-2.17
t3.27	-11	3.10	19.15	1.75	1.13	-2.27	-2.18	+0.11
t3.28	-141	2.78	104.16	9.53	8.34	(+10.90)	(+0.84)	-0.99

Table 3—Continued

ID ¹	v_{hel} (km s ⁻¹)	r_{TD}^2	A_{CCF}^3 (arb. units)	$\sum C_{\text{aCCF}}^4$ (Å)	W'^5 (Å)	$[\text{Fe}/\text{H}]_{\text{ZW}}^6$ (dex)	$[\text{Fe}/\text{H}]_{\text{CG97}}^7$ (dex)	$[\text{Fe}/\text{H}]_{\text{phot}}^8$ (dex)
t4.01	-61	6.74	24.21	2.21	0.51	-2.60	-2.44	-1.51
t4.02	—	1.76	—	—	—	—	—	-1.26
c4.03	-111	5.64	32.69	2.99	—	—	—	—
c4.04	-61	14.76	24.52	2.24	—	—	—	—
t4.05	-1	4.93	36.07	3.30	2.01	-1.99	-1.82	-0.66
t4.06	-131	3.76	59.91	5.48	4.07	-1.12	-0.95	-1.08
t4.07	—	2.21	—	—	—	—	—	(-3.28)
t4.08	—	1.95	—	—	—	—	—	-0.64
t4.09	-86	4.51	30.09	2.75	1.64	-2.09	-1.97	-0.48
t4.10 ⁹	-581	6.58	31.88	2.92	0.69	-2.49	-2.37	-2.31
t4.11	-86	11.72	41.88	3.83	1.67	-2.08	-1.96	-1.77
t4.12 ⁹	-221	6.00	54.73	5.01	3.51	-1.48	-1.19	-0.97
t4.13	—	3.38	—	—	—	—	—	-1.85
t4.14	—	2.19	—	—	—	—	—	-1.55
t4.15 ⁹	-241	7.28	33.46	3.06	0.97	-2.34	-2.25	-1.95
t4.16	-101	4.78	67.59	6.18	4.18	-1.03	-0.90	-2.72
t4.17	—	2.60	—	—	—	—	—	-0.30
t4.18	-176	5.82	25.66	2.35	0.27	-2.77	-2.55	(-4.08)
t4.19	-46	6.67	53.33	4.88	3.10	-1.66	-1.36	-1.55
t4.20 ⁹	-286	2.96	25.58	2.34	0.84	-2.41	-2.31	-1.82
t4.21	-76	5.97	47.23	4.32	2.21	-1.93	-1.73	(-2.88)
t4.22	—	0.62	—	—	—	—	—	-1.76
t4.23	—	1.44	—	—	—	—	—	(-2.98)
c4.24	-101	11.95	27.65	2.53	—	—	—	—
t4.25	-111	6.73	47.15	4.31	2.26	-1.92	-1.71	-2.76
t5.02	—	2.13	—	—	—	—	—	-0.83
t5.03 ⁹	-341	3.98	13.02	1.19	-0.46	(-3.51)	(-2.85)	-1.79
c5.04	-61	3.11	38.65	3.54	—	—	—	—
t5.05 ⁹	-461	2.43	43.37	3.97	1.97	-2.00	-1.83	-1.91
t5.06	-216	2.87	13.62	1.25	-0.68	(-3.80)	(-2.94)	(-4.86)
c5.07	-66	4.79	39.32	3.60	—	—	—	—
t5.08	+19	4.99	16.24	1.49	-0.34	(-3.36)	(-2.80)	-1.33

Table 3—Continued

ID ¹	v_{hel} (km s ⁻¹)	r_{TD}^2	A_{CCF}^3 (arb. units)	$\sum \text{Ca}_{\text{CCF}}^4$ (Å)	W'^5 (Å)	$[\text{Fe}/\text{H}]_{\text{ZW}}^6$ (dex)	$[\text{Fe}/\text{H}]_{\text{CG97}}^7$ (dex)	$[\text{Fe}/\text{H}]_{\text{phot}}^8$ (dex)
t5.09	-106	3.60	46.54	4.26	2.12	-1.96	-1.77	(-5.18)
t5.10	-101	5.14	45.98	4.21	2.32	-1.90	-1.68	-1.35
t5.11 ⁹	-306	3.50	33.43	3.06	1.23	-2.23	-2.15	-2.08
t5.12	-106	4.49	27.34	2.50	0.67	-2.50	-2.38	-1.31
t5.13	+239	2.89	176.45	16.14	14.18	(+83.87)	(+3.30)	(-2.90)
t5.14	-6	4.19	16.97	1.55	-0.07	(-3.07)	-2.69	-1.38
t5.15	-111	2.49	17.51	1.60	-0.85	(-4.05)	(-3.02)	(-7.43)
t5.16	—	2.14	—	—	—	—	—	-0.05
t5.17	—	3.30	—	—	—	—	—	-0.32
t5.18	-211	4.33	67.74	6.20	4.60	-0.63	-0.73	(-3.47)
t5.19	—	1.42	—	—	—	—	—	(-5.40)
c5.20	-6	11.07	30.29	2.77	—	—	—	—
c5.21	-36	14.28	32.50	2.97	—	—	—	—
t5.22	-6	8.19	33.95	3.11	1.10	-2.28	-2.20	-1.52
t5.23	-16	2.28	68.42	6.26	4.43	-0.81	-0.80	-1.32
t5.24	—	2.02	—	—	—	—	—	-2.28

¹See object ID key in Table 1.

²Significance of cross correlation peak (Tonry & Davis 1979). Radial velocity measurement fails for 19 objects with small r_{TD} values, and they are excluded from further spectroscopic analysis.

³Area under cross correlation peak, within ± 225 km s⁻¹ of it, relative to a linear baseline fit; see § 4.2.2 for explanation of units.

⁴Effective weighted sum of Ca II equivalent widths determined from empirical scaling of A_{CCF} (§ 4.2.2).

⁵Reduced Ca II line strength index corrected to a common value of $\log g$ and T_{eff} for main M31 spectroscopic target sample only (§ 4.2.2).

⁶Spectroscopic calibration of Zinn & West (1984) metallicity scale from Rutledge et al. (1997b) for main sample only (§ 4.2.2). Values in parentheses represent extrapolations well beyond the calibrated range (by > 0.5 dex) and should be treated as highly uncertain.

⁷Same as (6) for Carretta & Gratton (1997) metallicity scale.

⁸Same as (6) for a photometric calibration based on Bergbusch & Vandenberg (2001) model isochrones and two high metallicity Padova (Girardi et al. 2000) model isochrones (§ 4.1.1).

⁹Member of secure sample of M31 red giants: 25 stars with $v < -220$ km s⁻¹ and 4 red ($B - I > 2$) stars with $-220 < v < -160$ km s⁻¹ (§ 3.2).

Table 4. Metallicity measurements

Sample:	Main	Excl. Red Intermed. Vel. Stars ¹	Excl. Poss. Disk Stars ²	Excl. Red Intermed. Vel. & Poss. Disk Stars ^{1,2}	Poss. Disk Stars ²
Number of stars	29	25	25	21	4
[Fe/H]_{ZW}³ →					
Mean	-1.04	-1.00	-1.82	-1.92	(+3.82)
Median	-1.74	-1.74	-1.78	-1.88	(+2.62)
RMS	2.33	2.50	0.60	0.53	3.35
Corrected Mean ⁶	-0.51	-0.40	-1.77	-1.87	(+4.57)
Corrected Median ⁶	-1.64	-1.65	-1.78	-1.78	(+3.29)
Corrected RMS ⁶	2.98	3.19	0.58	0.51	3.23
[Fe/H]_{CG97}⁴ →					
Mean	-1.38	-1.41	-1.62	-1.70	+0.11
Median	-1.45	-1.45	-1.50	-1.65	+0.00
RMS	0.80	0.84	0.54	0.52	0.39
Corrected Mean ⁶	-1.22	-1.22	-1.56	-1.65	+0.20
Corrected Median ⁶	-1.34	-1.34	-1.50	-1.50	+0.10
Corrected RMS ⁶	0.88	0.93	0.52	0.50	0.38
[Fe/H]_{phot}⁵ →					
Mean	-1.37	-1.40	-1.49	-1.55	-0.64
Median	-1.27	-1.58	-1.62	-1.69	-0.62
RMS	0.60	0.63	0.55	0.56	0.35
Corrected Mean ⁶	-1.25	-1.26	-1.42	-1.47	-0.56
Corrected Median ⁶	-1.05	-1.09	-1.27	-1.62	-0.61
Corrected RMS ⁶	0.64	0.67	0.57	0.59	0.30

¹“Red Intermed. Vel. Stars” refers to red subset of stars in intermediate radial velocity range, $-220 < v < -160$ km s⁻¹; these are likely to be M31 halo red giants (§ 3.2).

²“Poss. Disk Stars” refers to kinematically-coherent group of four high-metallicity stars with velocities close to M31’s systemic velocity, similar to what might be expected for M31 disk stars or for metal-rich debris from a past accretion event (§ 5.3).

³Spectroscopic calibration of Zinn & West (1984) metallicity scale from Rutledge et al. (1997b); see § 4.2.2. Values in parentheses represent extrapolations well beyond the calibrated range and should be treated as highly uncertain.

⁴Same as (3) for Carretta & Gratton (1997) metallicity scale.

⁵Same as (3) for a photometric calibration based on Bergbusch & Vandenberg (2001) model isochrones and two high metallicity Padova model isochrones (Girardi et al. 2000); see § 4.1.1.

⁶Corrected for bias caused by I_{TGRB} becoming fainter with increasing [Fe/H] and incompleteness at the faint end (§ 5.2).